

MICROSCOPIC INVESTIGATION OF
MANGANESE BISMUTH MAGNETIC MATERIALS



A Thesis Submitted in Partial Fulfillment of the Requirement for the
Degree of Doctor of Philosophy in Physics
Suranaree University of Technology
Academic Year 2021

การศึกษาระดับแม่เหล็กแมงกานีสบิสมัทเชิงจุลภาค



นางสาวจรงค์ ป่อทรัพย์

วิทยานิพนธ์นี้เป็นส่วนหนึ่งของการศึกษาตามหลักสูตรปริญญาวิทยาศาสตรดุษฎีบัณฑิต

สาขาวิชาฟิสิกส์

มหาวิทยาลัยเทคโนโลยีสุรนารี

ปีการศึกษา 2564

**MICROSCOPIC INVESTIGATION OF
MANGANESE BISMUTH MAGNETIC MATERIALS**

Suranaree University of Technology has approved this thesis submitted in partial fulfillment of the requirements for the Degree of Doctor of Philosophy.

Thesis Examining Committee

Rattikorn Yimnirun

(Prof. Dr. Rattikorn Yimnirun)

Chairperson

Prayoon Songsiritthigul

(Assoc. Prof. Dr. Prayoon Songsiritthigul)

Member (Thesis Advisor)

Panomsak Meemon

(Assoc. Prof. Dr. Panomsak Meemon)

Member

Supree Pinitsoontorn

(Prof. Dr. Supree Pinitsoontorn)

Member

Narong Chanlek

(Dr. Narong Chanlek)

Member

Chatchai Jothityang

(Assoc. Prof. Dr. Chatchai Jothityangkoon)

Vice Rector for Academic Affairs
and Quality Assurance

Santi Maensiri

(Prof. Dr. Santi Maensiri)

Dean of Institute of Science

จรงค์ บ่อทรัพย์ : การศึกษาสารแม่เหล็กแมงกานีสบิสมัทเชิงจุลภาค (MICROSCOPIC INVESTIGATION OF MANGANESE BISMUTH MAGNETIC MATERIALS). อาจารย์ที่ปรึกษา : รองศาสตราจารย์ ดร.ประยูร ส่งสิริฤทธิกุล, 115 หน้า.

คำสำคัญ: กระบวนการเผาผนึกแบบมีเฟสของเหลว/เฟสแมงกานีสบิสมัทที่อุณหภูมิต่ำ/การเผาผนึกแบบสูญญากาศ/สัมประสิทธิ์การแพร่/คุณสมบัติแม่เหล็ก/ความเสถียรทางแม่เหล็ก/การเสื่อมสภาพ

การเผาผนึกด้วยเฟสของของเหลวที่อุณหภูมิต่ำ (LPS) ในสูญญากาศได้ถูกแสดงให้เห็นว่าเป็นเทคนิคที่สามารถสังเคราะห์สารประกอบเฟอร์โรแมกเนติกของแมงกานีสบิสมัทในเฟสอุณหภูมิต่ำ (LTP-MnBi) ซึ่งเป็นวัสดุแม่เหล็กปราศจากธาตุหายากสำหรับการผลิตแม่เหล็กถาวรประสิทธิภาพสูง เทคนิคนี้ไม่ต้องมีกระบวนการหรือขั้นตอนที่ยุ่งยากหลังจากการเผาผนึก ดังนั้นจึงเป็นเทคนิคที่ง่ายสำหรับการสังเคราะห์สาร LTP-MnBi จำนวนมากได้ พบว่าผงของ LTP-MnBi มีสนามลบล้างความเป็นแม่เหล็กมีค่าสูงสุดประมาณ 5 kOe และผลผลิตพลังงานสูงสุด ($(BH)_{max}$) มีค่าสูงสุดประมาณ 5.5 MGOe ที่อุณหภูมิห้องนั้นสามารถสังเคราะห์ขึ้นโดยการเผาผนึกที่ 325 °C ในขั้นตอนเดียวของการเผาผนึกในเฟสของของเหลวที่อุณหภูมิต่ำ ความซับซ้อนของกระบวนการเผาผนึกในเฟสของของเหลวสำหรับการสังเคราะห์ LTP-MnBi ถูกอธิบายโดยกลไกการแพร่มีบทบาทสำคัญในการก่อตัวของ LTP-MnBi ระหว่างการเผาผนึก ที่ผงบิสมัท (Bi) จะถูกหลอมเป็นของเหลวที่อุณหภูมิการเผาผนึกที่สูงกว่าจุดหลอมเหลวของมัน และของเหลวดังกล่าวจะเคลื่อนผ่านพื้นผิวภายนอกของอนุภาคแมงกานีส (Mn) และตามรอยแตกภายในอนุภาค Mn ชั้น LTP-MnBi เกิดขึ้นเมื่อ Bi แพร่เข้าไปเนื้อสารของอนุภาค Mn จากพื้นผิวภายนอกของอนุภาคและจากพื้นผิวภายในของรอยแตกภายในอนุภาค ค่าสัมประสิทธิ์การแพร่ใน MnBi ได้ถูกคำนวณจากผลการทดลองที่อุณหภูมิระหว่าง 275 ถึง 375 °C ค่าสัมประสิทธิ์การแพร่จะเป็นไปตามสมการอาร์เรเนียส โดยมีค่าพารามิเตอร์หน้าของทอมเอ็กซ์โพเนนเชียล คือ $5.33 \times 10^{-10} \text{ cm}^2/\text{s}$ และพลังงานกระตุ้นคือ 0.45 eV สมการนี้ให้ข้อมูลเพื่อคำนวณความหนาของชั้น LTP-MnBi ที่ก่อตัวขึ้นบริเวณพื้นผิวภายนอกของอนุภาคและพื้นผิวภายในของรอยแตกภายในอนุภาค ที่ได้จากการเผาผนึกที่อุณหภูมิระหว่าง 275 ถึง 375 °C สำหรับระยะเวลาการเผาผนึกใด ๆ

สารแม่เหล็ก LTP-MnBi ที่ได้จากการเผาผนึกแสดงการเปลี่ยนแปลงที่ค่อนข้างน่าสนใจคือว่าประสิทธิภาพของสารแม่เหล็กมีค่าเพิ่มขึ้นตามกาลเวลา โดยพบว่าทั้งสนามลบล้างความเป็นแม่เหล็กและผลผลิตพลังงานสูงสุดที่อุณหภูมิห้องมีค่าเพิ่มขึ้นร้อยละ 52 เมื่อระยะเวลาผ่านไป 18 เดือนเมื่อเทียบกับสารที่เพิ่งสังเคราะห์ขึ้นใหม่ การเพิ่มประสิทธิภาพของแม่เหล็กคาดว่าน่าจะเกิดจากการเพิ่มขึ้นของเนื้อสารทำให้ความหนาของ LTP-MnBi มีค่าเพิ่มขึ้น ความหนาที่เพิ่มขึ้นนั้นน่าจะเกิดจาก

การที่มีการแพร่ผ่านชั้น LTP-MnBi และได้ข้อสรุปจากผลการทดลองว่า LTP-MnBi ที่สังเคราะห์ขึ้นในงานนี้ค่อนข้างเสถียรที่อุณหภูมิห้อง อย่างไรก็ตามสาร LTP-MnBi สามารถเสื่อมสภาพได้ง่ายเมื่อมีการให้ความร้อนกับสารที่อุณหภูมิ 150 °C ในอากาศ การเสื่อมสภาพส่วนใหญ่เกิดจากการปฏิกิริยาออกซิเดชันทำให้เกิดสารหลักคือ ออกไซด์ของ Mn และ Bi ดังนั้นการป้องกันการสัมผัสกับอากาศต้องพิจารณาอย่างจริงจังเมื่อต้องการใช้สาร LTP-MnBi ที่อุณหภูมิสูง การเคลือบฟิล์มบนผิวของสารแม่เหล็กอาจเป็นวิธีแก้ปัญหานี้ได้



สาขาวิชาฟิสิกส์
ปีการศึกษา 2564

ลายมือชื่อนักศึกษา ชวิภ
ลายมือชื่ออาจารย์ที่ปรึกษา ชบ.ภ. อ.

JONGRAK BORSUP : MICROSCOPIC INVESTIGATION OF MANGANESE BISMUTH
MAGNETIC MATERIALS. THESIS ADVISOR : ASSOC. PROF. PRAYOON
SONGSIRIRITHIGUL, Ph.D. 115 PP.

Keyword: LIQUID-PHASE SINTERING/LTP-MnBi /VACUUM SINTERING/DIFFUSION
COEFFICIENT /MAGNETIC PROPERTIES/ MAGNETIC STABILITY/DEGRADATION

Low-temperature liquid-phase sintering (LPS) in vacuum has been demonstrated to be a promising method for synthesizing ferromagnetic low-temperature phase manganese bismuth compound (LTP-MnBi), which is also a promising rare-earth-free magnetic materials for fabricating high-performance permanent magnets. The technique requires no extensive post-sintering processing, and thus is a facile technique for mass production. Powder of LTP-MnBi with coercivity of about 5 kOe at room temperature has been achieved by a single-step low-temperature LPS. The highest $(BH)_{max}$ of approximately 5.5 MGOe was obtained for the MnBi powder sintered at 325 °C. The complex nature of the liquid phase sintering processes for synthesizing LTP-MnBi was explained. The diffusion mechanism plays an important role in the formation of LTP-MnBi during LPS. At sintering temperatures higher than the melting point, Bi powder was melted into liquid before migrating over the surface of the Mn particles, and along the cracks within the Mn particles. LTP-MnBi layers were formed when Bi diffuses into the bulk Mn particles from their exterior surfaces and from interior surfaces of cracks within the particles. The diffusion coefficient in MnBi was experimentally determined. At temperatures between 275 and 375 °C, the diffusion coefficient follows the Arrhenius equation with the pre-exponential factor of 5.33×10^{-10} cm²/s and activation energy of 0.45 eV. This equation provides the information to estimate the thickness of LTP-MnBi layers sintered at any temperature between 275 and 375 °C for a given sintering duration.

The sintered LTP-MnBi exhibits rather interesting changes that the magnetic performance improved with aging. Both coercivity and energy product were found to increase by 52% with 18-month aging at room temperature. The enhance in the

ACKNOWLEDGEMENTS

Words cannot express my gratitude to my advisor, Assoc. Prof. Dr. Prayoon Songsiriritthigul. He has provided me with great guidance, never-ending encouragement and supports. He has given me opportunities to access to different research facilities both in Thailand and abroad. He was kind and listened to my opinions even at conflicting times. Thousand thanks for accepting me as an advisee when I applied to study at SUT, and that has provided me with many educational opportunities. My thesis was not completed without invaluable advice and feedback from the Thesis Examining committee such as Prof. Dr. Rattikorn Yimnirun (Chairperson), Assoc. Prof. Dr. Panomsak Meemon, Prof. Dr. Supree Pinitsuntorn and Dr. Narong Chanlek.

In particular, Prof. Dr. Supree Pinitsuntorn for the access and advice on the VSM technique for the investigation of MnBi magnetic properties at the Faculty of Science, Khon Kaen University, Thailand.

I would also like to express my deepest gratitude to Dr. Chanchana Thanachayanont at MTEC (Thailand) for the advice and access to FE-SEM. Mr. Visittapong Yordsri is also acknowledged for his excellent skills and assistant in the FE-SEM observations.

I would like to thank Dr. Tanachat Eknapakul for assisting in analyzing the experimental results and helping in writing. I would also like to thank Asst. Prof. Dr. Michael F. Smith for his advice and help in writing manuscripts. I am very proud to have opportunities to attend his classes since I started at SUT.

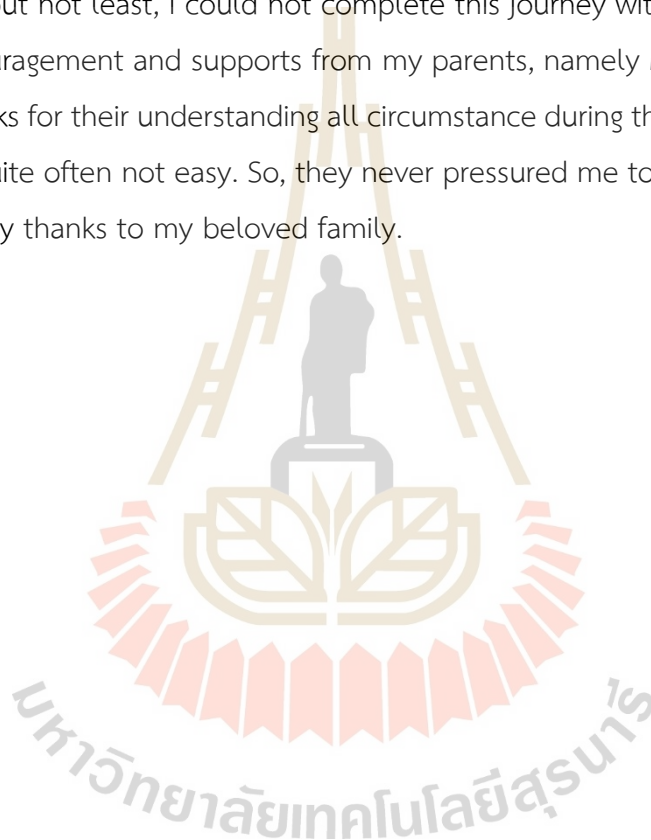
Moreover, I am also thankful to Mr. Anuchit Ruangvittayanon at the microscopy laboratory of SLRI for valuable advice and assistant in the preparation of the cross-sectional MnBi powder particles. I would like to thank Dr. Pinit Kitkhuntod and Dr. Ittipon Fongkeaw for advice and helps on measurements, data analysis and theoretical calculations of X-ray absorption spectra.

Special thanks to all former and present members of the Nano-spectroscopy group. Especially, Dr. Thanit Saisopa (RMUTI), Mr. Satienrapong Ngamsomrit, Ms Hsu Thazin Myint, and Ms Myat Su Tun.

This work is financially supported by the Science Achievement Scholarship of Thailand (SAST), Thailand Center of Excellence in Physics (ThEP), and The Research Network NANOTEC (RNN) program.

Last but not least, I could not complete this journey without huge and never-ending encouragement and supports from my parents, namely Mr. Sao and Mrs. Jittra Borsup. Thanks for their understanding all circumstance during the course of my study, which was quite often not easy. So, they never pressured me to follow my dreams to the end. Many thanks to my beloved family.

Jongrak Borsup



CONTENTS

	Page
ABSTRACT IN THAI.....	I
ABSTRACT IN ENGLISH.....	III
ACKNOWLEDGEMENTS	V
CONTENTS.....	VII
LIST OF FIGURES	X
LIST OF TABLES.....	XVI
CHAPTER	
I INTRODUCTION	1
1.1 Background and motivation.....	1
II LITERATURE REVIEWS.....	6
2.1 Ferromagnetic materials and hysteresis loop.....	6
2.2 Properties of LTP-MnBi.....	10
2.2.1 Crystal structure.....	10
2.2.2 Magnetic property	14
2.2.2.1 Coercivity (H_c).....	14
2.2.2.2 Energy product (BH) _{max}	16
2.2.2.3 Curie temperature.....	19
2.3 Synthesis techniques for LTP-MnBi	19
2.3.1 Chemical reaction method.....	21
2.3.2 Arc-melting or induction melting method.....	22
2.3.3 Melt spinning or rapid solidification.....	24
2.3.4 Sintering.....	26
2.4 Diffusion.....	29
2.5 Stability of magnetic materials	32

CONTENTS (Continued)

	Page
III EXPERIMENTEL METHOD	36
3.1 LTP-MnBi synthesis	36
3.1.1 Ball milling and sieving	36
3.1.2 Sintering in vacuum	37
3.1.3 Preparation of cross-sectional sample for SEM/EDS.....	38
3.2 Materials characterizations.....	40
3.2.1 X-ray diffraction (XRD).....	40
3.2.2 Scanning electron microscopy (SEM).....	42
3.2.3 Energy dispersive spectroscopy (EDS).....	44
3.2.4 Vibration Sample magnetometer (VSM).....	46
3.2.5 X-ray absorption spectroscopy (XAS).....	48
3.3 Experimental procedures	52
IV RESULTS AND DISSCUSSION	58
4.1 LTP-MnBi sintered at 275, 325 and 375 °C for 12 hours	59
4.1.1 Phase identification.....	59
4.1.2 Morphology and size distribution	62
4.1.3 Magnetic properties	64
4.1.4 Depth profile and diffusion in MnBi layers.....	68
4.2 LTP-MnBi sintered at 325 °C for 12, 24 and 48 hours	75
4.2.1 Phase identification.....	75
4.2.2 Magnetic properties	77
4.2.3 Diffusion in MnBi layers.....	80
4.3 Long-term stability of LTP-MnBi	83
4.3.1 Magnetic properties	84

CONTENTS (Continued)

	Page
4.3.2 Surface morphology of LTP-MnBi powder	85
4.3.3 Phase identification	87
4.3.4 Local structure of Mn atoms.....	89
4.4 Decomposition of MnBi at 150 °C	94
4.4.1 Surface morphology and chemical composition	94
4.4.2 Phase identification	98
4.4.3 Chemical composition.....	98
4.3.4 Magnetic properties.....	101
V CONCLUSION AND FUTURE RESEARCH	103
5.1 Conclusions	103
5.2 Future works.....	104
REFERENCES	106
CURRICULUM VATAE	115

LIST OF FIGURES

Figure	Page
2.1 A magnetic material with random domain orientation and aligned domain orientation by magnetization	7
2.2 A hysteresis loop of ferromagnetic materials.	8
2.3 Dependence of a rotation magnetic domain with an external magnetic field.....	9
2.4 Development of magnetic materials for fabricating permanent magnets in the last 100 years.	10
2.5 Crystal structure of LTP-MnBi.....	11
2.6 Rietveld refinement of XRD pattern for annealed $Mn_{52}Bi_{48}$ ribbons.....	13
2.7 Temperature-dependent coercivity of anisotropic MnBi powders ground for 3 hrs and 7 hrs The Insert shows M-H curves of MnBi powder with a different grinding time at 300K.....	14
2.8 Demagnetization curves of (a) anisotropic $Mn_{55}Bi_{45}$ and (b) $Mn_{60}Bi_{40}$ bonded magnets under various tested temperatures.....	15
2.9 Temperature-dependent M-H loops of MnBi ingots annealed for 8 hrs at 535K; the inset shows the M-H loops acquired at 650K.....	16
2.10 Temperature dependence of the theoretical $(BH)_{max}$ compared with the experimental $(BH)_{max}$ of LTP-MnBi and Nd-Fe-B.....	18
2.11 Mn-Bi phase diagram.....	19
2.12 Summary of LTP- MnBi preparation with various techniques	27
2.13 Types of sintering.....	28
2.14 Various sintering mechanism	29
2.15 Illustration of Fick first law.....	30

LIST OF FIGURES (Continued)

Figure	Page
2.16 LTP content $\delta(t_a)$ of MnBi as a function of annealing time. The diffusion coefficients $D = 1 \times 10^{-12}$ (dotted) and 2×10^{-12} cm ² /s (solid). The square is the calculated results by endo peaks of the cycled DSC trace. The insert shows the VSM loops of MnBi powder ground from arc-melting (square), the 300 °C/3 hr (circle) and 300 °C/30 hr (line)	31
2.17 Magnetic Hysteresis loop of LTP-MnBi thin film as fabricated (Test 1) and after 14-days exposure to air (Test 2)	32
2.18 Magnetic Hysteresis loop of LTP-MnBi thin film before and after degradation (a) and XRD diffraction after growth and 4 months (b).....	34
3.1 The graphical representation showing the procedures for preparing the mixture of Mn and Bi powders before sintering.....	37
3.2 (a) A schematic diagram and (b) photo of an in-house made sintering system.....	38
3.3 Graphical representation for the resin embedded with MnBi and sandwiched between microscope cover glasses	39
3.4 Target surfacing system	40
3.5 Argon ion beam slope cutting device (EM TIC 3X, Leica, Germany) at the Thailand Science Park.....	40
3.6 Schematic diagram showing X-ray diffraction from an atomic plane	41
3.7 X-ray diffractometers used in this work: (a) Bruker D2 phaser, (b) Bruker D8 ADVANCE, and (c) Rigaku Smart lab diffractometers	42
3.8 Principle of SEM operation.....	43
3.9 Interaction of an electron beam with specimen.	43
3.10 Principle of EDS.....	44
3.11 MnBi powder spectrum of the EDS analysis.	45
3.12 (a) SEM/EDS (JEOL JSM-6010LV) and (b) FE-SEM/EDS (JSM-7800F Prime).....	46
3.13 VSM schematic.	47

LIST OF FIGURES (Continued)

Figure	Page
3.14 VSM (Quantum Design Inc., VersaLab series) was used at Khon Kaen University.	47
3.15 Fundamental processes of X-ray absorption, showing the excited state (a), fluorescent X-ray emission (b), and Auger emission (c) at the relaxation to ground state.	50
3.16 Schematic diagram of the synchrotron light source at SLRI.	51
3.17 A schematic of the beamline 5.2 at SLRI.	51
3.18 Flow-chart of the experimental procedure for the study of the magnetic properties, crystal structure, morphology, and elemental composition of the LTP-MnBi material sintered in vacuum at temperature range of 275-375 °C.	53
3.19 Flow-chart of the experimental procedure for the study of the formation mechanism of the sintered LTP-MnBi material sintered in vacuum at temperature range of 275-375 °C.	54
3.20 A standard Quantum Design powder sample holder.	55
3.21 Diagram of long-term stability of LTP-MnBi material at different aging time, including MnBi characterization.	56
3.22 Diagram of a magnetic degradation with an evaluated heating time in ambient oven, including MnBi characterizations.	57
4.1 XRD patterns of LTP-MnBi powder prepared at various annealing temperature at 275 °C, 325 °C and 375 °C for small particle size of (a) < 20 μm and (b) 20-53 μm.	61
4.2 SEM images of the MnBi samples sintered at 275 °C with particle sizes of (a) < 20 μm and (b) 20-53 μm. The inset in (a) is the Bi/Mn ratio obtained from the EDS analysis of three specific locations.	63

LIST OF FIGURES (Continued)

Figure	Page
4.3 The M-H curves with demagnetizing field correction of the MnBi samples sintered at 275, 325 and 375 °C for particle sizes of (a) < 20 μm and (b) 20-53 μm. The inset in (a) shows the demagnetization curves of raw M (N = 0), corrected M (N = 0.4), corrected B (N = 0.4) of the small MnBi sintered at 325 °C. The $(BH)_{max}$ is the dashed rectangle with maximum area.....	65
4.4 M-H curves measured at sample temperature of 300K, 350K and 400K for the fresh and 10-month-old MnBi samples sintered at 275 °C showing the increase of coercivity with temperature.....	68
4.5 The cross-sectional SEM images of (a) as-received Mn powder particle (b) Mn powder particles sintered at 275 °C (c) at 325 °C and (d) at 375 °C..	69
4.6 (a) Zoom-in cross-sectional SEM image of the MnBi sintered at 325 °C. Inset illustrates the side-view schematic which may yield to different forming thickness between each side of the crack. (b) The Bi and Mn concentration profiles along the yellow line of (a).....	70
4.7 Histograms of the thickness of MnBi layers in the MnBi samples sintered at 275 °C, 325 °C and 375 °C. Each bin of the histogram is 0.05 micron.....	72
4.8 Arrhenius plot of the diffusion coefficient as a function of inverse temperature.....	74
4.9 XRD patterns of the MnBi samples with (a) small particle size (< 20 μm) and (b) large MnBi particle sizes (MnBi 20-53 μm). The MnBi samples were sintered at 325 °C for 12, 24, and 48 hrs.....	76
4.10 Room temperature M-H curves with demagnetization field correction of (a) the small MnBi particle size and (b) large MnBi particle size samples sintered at 325 °C for 12, 24, and 48 hrs.....	78
4.11 The energy product, $(BH)_{max}$, of the MnBi samples with particle sizes less than 20 μm as a function of sintering time.....	79

LIST OF FIGURES (Continued)

Figure	Page
4.12 a) A cross-sectional MnBi powder at 325 °C for 48 hr was prepared by ion beam slope cutting device and the zoom-in SEM images of a cross-sectional MnBi powder in the (b) 325 °C_12hr, (c) 325 °C_24hr, and (d) 325 °C_48hr at nearly the crack, respectively	81
4.13 Histogram of the thickness of MnBi layers in the (a) 325 °C_12hr, (b) 325 °C_24hr, and (c) 325 °C_48hr. Each bin of the histogram is 0.05 μm.....	81
4.14 Comparison of calculating MnBi layer thickness in the 1 st order diffusion equation and experimental MnBi layer thickness prepared at 325 °C for 12hr, 24hr, and 48hr, respectively.....	82
4.15 Room temperature M-H curves with demagnetization field correction of the samples stored in a sealed tube up to 18 months	84
4.16 SEM images of (a) fresh and (b) 18-month-old MnBi powders. The particle size distribution of MnBi powders shown in (c) and (d). The red squares in (a) and (b) are the areas for EDS measurements to determine the elemental composition, as shown in (e).....	86
4.17 XRD patterns of the fresh and 18-month-old LTP-MnBi showing at different 2θ ranges (a) 20-60 deg. (b) 27.79 – 30 deg. and (c) 32 – 44 deg. ...	88
4.18 (a) Theoretical K-edge XANES spectra of MnO (cal.) and MnBi (cal.), (b) the comparison of theoretical XANES spectrum for MnBi+MnO and experimental XANES spectrum of fresh MnBi, respectively, (c) Mn K-edge XANES spectra of LTP-MnBi and standard samples, (d) Fourier transform of EXAFS spectra of previous samples (fresh MnBi, old MnBi, and standard samples).....	91
4.19 Discussion: a relationship of the maximum energy product and diffusion length with a difference period	94

LIST OF FIGURES (Continued)

Figure	Page
4.20 SEM images of LTP-MnBi powder heated at 150 °C at different duration; (a) 0, (b) 0.5, (c) 3, (d) 6, (e) 12, (f) 24, and (g) 48hr. Inset shows their corresponding colors of all samples, and the specific points of EDS analysis (A, B, C, and D) in (h).....	96
4.21 (a) X-ray diffraction patterns of LTP-MnBi powder heated at 150 °C for different duration. (b) The zoom-in patterns of selected conditions revealing several forms of impurities.....	97
4.22 The Mn K-edge XANES spectra of MnBi powder heated at 150 °C for different duration. Dashed lines represent MnO, Mn ₂ O ₃ and calculated MnBi spectra.	99
4.23 (a) Room temperature M-H curves with demagnetization field corrector of MnBi powder heated at 150 °C for different duration. (b) Extracted saturation magnetization (M_s), coercivity (H_{ci}) and the calculated energy products ($(BH)_{max}$).....	100

LIST OF TABLES

Table	Page
2.1 Summary of Rietveld analysis on Mn ₅₂ Bi ₄₈ alloy prepared in melted-spinning with different processing step	12
2.2 Refined structural parameters and magnetic moment of MnBi with various annealing temperatures from 10 to 700K.....	13
2.3 The coercivity of MnBi ingot at different temperatures.....	16
2.4 Summaries magnetic properties of MnBi (M), NdFe (N) and MnBi/NdFeB (H) with 20 wt% bonded magnet at different temperatures.....	18
2.5 Variables affecting sinter-ability and microstructure	28
2.6 The saturated magnetization (emu/g at 1 T) after heat treatments for the MnBi samples with different particle sizes. It is noted that, before the heat treatment, the saturation magnetization is about 63 emu/g.....	35
4.1 The weight percentage of MnBi content and magnetic behaviors of all sintered MnBi sample	66
4.2 The mean, standard deviation, diffusion length, and diffusion coefficient of MnBi prepared by different sintering temperatures	74
4.3 The mean, standard deviation, and the maximum MnBi layer thickness prepared at different sintering time.....	82
4.4 Magnetic properties (H_c , M_s , $(BH)_{max}$) of MnBi sample at different ages or storing periods	85

CHAPTER I

INTRODUCTION

1.1 Background and motivation

Permanent magnets can maintain magnetic flux in the absence of an external magnetic field. This suggests that a permanent magnet has the potential to generate energy. They play an important role in modern technology related to energy conversion (Mohapatra and Liu, 2018). Permanent magnets are commonly used in everyday life, such as refrigerator magnets, dynamos, motors, sensors, and transducers as well as storage devices. In modern world, environment becomes important issue. There are increasing demands for high-performance permanent magnets in environmentally friendly technologies such as high-performance permanent magnet motors for hybrid and electric vehicles, performance dynamo for wind turbine, and future magnetic refrigerators and magnetic air conditioners

Nd-Fe-B and Sm-Co magnetic materials have long popularity over time in the permanent magnet industry due to their properties superior to other magnetic materials such as high energy product ($(BH)_{max}$) and low cost. However, these materials containing rare earths and thus have obvious disadvantages, such as poor corrosion resistance, loss of magnetic properties when the temperature rises (Li et al., 2018). In addition, according to a 2011 US Department of Energy report (Energy, 2010), rare earth elements, particularly Nd and Sm, are in critical supply. Mining of these elements lead to environmental problems. To alleviate such problems, rare earth free permanent magnets are therefore an option. Although the theoretically predicted $(BH)_{max}$ values for rare earth free magnetic materials are less than that of rare earth magnetic materials, the aforementioned disadvantages of rare earth magnets provide additional incentives and attract more attention to research and develop rare earth permanent magnets (Patel, Zhang and Ren, 2018).

Low-temperature phase Manganese Bismuth (LTP-MnBi) is a rare-earth-free ferromagnetic material with high coercivity and large positive temperature coefficient (Li et al., 2018; Liu, Wang and Dong, 2018), which are the desired properties for magnetic materials to be used for producing permanent magnets operating at relatively high temperature (Yang et al., 2002). LTP-MnBi is also a promising material to be as a hard phase in permanent magnet nanocomposites (Yang et al., 2002). In the recent decades, great efforts of many research groups have been devoted to the synthesis of the single phase LTP-MnBi compound. It has been theoretically predicted that its $(BH)_{max}$ could be as high as 17.7 MGOe at 300 K (Park et al., 2014). There has been reports that the single phase LTP-MnBi nanoparticles could be produced via chemical techniques with a high remanence ratio (M_r/M_s) and high coercivity (H_c) (Kirkemide, Shen, Gong, Cui and Ren, 2015; Liu et al., 2018; Rama Rao, Gabay, Hu and Hadjipanayis, 2014; J. Sun et al., 2016). Arc-melting or melt-spinning process with subsequent grinding and thermal annealing has been employed to synthesize relatively high-purity LTP-MnBi over 90 wt%. The experimental value of the $(BH)_{max}$ of the magnetically aligned samples was reported to be 50–86% of the theoretical value with an H_c of 7.11–18.2 kOe at room temperature.

It has been demonstrated that MnBi powders with H_c values up to 3.4 kOe could be prepared by sintering at 700 °C under helium ambient (Adams, Hubbard and Syeles, 1952). There has also been a report that the magnetically aligned MnBi samples sintered at 1000 °C in an argon atmosphere exhibited a considerable H_c of 14 kOe (Yang et al., 2002). Despite being a simple method, high-temperature sintering still requires high energy and post-sintering treatments because of the formation of high-temperature phase MnBi (HTP-MnBi) at temperatures above 350 °C (Jun Cui et al., 2018). Therefore, low-temperature sintering method was applied to avoid such difficulties. Magnetically aligned MnBi with a reported H_c of about 16 kOe has been produced by sintering at 1000 °C for 10 days under high pressure in an evacuated glass capsule (Kishimoto and Wakai, 1977). A spark plasma sintering followed by long-term annealing in argon gas (up to 28 days) was also used to produce MnBi powder with H_c of 5.7 kOe (Ko, Choi, Yoon and Kwon, 2007).

Synthesis of single phase LTP-MnBi by sintering is very challenging due to its complex phase diagram resulting in segregation of Mn from MnBi during a peritectic reaction as well as the formation of HTP-MnBi upon cooling down (T. Chen, 1974). Hence, the unreacted Mn and Bi phases are commonly detected along with the LTP-MnBi phase (J. Cao et al., 2019). Owing to the low melting point of Bi (~271 °C) compared to Mn (~1246 °C) (Antonov and Antropov, 2020), the formation of LTP-MnBi at temperature above the Bi melting point involves the rearrangement of Mn powder particles in liquid Bi, liquid–solid interactions at the liquid–solid interface and diffusion of Bi into the bulk. Details of solid–liquid diffusion and isothermal solidification in several metals in a transient liquid phase during sintering were studied (Corbin and Mclsaac, 2003). It is natural to explore possible ways in which large-scale MnBi might be synthesized by exploiting the solid–liquid diffusion mechanism. The minimum sintering temperature is determined by the eutectic temperature (262 °C, at which Bi-rich liquid \rightarrow Bi + MnBi) where the peritectic temperature (359 °C, Mn1.08Bi + Bi-rich liquid \rightarrow MnBi) is the upper limit (Si et al., 2019). So, the temperature range between 262 and 359 °C is considered to be optimal between the highest diffusion rate and the lowest HTP-MnBi formation. Analytical treatment of the sintering process in this temperature range is difficult because of the coexistence of vapor, liquid and solid phases: they must treat at once solubility, viscosity and diffusivity (Gupta, Anil Kumar and Khanra, 2018). But by assuming that the diffusion process is the rate-limiting mechanism of MnBi formation, recent research has reported that the diffusion coefficient of 1×10^{-12} cm²/s at an annealing temperature of 300 °C, which was deduced from the SEM observations of the decrease in size of Mn inclusions in the bulk LTP-MnBi prepared by arc-melting process (Van Nguyen and Nguyen, 2017). This value is rather high and, thus, not applicable for explaining the diffusion during MnBi formation by sintering, which obviously occurs at much smaller formation rate.

It is essential that the magnetic stability is one of the most important factors shall fully be investigated prior to launching a new type of permanent magnet. Generally, the magnetic properties were degraded mainly due to the oxidation (Janotová, Švec, Matko, Janičkovič and Sr., 2018; Ly et al., 2014; Villanueva et al., 2019) and decomposition (Ly et al., 2014; Sun, Xu, Liang, Sun and Zheng, 2016) upon

experiencing to humidity (Jacobson and Kim, 1987) and elevated temperatures (S. Cao et al., 2011; Y.-C. Chen et al., 2015; J. Cui et al., 2014; Zhang et al., 2014) for an extended period of time. It was found that the magnetic performance of LTP-MnBi could be degraded even in ambient atmosphere with different rates depending on its physical forms or shapes. Sun et al. reported the magnetic degradation in ambient atmosphere at room temperature of the LTP-MnBi thin film prepared by magnetron sputtering system. They found a 35% saturation magnetization (M_s) reduction with slight coercivity (H_c) enhancement after exposure to air for 14 days. These behaviours were explained by the oxidation of Mn and the weakened inter-grain exchanges at grain boundaries (M. Y. Sun et al., 2016). Villanueva et al. also reported that the ferromagnetic property of LTP- MnBi thin film prepared by DC-magnetron sputtering were reduced for up to 54% and 100% after exposing to the air for 6 days and 4 months explained by the MnBi phase disappearance (Villanueva et al., 2019). The dramatic degradation in the melt-spun LTP-MnBi ingot were reported after exposing to the air for 7 days which were explained by the Mn oxidation leading to the MnBi decomposition (Ly et al., 2014). The magnetic phase content of MnBi ribbon flakes decreases after exposure to ambient atmosphere for 1 year respected to oxidation. A chemical composition of surface sample was investigated by EDS map. They found Bi-rich phases segregate after 6 months and the top of master alloy surface is covered by oxygen layer (Janotová et al., 2018).

Several techniques, such as surface modifications and surface capping, have been utilized in order to stabilize the magnetic performance of LTP-MnBi. The aim of such modifications is to prevent the MnBi from oxidation and decomposition. For example, Sun et al. found that their Ta capped MnBi were significantly more stable than the bare MnBi. The H_c and M_s were kept unchanged after 14-day exposure to air (M. Y. Sun et al., 2016). The cross-sectional MnBi bulk prepared by zone-melting in a He atmosphere was studied. It does not slightly exhibit oxidation after exposure to air more than 1 year due to nearly Mn free-MnBi ingot (Yoshida, Shima, Takahashi and Fujimori, 1999).

This thesis work focused on the investigation of LTP-MnBi sintered in vacuum at low temperature. The crystal structure, morphology, and the magnetic properties of the sintered LTP-MnBi were studied. More importantly, this is the first time to carry out in-depth investigation of the formation mechanism for LTP-MnBi prepared by low-temperature sintering in vacuum and thermal stability of the sinter MnBi. It was expected that the diffusion process is the main factor for controlling the LTP-MnBi layers formed during sintering. In this work, a new approach was adopted to determine the diffusion coefficient in sintered LTP-MnBi powder particles from the results taken by energy dispersive spectroscopy (EDS) line scan measurements of cross-sectional MnBi powder particles. The long-term magnetic stability at room temperature and decomposition at elevated temperature of the vacuum sintered LTP-MnBi samples were also investigated for the first time. The details of magnetic properties, crystal structure and chemical composition were obtained by various material characterization techniques.

CHAPTER II

LITERATURE REVIEWS

This chapter provides information as the background for the investigations of formation and magnetic properties of LTP-MnBi, long-term thermal evolution at room temperature of magnetic properties, and decomposition of LTP-MnBi at elevated temperature. Since hysteresis loop (M-H curve) is generally used for describing magnetic properties, thus, it will be first mentioned. The information of MnBi such as phase diagram and crystal structure are provided. Different synthesis techniques for MnBi, including liquid-phase sintering (LPS) used in this thesis work, are described. Most importantly, the 1st order diffusion law is given as the basis for explaining the formation of LTP-MnBi during LPS.

2.1 Ferromagnetic materials and hysteresis loop

Among various types of magnetism, ferromagnetism is the strongest type. More importantly, ferromagnetic materials are the materials which exhibit a spontaneous net magnetization at the atomic level, even without an external magnetic field. These materials could attain permanent magnetism. This property is of great importance for fabricating of permanent magnets, which are widely used in many different kinds of devices such as an electric motor, generators, loudspeakers, magnetic sensors, magnetic stripe at the back of credit cards.

Magnetism of magnetic materials can be explained by a concept of magnetic domain. This magnetic domain or domain is a small region with all atomic dipoles pointing in the same direction when the materials are in the unmagnetized state. Thus, each domain exhibits a net magnetic moment even though there is no external magnetizing field. There are many domains in magnetic materials. The magnetic moments of the domains are oriented in opposite directions in such a way that they cancel out, resulting that zero net magnetic moment of the material.

When an external magnetic field is applied, all magnetic domains in ferromagnetic materials align themselves in the direction of the applied field. In this case, the material is strongly magnetized in a direction parallel to the magnetizing field, as shown in Figure 2.1. It is well understood that ferromagnetic materials are strongly magnetized in the direction of the field when placed in an external magnetic field. Therefore, ferromagnetic materials strongly interact with magnetic field, or are attracted to a magnet. The ferromagnetic materials will retain their magnetization for some extended duration even after removing the external magnetizing field. This property is called hysteresis.

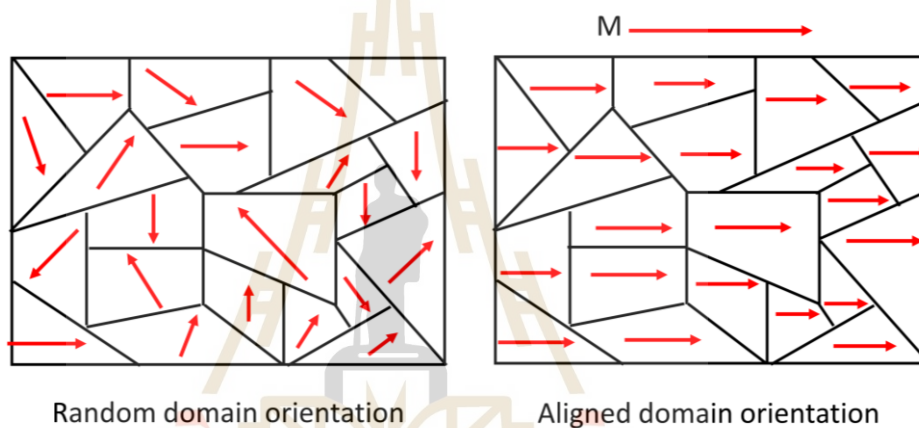


Figure 2.1 A magnetic material with random domain orientation and aligned domain orientation by magnetization.

Magnetic properties of magnetic materials are, in general, described by a graph showing the relationship between magnetic flux density (B) and magnetic field intensity (H), as shown in Figure 2.2. This is known as an induction hysteresis loop or B - H curve or M - H curve, where the magnetization $M = B/\mu - H$ and μ is the magnetic permeability. The graph shows the changes from the beginning where the material has no magnetic flux (B is zero) and the magnetic field H is zero. As the magnetic material is magnetized, the H magnetic field increases, the magnetic flux B will increase along the dotted line until H reaches a certain value and the value B will not increase again, that is the magnetization reaches the saturation point is reached (position 1 in the figure). When the magnetic field H is reduced to zero, the value of magnetic flux B has decreased accordingly. The path from position 1 to position 2 can be seen that the value B has

changes in the shapes of the magnetic domains occur. Increasing magnetic force leads to a growth of favorable domains and shrinkage of unfavorable domains. The domain grown by domain wall movement while the magnetic moments in the domains remain unchanged. With small magnitude of the H field, the original shapes of the domains could be restored when the H field is removed. This region of the H field allows reversible magnetic domain wall motion. However, when the H field exceeds a critical value, the magnetic domain wall motion is irreversible. That is the original shapes of the domains cannot be restored when the H field is removed. Further increase of the H field causes the rotation of the magnetic moments in the domains, called magnetization rotation. The magnetization forces the magnetic moment to align with the H field. It is noted that the energy required for the domain growth is less than the magnetization rotation energy. Up to the saturation magnetization, all magnetic dipoles are aligned with the H field resulting in a single magnetic domain with magnetic moment in the same direction of the H field.

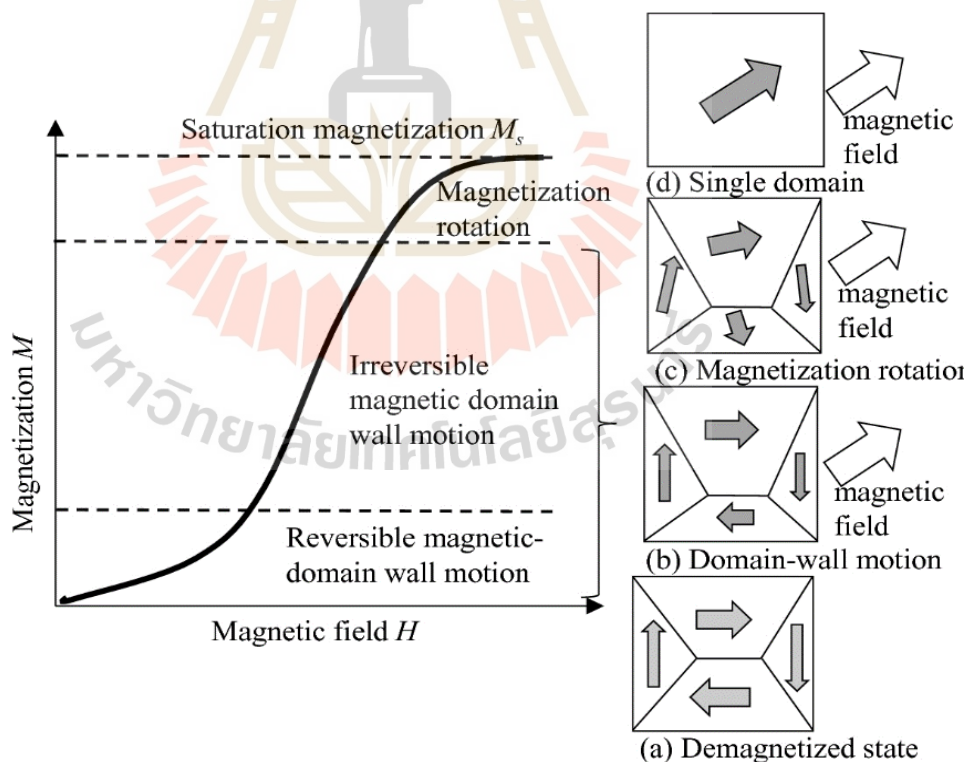


Figure 2.3 Dependence of a rotation magnetic domain with an external magnetic field (Akagi, 2019).

High performance permanent magnets exhibit a high magnetic field (high retentivity or remanence) and high coercivity, results in a high maximum energy product, $(BH)_{max}$, which is an performance indicator for permanent magnets (Kramer, McCallum, Anderson and Constantinides, 2012). The development of magnetic materials to increase the performance or $(BH)_{max}$ value of permanent magnets is shown in Figure 2.4. It is obvious that, for over 50 years, high performance permanent magnets are produced from rare earth materials. These magnets include samarium-cobalt (Sm-Co) magnets and Nd-Fe B (NIB) magnets prepared by mixing neodymium (Nd), iron (Fe) and boron (B). Up till now, the $Nd_2Fe_{14}B$ magnetic compound still has the highest $(BH)_{max}$ value of nearly 60 MGOe (Mohapatra and Liu, 2018), and is a widely used for producing permanent magnet.

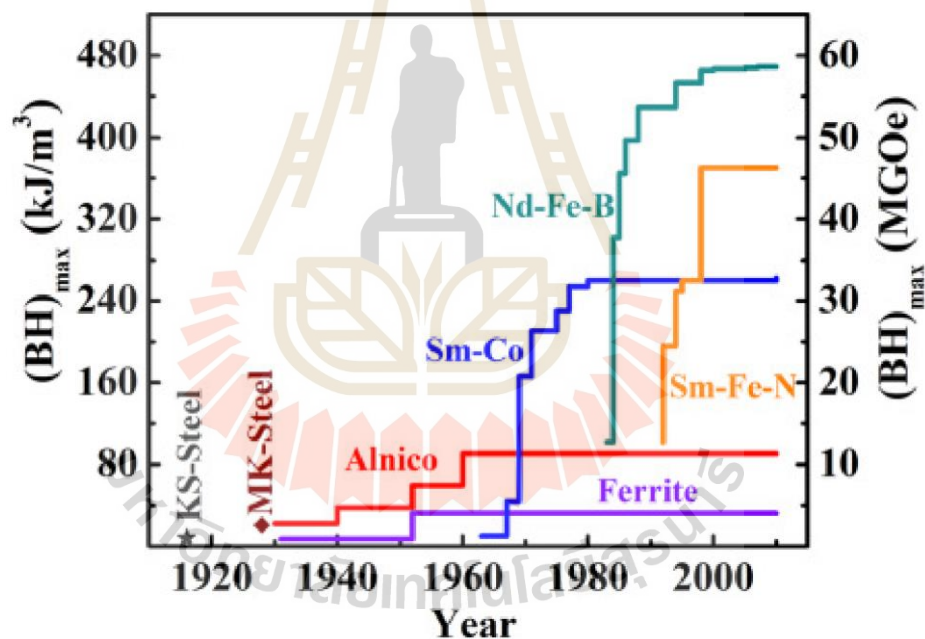


Figure 2.4 Development of magnetic materials for fabricating permanent magnets in the last 100 years (Mohapatra and Liu, 2018).

2.2 Properties of LTP-MnBi

2.2.1 Crystal structure

Mn is a 3d transition element with atomic number of 25. It exists in nature with different oxidation states, i.e., 0, +2, +3, +4, and +7. While Bi is a large atom with atomic number of 83 and plausible oxidation states of 0, +3 and +5. The electron configuration

in ground state of Mn and Bi are $1s^2, 2s^2, 2p^6, 3s^2, 3p^6, 4s^2, 3d^5$ and $1s^2, 2s^2, 2p^6, 3s^2, 3p^6, 4s^2, 3d^{10}, 4p^6, 5s^2, 4d^{10}, 5p^6, 6s^2, 4f^{14}, 5d^{10}, 6p^3$, respectively. Normally, metallic Mn is an antiferromagnetic at room temperature. However, when formed with other elements, the compounds become a strong ferromagnetic material (Jun Cui et al., 2018). Pure Bi is a non-magnetic material. The magnetic property of Bi is sensitive to its purity. Mn is more chemically reactive to oxygen than Bi (Villanueva et al., 2019). LTP-MnBi compound (α -MnBi or $Mn_{50}Bi_{50}$) has the hexagonal NiAs ($P6_3/mmc$) structure with a unit cell parameters $a = b = 4.290 \text{ \AA}$ and $c = 6.125 \text{ \AA}$ ($\alpha = \beta = 90^\circ, \gamma = 120^\circ$ respectively) at room temperature (Jun Cui et al., 2018). The crystal structure of LTP-MnBi is graphically shown in Figure 2.5 (Bandaru, Sands, Weller and Marinero, 1999).

Magnetic exchange coupling in MnBi leads to strong ferromagnetism. A coupling strength was influenced by the coupling intensity, which can be explained by Beth-Stater curve (Vuong, 2019). The coupling strength depends on the ratio λ between the interatomic distance and radius of d-shell (3-d orbital) of Mn atoms in the unit cell. For pure Mn (antiferromagnetic), the λ value is just below 1.5. This implies that increasing the separation between Mn atoms will favorably alter the ratio λ and leading to ferromagnetism. This evidence is realized by alloying Mn with Bi and the MnBi alloys become ferromagnetic. Based on reported data, the critical Mn-Mn distance is 2.83 \AA to induce ferromagnetism in the MnBi alloy (Vuong, 2019). Mn atoms can be easily oxidized in LTP-MnBi due to unpaired electrons in 3d orbits (Huang, Shi, Hou and Cao, 2019).

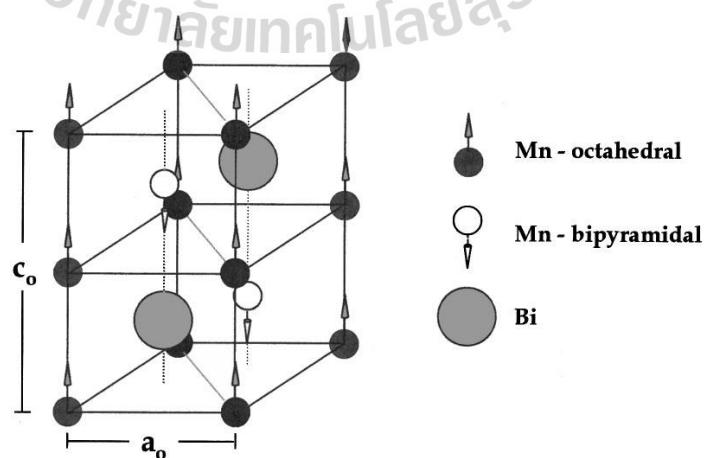


Figure 2.5 Crystal structure of LTP-MnBi (Bandaru et al., 1999).

The crystal structure of LTP-MnBi can be changed with increasing temperature to HTP, leading to a different magnetic behavior. LTP-MnBi displayed crystal structure of NiAs-hexagonal structure, exhibited a ferromagnetic behavior (Roberts, 1956) while HTP-MnBi (temperature > 628K) was a disordered Ni₂In-hexagonal structure with paramagnetic behavior (Vuong, 2019). The HTP-MnBi (β -MnBi) is Mn_{2.23}Bi_{1.88} with space group of Pm₃m at 630K. The lattice parameter of is $a = 5.959 \text{ \AA}$, $b = 4.33 \text{ \AA}$, and $c = 7.505 \text{ \AA}$ ($\alpha = \beta = \gamma = 90^\circ$), respectively (Jun Cui et al., 2018).

Jensen et al. (2019) reported the lattice parameter and phase fraction of Mn₅₅Bi₄₈ alloy prepared in melted-spinning with different processing step, which calculated from Rietveld refinement of XRD pattern as show in Table 2.1. The instance of Rietveld refinement was obtained by XRD pattern of Mn₅₅Bi₄₈ annealed ribbon pieces at 290 °C for 5 days are shown in Figure 2.6. The content of LTP-MnBi, Bi and MnO₂ are 98.2 wt%, 0.5 wt%, and 1.2 wt%., respectively.

Y. B. Yang et al. (2013) revealed a refined structural parameter and magnetic moment of MnBi with various annealing temperatures from 10 to 700K, as provided in Table 2.2. These results were measured by the neutron diffraction technique. They found that the lattice constants increase with increasing temperature. The highest c/a lattice parameter ratio is 1.433 at 600K. The nearest distance of the Mn-Mn bond is from 3.038 Å to 3.082 Å, which is larger than 2.754 Å for the Mn element.

Table 2.1 Summary of Rietveld analysis on Mn₅₂Bi₄₈ alloy prepared in melted-spinning with different processing step (Jensen et al., 2019).

Processing step	a, b (Å)	c (Å)	MnBi fraction (wt)	Bi fraction (wt)	Fitting (χ^2)
Annealed ribbon	4.28172(10)	6.11311(17)	0.9687(1)	0.0313(15)	10.620
Ball milled powders	4.28303(20)	6.11004(34)	0.9245(8)	0.0755(68)	3.808
Annealed powders	4.28133(13)	6.11081(21)	0.98501(7)	0.0149(28)	7.399

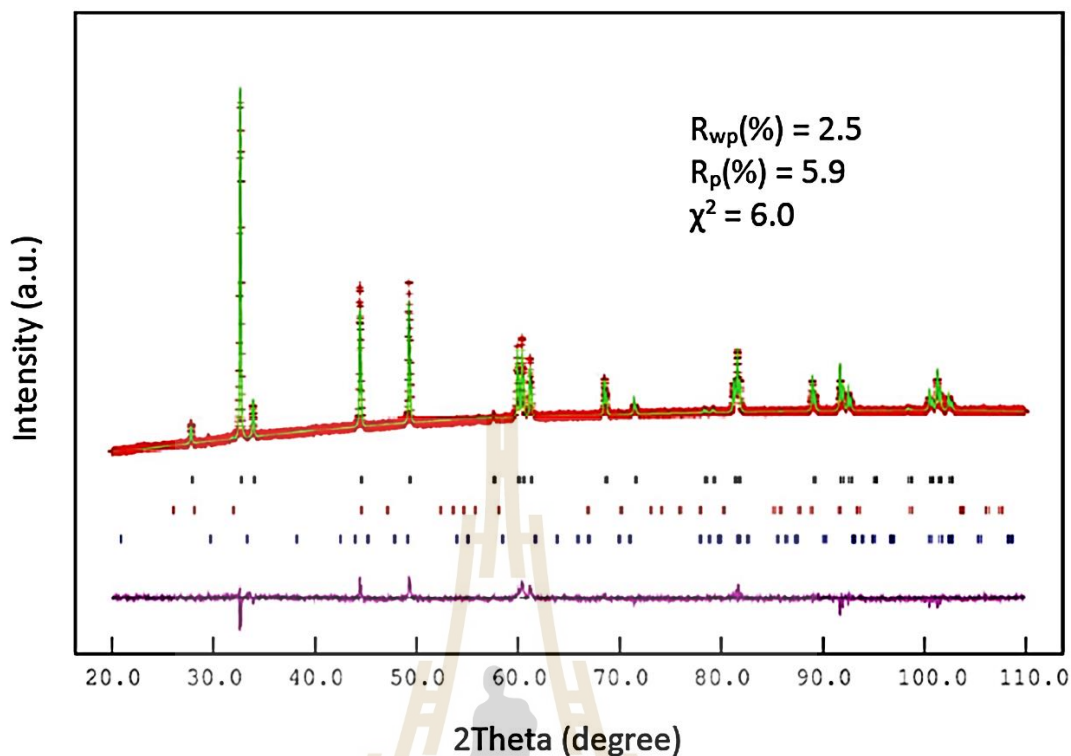


Figure 2.6 Rietveld refinement of XRD pattern for annealed $\text{Mn}_{52}\text{Bi}_{48}$ ribbons (Jensen et al., 2019).

Table 2.2 Refined structural parameters and magnetic moment of MnBi with various annealing temperatures from 10 to 700K (Y. B. Yang et al., 2013).

T (K)	a, b (Å)	c (Å)	c/a	V (Å ³ / Cell)	Mn–Mn (Å) ^a	Moment (μ_B) ^b	β (°) ^c
10	4.26902	6.07612	1.42331	95.899	3.0381	3.997	89.135
100	4.27364	6.09014	1.42505	96.328	3.0451	3.798	9.587
200	4.27831	6.10269	1.42643	96.738	3.0513	3.813	4.036
300	4.28541	6.12296	1.42881	97.381	3.0615	3.503	1.138
400	4.28952	6.13703	1.43072	97.793	3.0685	3.463	6.288
500	4.29531	6.15241	1.43325	98.302	3.0762	3.109	6.480
600	4.30072	6.16491	1.43346	98.751	3.0825	1.411	34.37
700	4.30919	6.17521	1.43303	99.306	2.9279	–	–

^a The nearest Mn–Mn distance.

^b Magnetic moment per Mn atom.

^c β indicates the angle between the magnetic moment of Mn atom and the c -axis.

2.2.2 Magnetic property

2.2.2.1 Coercivity (H_c)

There are several studies on temperature-dependent coercivity (H_c). Some reports revealed annealing temperature effects on the magnetic properties, while others reported temperature-dependent magnetic properties during VSM measurements. For example, magnetic properties are influenced by various annealing temperature (Y. B. Yang et al., 2013). They prepared MnBi by melted-spinning under Ar. The MnBi ribbons annealed at difference temperatures. They found the temperature dependence on the H_c of MnBi with a different grinding time, as seen in Figure 2.7. The highest H_c of MnBi with grinding time for 7 hr due to the reduction of MnBi powder, which close to single domain size of MnBi 250 nm. Moreover, the highest H_c of 1.2 T at room temperature after grinding time for 7 hr (see in insert of Figure 2.7). The all H_c of two samples exhibited a positive temperature coefficient and the highest H_c of 2.5 T at 540K and decreased slightly to 1.8 T at 610K.

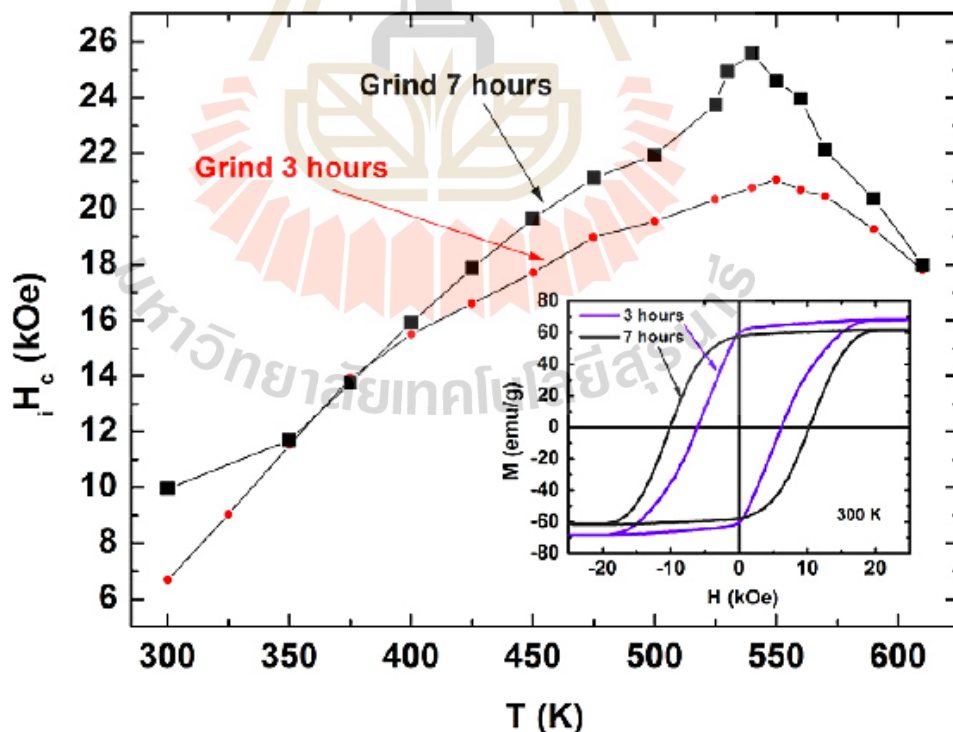


Figure 2.7 Temperature-dependent coercivity of anisotropic MnBi powders ground for 3 hrs and 7 hrs The Insert shows M-H curves of MnBi powder with a different grinding time at 300K (Y. B. Yang et al., 2013).

Temperature-dependent magnetic properties during VSM measurements. Jun Cao et al. (2018) demonstrated the temperature dependent on demagnetization curves of anisotropic $\text{Mn}_{55}\text{Bi}_{45}$ and $\text{Mn}_{60}\text{Bi}_{40}$ bonded magnets prepared by melted-spinning at 673K for 30 min. The resin bonded MnBi magnet was aligned with a magnetic field of 1.8T. Figure 2.8 shows the coercivity increases with increasing sample temperature. The H_c of anisotropic $\text{Mn}_{55}\text{Bi}_{45}$ ($\text{Mn}_{60}\text{Bi}_{40}$ bonded magnets) increases from 12.00 kOe (13.89 kOe) at 300 K to 17.26 kOe (18.36 kOe) at 380 K, respectively. The positive temperature coefficient of coercivity respond to the elevated coercivity.

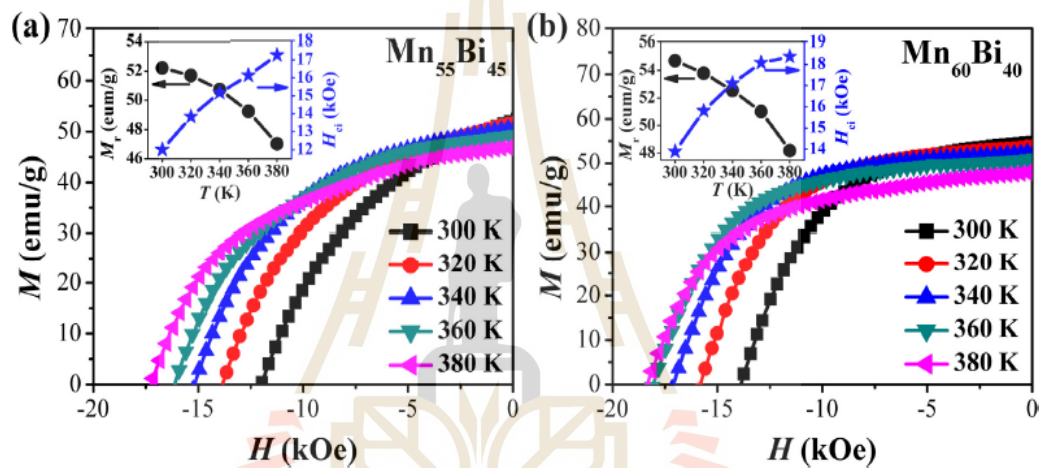


Figure 2.8 Demagnetization curves of (a) anisotropic $\text{Mn}_{55}\text{Bi}_{45}$ and (b) $\text{Mn}_{60}\text{Bi}_{40}$ bonded magnets under various measured temperatures (Jun Cao et al., 2018).

Additional, Huang et al. (2019) reported the temperature dependence on the M-H curves of MnBi ingot at 535 K for 8 hr, as shown in Figure 2.9, and the extracted magnetic properties of H_c , and J_r , as given in Table 2.3. The H_c of MnBi increases with increasing temperatures. The highest H_c of 21.97 kOe at 500 K is due to the positive temperature coefficient of coercivity. At 600 K, H_c of MnBi is 15.96 kOe but the shape of the M-H curve with paramagnetic pattern. The ferromagnetic LTP-MnBi transformed to the paramagnetic of HTP-Mn_{1.08}Bi when the temperature is increased to 650 K.

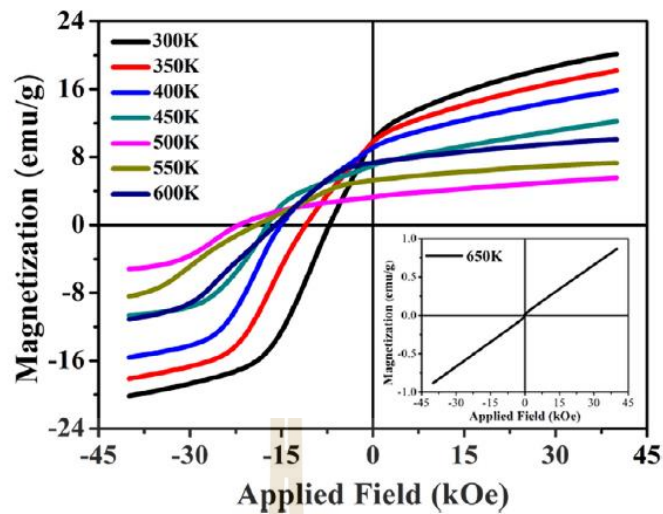


Figure 2.9 Temperature-dependent M-H loops of MnBi ingots annealed for 8 hrs at 535K; the inset shows the M-H loops acquired at 650K (Huang et al., 2019).

Table 2.3 The coercivity of MnBi ingot at different temperatures.

Temperature	300 K	350 K	400 K	450 K	500 K	550 K	600 K
H_{ci} (kOe)	7.11	11.01	15.07	17.28	21.97	19.06	15.96
J_r (emu/g)	9.9	9.8	9.1	7.0	3.3	5.3	7.3

2.2.2.2 Energy product $(BH)_{max}$

$(BH)_{max}$ is the maximum amount of magnetic energy stored in a magnet. The magnetic performance of LTP_MnBi depend on morphology, microstructure, particle size, and LTP-MnBi content, which are related to the preparation technique, production process and controlled environment (Borsup et al., 2022). Y. B. Yang et al. (2012) prepared MnBi by melted-spinning at various annealing temperatures (473-773K) and followed by grinding. The MnBi power was boned with an epoxy resin, and aligned in a magnetic file of 1.5 T. They found the $(BH)_{max}$ of the magnet was 7.1 MGOe at room temperature.

Kim et al. (2017) produced the MnBi bulk by melted spinning (the 98 wt% of content MnBi). The MnBi ribbons were coarsely ground and annealed at 300 °C under vacuum for 20 hr, and then magnetically separated. The MnBi particle was ground again by ball milling (time = 1, 2, 2.5 hr) and jet milling method.

The fine MnBi powder was compressed with magnetic alignment of 2 T and then the obtained MnBi bulk was sintered at 280°C. They found the highest $(BH)_{max}$ of 7.3 MGO at 280 °C for the 1 hr ball milled sample.

Y.-C. Chen et al. (2016) prepared MnBi by arc-melting at 300 °C under vacuum for 1-3 days and then took the sample to ball milling at room temperature for 2-12 hr. After that the sample was magnetically separated and pre-aligned at 1.8 T in cylinder die mode with hot compaction in vacuum (473K, 523K, 573K for 5 mins). They found the maximum $(BH)_{max}$ is 15.08 MGOe at room temperature, which is close to the theoretical $(BH)_{max}$ value (Park et al., 2014). The report $(BH)_{max}$ of magnetic aligned samples was 50–86% as compared to theoretical value and the H_c was 7.11–18.2 kOe at room temperature (J. Cao et al., 2019; Huang et al., 2019; Kim et al., 2017; X. Li, Pan, Zhen, Lu and Batalu, 2019; Y. B. Yang et al., 2012)

Park et al. (2014) studied temperature dependence of the $(BH)_{max}$ of the theoretical compared with the $(BH)_{max}$ of experimental LTP-MnBi and Nd-Fe-B, as shown in Figure 2.10. A formula is $(BH)_{max} = B_r^2/4$ was estimated in this work. They found MnBi increased from 1.7 MGOe at 100 K to 18.7 MGOe at 250 K and then slightly decreased to 6.2 MGOe at 600 K. The calculated $(BH)_{max}$ at 300 K is 17.7 MGOe, with is similar to the $(BH)_{max}$ of directionally solidified LTP MnBi (17 MGOe at 290 K). The sintered MnBi magnet shows $(BH)_{max}$ values of 7.8 MGOe and 5.8 MGOe at 300 K. The experimental values of all $(BH)_{max}$ are smaller than the estimated values. This was suggested to be the result from the imperfect rectangular demagnetization curve. Moreover, the calculated $(BH)_{max}$ of LTP-MnBi at 500K is 10.9 MGOe, which has higher value than that 2 MGOe of Nd-Fe-B, indicating that LTP-MnBi is a good permanent magnet for high temperature applications.

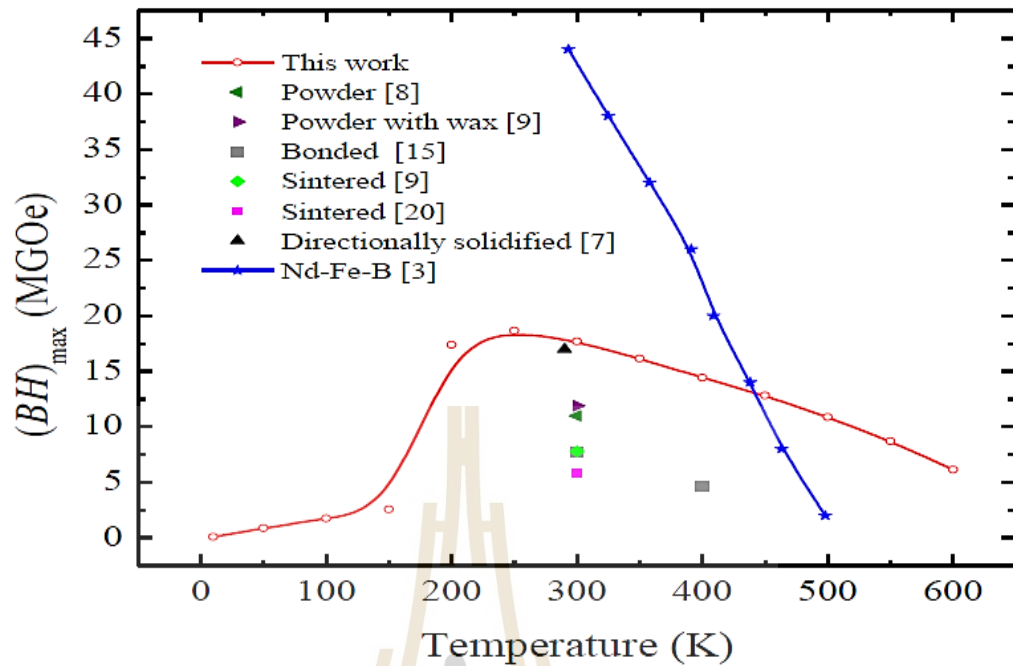


Figure 2.10 Temperature dependence of the theoretical $(BH)_{max}$ compared with the experimental $(BH)_{max}$ of LTP-MnBi and Nd-Fe-B (Park et al., 2014).

Additionally, the tendency of experimental $(BH)_{max}$ of the resin bonded MnBi powder show the similar tendency as a previous tendency of the theoretical $(BH)_{max}$ from 300K to 450K (S. Cao et al., 2011). At elevated temperatures, the $(BH)_{max}$ increased and gradually decreased from 2.25 MGOe at 298K to 1.6 MGOe at 423K, as show in Table 2.4.

Table 2.4 Summaries magnetic properties of MnBi (M), NdFe (N) and MnBi/NdFeB (H) with 20 wt% bonded magnet at different temperatures (S. Cao et al., 2011).

	298 K			323 K			373 K			423 K		
	N	H	M	N	H	M	N	H	M	N	H	M
Br(kGs)	6.24	6.55	2.82	6.18	6.02	2.74	5.8	5.57	2.65	5.37	5.01	2.47
Hci(kOe)	9.68	9.31	14.93	8.13	8.17	15.4	7.12	6.77	21.29	5.62	5.91	16.2
$(BH)_{max}$ (MGOe)	9.97	9.74	2.25	8.07	7.76	1.93	6.21	6.76	2.06	3.67	5.71	1.6

2.2.2.3 Curie temperature

Curie temperature is temperature above at which some materials lose their permanent magnetic properties. For a ferromagnetic material, it transforms to paramagnetic at temperature above the Curie temperature. Ferromagnetic LTP-MnBi can be transformed into HTP-paramagnetic MnBi at 628 K, the magnetization was dramatically dropped at 628 K (Park et al., 2014). This value of Curie temperature of LTP-MnBi is slightly smaller than the previous reported value of 633 K (Jun Cui et al., 2018).

2.3 Synthesis techniques for LTP-MnBi

In practice, synthesis of single-phase LTP-MnBi is technically difficult due to the huge difference in the melting points of Mn (1246 °C) and Bi (271 °C). The main problem is the dissociation of Mn due to the effect of the peritectic reaction between Mn and Bi. From the Mn-Bi phase diagram, as shown in Figure 2.11, peritectic reactions result in the formation of LTP-MnBi with an always excess of Bi (Truong and Nguyen, 2015).

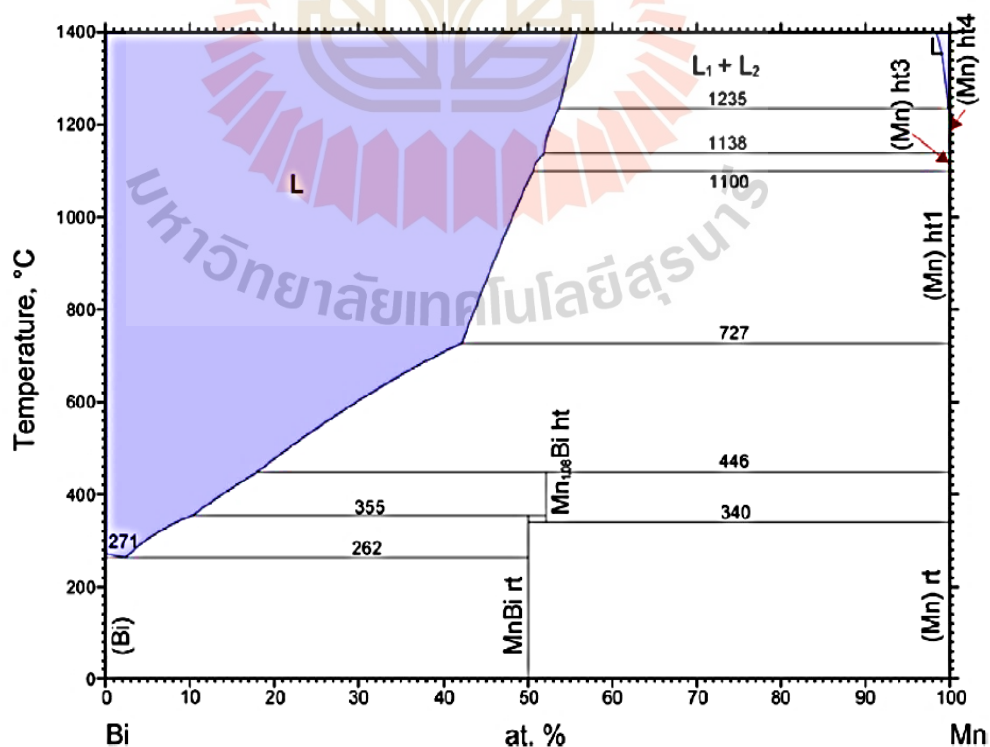


Figure 2.11 Mn-Bi phase diagram (J. Cui et al., 2014).

Figure 2.11 shows Mn-Bi phase diagram, corresponding with a various ratio of atomic percentage of Mn and Bi and temperature. This figure defined the atomic ratio of Mn:Bi (50:50 at%). The formation of MnBi occurred from the heating temperature over to the melting point of Bi. The peritectic reaction (1,2) and eutectic reaction (3,4) can explain MnBi formation at low temperatures phase to high temperature phase are summarized below.

- 1) At 628K (355 °C) upon heating, α -MnBi \rightarrow Mn_{1.08}Bi + Bi rich liquid
- 2) At 719K (446 °C) upon heating Mn_{1.08}Bi \rightarrow Mn + Bi rich liquid
- 3) At 613K (340 °C) during cooling Mn_{1.08}Bi \rightarrow α -MnBi + Mn
- 4) At 535K (262 °C) during cooling, MnBi + Bi \rightarrow Bi-rich liquid

The ferromagnetic to paramagnetic transition upon heating to 628 K and paramagnetic to ferromagnetic transition upon cooling to 613K, corresponding to phase decomposition of (1) α -MnBi \rightarrow Mn_{1.08}Bi + Bi rich liquid and (3) Mn_{1.08}Bi \rightarrow α -MnBi + Mn (Tu and Stutius, 1974). The minimum sintering temperature at LTP is determined by the (4) eutectic temperature and the (1) peritectic temperature (262 °C, Bi-rich liquid \rightarrow Bi + MnBi) where the peritectic temperature (359 °C, Mn_{1.08}Bi + Bi-rich liquid \rightarrow MnBi), The 340 °C is the limited temperature at LTP (Borsup et al., 2022).

The phase diagram of the Mn–Bi system near the compound MnBi was studied with single crystals in the as-grown and heat-treated states. The results show that the high-temperature phase of MnBi is in fact a separate compound with chemical formula Mn_{1.08}Bi, when grown from a Bi-rich solution. It was found that the transformation of MnBi at 355 °C upon heating is associated with a peritectic decomposition of MnBi into Mn_{1.08}Bi + liquid, and the transformation at 340 °C upon cooling of the high-temperature phase is the result of decomposition of Mn_{1.08}Bi to MnBi + Mn (T. Chen, 1974).

This challenge led to the development of techniques for synthesizing single phase LTP-MnBi magnetic particles. The commonly used techniques are summarized as follows.

2.3.1 Chemical reaction method

Nanoparticles may be synthesized by chemical technique with different processes such as, mechanochemical process, metal-redox method, facile aqueous solution method and wet chemistry reduction process. The advantage of chemical technique is an ease to produce MnBi nanoparticles, which exhibit high coercivity approaching the theoretical value. The drawback for this technique is the difficulty to upscale for mass production.

Rama Rao, Gabay, Hu and Hadjipanayis (2014) reported MnBi nanoparticles with size in a range between 100 and 300 nm. The particles were synthesized from a mixture of Bi_2O_3 and Mn powders in the process of Ca reducing element ($\text{Bi}_2\text{O}_3 + 2 \text{Mn} + 3\text{Ca} = 2\text{MnBi} + 3\text{CaO}$) by mechanochemical process. The materials from the reaction were then ground by using high-energy ball milling under Ar atmosphere for 4 hr. A two-step annealing has been used. In the first step, the sample was annealed at 1075K for 10 min and quenched, while the second step the sample was annealed at 575K for 15 hr. The heat-treated powders were washed to remove CaO and unreacted reactants with deionized water and 1 vol.% aqueous solution of acid and ethanal. Magnetic hysteresis loops (M-H hysteresis) of the field aligned powders were measured by VSM after magnetizing in a pulse field of 80 kOe. Temperature dependence of the magnetization was measured under a bias magnetic field of 1000 Oe. The nanoparticles exhibit high remanence ratio (M_r/M_s) of 0.94 and high coercivity (H_c) of 16.3 kOe at room temperature.

Kirkemide, Shen, Gong, Cui and Ren (2015) reported MnBi nanoparticles by metal-redox method with size in a range between 54 and 288 nm, the M-H hysteresis loop of the magnetic aligned MnBi nanoparticles display the saturation magnetization (M_s) of 49 emu/g, the remnant magnetization (M_r) of 43 emu/g, and coercivity (H_c) of 15 kOe.

J. Sun et al. (2016) reported Mn-Bi@Bi magnetic nano particles prepared by a facile aqueous solution method. The obtained MnBi exhibits a saturation magnetization (M_s) of 2.37 emu g^{-1} , coercivity (H_c) of 8 kOe at 5K and superparamagnetism at 300K.

Liu, Wang and Dong (2018) reported the sintering of a mixture of Mn and Bi nanoparticle synthesized by a wet chemistry reduction process.

Mn and Bi nanoparticle were mixed with hexane (ratio 1:1) and annealed at 250 °C under Ar atmosphere. The annealing time was controlled to be 2, 4, 6 and 8 hr. M-H hysteresis of the magnetic field aligned up to 3 T were measured by VSM. The coercivity is more than 8 kOe for the sample with annealing times of 6 and 8 hr.

2.3.2 Arc-melting or induction melting method

Arc-melting is used for melting metals (alloy) by an electric arc struck between a tungsten electrode and metals placed in copper hearth. Induction heating is the process of heating by electromagnetic induction, through heat generated in the electrically conducting object by eddy currents.

Zhang et al. (2011) reported the study of bulk nanostructural $Mn_{100-x}Bi_x$ ($x= 40, 45, 52$) permanent magnets (~93 wt%) prepared by spark plasma sintering technique (SPS). The bulk $Mn_{100-x}Bi_x$ was prepared by induction melting. The ingots were annealed at 573K for 10 hr, and then crushed and ball milled for 4 hr in a high-energy ball mill. Using spark plasma sintering techniques, the samples were sintered at 573K with a heating rate of 50 K/min. The obtained product was $Mn_{55}Bi_{45}$ magnet exhibiting coercivity of 12 kOe at room temperature. The $Mn_{48}Bi_{52}$ magnet shows a rather high coercivity of 19 kOe at 423K. $Mn_{48}Bi_{52}$ magnet is composed of fine and uniform grains with an average size of 140 nm.

Rama Rao, Gabay and Hadjipanayis (2013) reported the investigation of an MnBi magnet prepared by hot compaction. The MnBi ingot was prepared by arc-melting. The ingots were annealed at 573K for 24 hr, and then crushed and ground by low energy ball milling (LEBM), the milled powders were compacted with aligned magnetic field of a 1.8 T and the green compacts were placed to hot compaction at 593K for 10 min. VSM was employed to study the magnetic properties after magnetizing in a pulse field of 80 kOe. Highly anisotropic MnBi powders show very high remanence ratio (M_r/M_s) of 0.97, coercivity (H_c) of 11.7 kOe and maximum energy product $(BH)_{max}$ of 9 MGOe. The bulk magnet could be fabricated with high M_r/M_s ratio of 0.91 and a $(BH)_{max}$ of 5.8 MGOe at room temperature. The H_c of the bulk magnet increases linearly from 6.5 kOe at 300K to 28.3 kOe at 530K with a $(BH)_{max}$ of 3.6 MGOe at 530K.

P.-K. Nguyen, Jin and Berkowitz (2013) reported the study of bulk polycrystalline of LTP-MnBi ($\text{Mn}_{1.08}\text{Bi}$) prepared by induction melting and subsequent annealing at 300 °C for 96 hr. The sample was measured by VSM. The M-H loop shows a saturation magnetization (M_s) of 73.5 emu/g in 70 kOe and coercivity (H_c) of 50 Oe at 300 °C.

V. V. Nguyen et al. (2014) reported the study the effect of milling on the properties of MnBi magnet. Low-temperature (– 120 °C) and low-energy ball-milling (LTLEBM) was employed to produce powders of MnBi from the ingots of MnBi (~ 97 wt%) prepared by arc-melting. After milling, the powders were sintered in vacuum at 300 °C. The milled powders were aligned in an 18 kOe field and fast-warm compacted by a pressure of 100–250 MPa at 300 °C for 5–20 min. The magnetic properties were measured by physical property measurement system (PPMS) with a maximal measuring field of 90 kOe at different temperatures. After LTLEBM, the coercivity of the MnBi powder was found to increase from 1 kOe to 12 kOe. The bulk magnets have a maximum energy product of 7.8 MGOe and coercivity of 6.5 kOe at room temperature. When the temperature is increased to 475K, the coercivity increases to 23 kOe.

J. Cui et al. (2014) reported the study of MnBi permanent magnets (>90%) made from MnBi powder prepared arc melting followed by grinding (mortar and pestle), annealing (at 563 K for 24 hr) and ball milling. The powders were aligned using DC or pulsed magnetic field and the obtained green compact was sintered at 530K for 30 min. The produced powder exhibits saturation magnetization (M_s) of 74.6 emu g⁻¹ at room temperature with 9 T applied field. After alignment, the maximum energy product of the powder reached 11.9 MGOe, and that of the sintered bulk magnet reached 7.8 MGOe at room temperature. A comprehensive study of thermal stability was carried out. MnBi powder was found to be stable up to 473K in air.

Poudyal et al. (2016) reported the study of MnBi magnet made from MnBi prepared by arc-melting and subsequent sintering. High LTP-MnBi content up to 98 wt% was obtained by arc-melting followed by grinding and sintering around 573K. This work used low-temperature ball-milling to produce MnBi powder before a warm compaction technique to produce a magnet. Before low-temperature ball-milling, the starting MnBi powders have the size ranging from 20 to 75 μm and coercivity of about 2–3 kOe. After milling down to 1–7 μm particle size, the coercivity was increased

above 12 kOe. The as-milled powders were aligned with a magnetic field of 2 T then subjected to a fast-warm compaction (573K for 10–60 min) with average size about 50 nm. Using PPMS with a maximal measuring field of 9 Tesla at different temperatures (300 to 400K), the magnet was found to exhibit a maximum energy product of 8.4 MGOe and a coercivity of 6.2 kOe at room temperature. Magnetic characterization at elevated temperatures showed an increased coercivity to 16.2 kOe while energy product value decreased to 6.8 MGOe at 400K.

B. Li et al. (2018) prepared MnBi powder with composition to obtain $Mn_{50}Bi_{50}$ by arc-melting, subsequent annealing and followed by ball milling. The ingot was annealed at 573K for 10, 15, 20, 25 hr. The ingot heat treated at 573K for 25 hr was crushed and sieved. Obtaining initial particles with average size of $\sim 75 \mu m$ and then LEBM was conducted for 2,3,5 hr using a home-made rotary milling machine with a rotation speed of 150 rpm. An average particle size of approximately $2 \mu m$ could be obtained after ball-milling of 2 hr, small size of $1 \mu m$ was obtained when extending ball milling time to 5 hr. The as-milled powders were mixed with epoxy resin and aligned in a mold under a magnetic field of 1.8 T at room temperature to obtain anisotropic powder. The content of LTP MnBi increases with annealing time and the coercivity increases with milling time. The magnetically aligned 2-hr-ball-milled MnBi exhibits optimal magnetic performance with M_s of 55.1 emu/g, H_c of 14.1 kOe, and a high ratio M_r/M_s value of 96.2%.

Huang et al. (2019) prepared $Mn_{60}Bi_{40}$ alloys by arc melting and subsequent heat treatment under Ar atmosphere. The temperature and annealing time were in the range of 535-613K and 6-12 hr, respectively. High-energy ball milling was conducted for 0.5-8 hr in a hardened stainless-steel with a rotation speed of 200 rpm. VSM measurement with aligned- field of 9T show coercivity of 7.11 kOe at 300K and 21.97 kOe at 500K.

2.3.3 Melt spinning or rapid solidification

Melt spinning or rapid solidification is a technique to form thin ribbons of metal or alloys. A melt spinning process involves casting molten metal by jetting it onto a rotating wheel or drum, which is cooled internally, usually by water or liquid nitrogen.

The first demonstration of high performance large sized MnBi permanent magnets was studied by Kim et al. (2017). MnBi ribbons were synthesized by melt-spinning of arc-melt MnBi molten. MnBi ribbons were cold-pressed and annealed at 300 °C for 20 hr in vacuum. The pressed sample was ground by ball-milling and jet-milling. Magnetic separation was employed to obtain pure magnetic phase of 98 wt%. The MnBi powder was compressed with aligned magnetic field of 2 T and then sintered at 280 °C for 10-20 min under vacuum. The highest maximum energy product $(BH)_{max}$ of 7.3 MGOe was obtained.

J. Cao et al. (2018) synthesized MnBi powders from MnBi ribbons prepared by arc-melt-spinning on a surface of a rotating copper wheel in argon atmosphere. The ribbons were annealed at 673K for 30 min in vacuum and ball milling for different durations (0.5-28 hr). MnBi powders were then treated by spark plasma sintering (SPS). The magnetic properties were measured by VSM with maximum aligned field of 9 T. The optimum conditions result in MnBi powders with $M_r = 26.0$ emu/g, $H_c = 7.11$ kOe and $(BH)_{max} = 1.53$ MGOe at room temperature, and a maximum value $H_c = 25.37$ kOe at 550K.

X. Li et al. (2019) synthesized $Mn_{55}Bi_{45}$ ribbons by melt spinning of the MnBi molten produced by induction melting in argon gas. Annealing ribbons at 573K for 30 min in vacuum and milling by LEBM and SALEBM (Surfactant assisted low-energy ball milling) were carried out after melt-spinning. The milled $Mn_{55}Bi_{45}$ powders were mixed with epoxy resin and aligned in a magnetic field of 1.8 T. Using PPMS to measure the magnetic properties with a maximum aligned field up to 30 kOe, it was found that $Mn_{55}Bi_{45}$ powders obtained by SALEBM have better particle size uniformity and show higher decomposition of LTP MnBi. The coercivity of 17.2 kOe and the saturation magnetization (M_s) of 16 emu/g were obtained when $Mn_{55}Bi_{45}$ powders milled about 10 hr by SALEBM. The maximum of 18.2 kOe at room temperature, and 23.5 kOe at 380 K were observed after 14 hr of LEBM.

J. Cao et al. (2019) fabricated resin-bonded MnBi magnets from melt-spun MnBi. First, Mn_xBi_{100-x} ($x = 45, 55, 60$) ribbons were prepared by melt-spinning of arc-melting molten in argon atmosphere. The ribbons were ejected to the surface of a rotating copper wheel and heat treatment at 673K for 30 min in vacuum. MnBi powders were

obtained by using ball milling (SABM) for 0.5–28 hr at room temperature. Anisotropic bonded MnBi magnets were fabricated by compression molding of MnBi powder/epoxy resin under a magnetic field of 1.8 T. Using VSM with a maximum aligned field of 9 T, the optimum anisotropic bonded magnet was found displaying the maximum energy product $(BH)_{max}$ of 9.06 MGOe at room temperature, and 7.05 MGOe at 380 K, and coercivity of 15 kOe at room temperature.

2.3.4 Sintering

Sintering is a processing technique used to produce materials by applying thermal energy. Adams, Hubbard and Syeles (1952) was the first to report MnBi magnet prepared by hot pressing of sintered MnBi. Sintering was taken place at 700 °C. Subsequent grinding with high-speed harmer mill was carried out in He atmosphere. Magnetic separation was carried out to obtain pure magnetic MnBi material. The powders were under compaction at 300 °C and a magnetic field of 2 T. Some MnBi compacts showed a maximum energy product $(BH)_{max}$ of 4.3 MGOe, a coercivity of 3.4 kOe and a residual flux density (B_r) of 4.3 kG.

Kishimoto and Wakai (1977) synthesized MnBi particles by ball milling of sintered MnBi. Sintering was carried out at 265 °C for 10 days. The sintered MnBi powders was obtained by ball milling. At 300K, the coercivity was found to be only 550 Oe. After milling for 24 hr, the coercivity was increased to 16 kOe. At 85K, the coercivity was about 80-400 Oe for ball milling time as 1, 2, 8, and 24 hr, very low comparing to that obtained at 300K.

J. B. Yang et al. (2002) fabricated MnBi resin-bonded magnets from magnetic-purified sintered MnBi. MnBi resin bonded magnets exhibited coercivity of 14 kOe and energy produce of 7.7 MGOe (61 kJ/m³) at 300K, and coercivity of 20 kOe and energy produce of 4.6 MGOe (61 kJ/m³) at 400K.

Ko, Choi, Yoon and Kwon (2007) fabricated Mn_{1+x}Bi (0.0≤x≤0.5) magnets from mechanically MnBi (MA) alloyed powers using spark plasma-sintering process. Total mass of 20 g was weighted for Mn_{1+x}Bi and milled in a planetary ball mill under Ar atmosphere for MA. Milling was done in two steps. Rather hard small balls of mixture of Mn and Bi powder were obtained by milling for 120 min at 64 G.

These balls were heat-treated for 10 hr at 250 °C (first heating). Then the ball became soft to easily ground into coarse powder in a mortar. The second-step milling was done on these coarse powders for 10 min at 2 G to fine powders with size smaller than 0.5 μm . The powders were contained in a cylindrical graphite mold and then sintered at 230 °C and 20 MPa by vacuum spark plasma-sintering process. The obtained MnBi tablets were sealed in glass tube and annealed at 250 °C (second heating) for 3, 7, 14, and 28 days. Mechanically alloyed powders (2nd-MA) yielded powder with sizes smaller than 0.5 μm . VSM measurements were carried out with a maximum aligning field of 15 kOe, it was found that optimum values of $M_r = 15 \text{ emu/g}$ and $H_c = 10.0 \text{ kOe}$ and $(BH)_{max} = 5.34 \text{ MGOe}$ at $x = 0.08$ powders, 250 °C. In spark plasma-sintering magnet, M_r increased with x while H_c did not change around 7.5 kOe (varied day, at 250 °C).

Schematic diagram showing methods for synthesizing LTP-MnBi is displayed in Figure 2.12 The preparations techniques include arc-melting, induction heating, melt spinning and sintering.

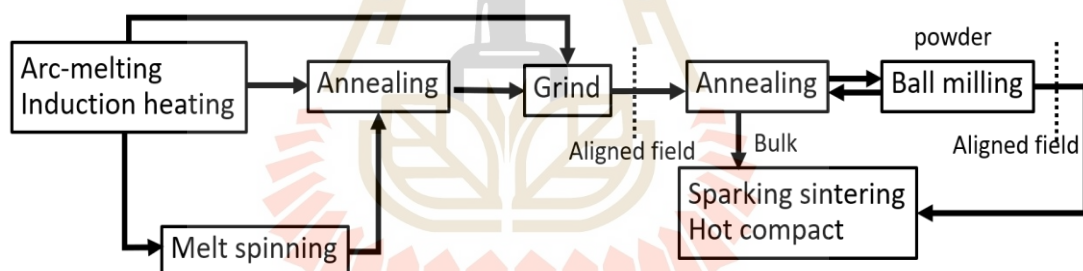


Figure 2.12 Summary of LTP- MnBi preparation with various techniques.

Types of sintering: Sintering may be divided into four main types i.e., solid state sintering, liquid phase sintering, transient liquid phase and viscous flow sintering. Viscous flow sintering occurs when the fraction of liquid is high. Transient liquid phase consists of liquid phase sintering and solid-state sintering. In this sintering a liquid phase disappears as sintering progresses, only solid phase is appeared, as shown in Figure 2.13.

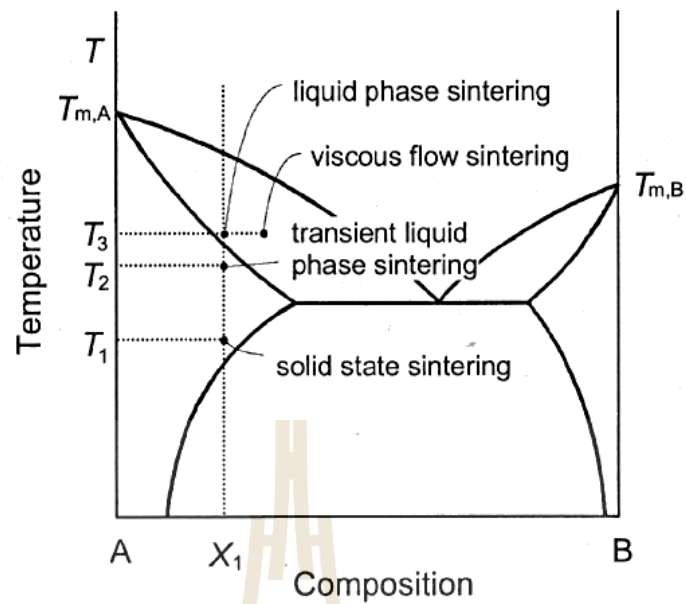


Figure 2.13 Types of sintering (Kang, 2005).

Sintering variation: The sintering variation can be divided into two types: material variables and process variables as summarized in Table 2.5. Material variables effect the densification and grain growth, and process variables influence sinter-ability and microstructure.

Table 2.5 Variables affecting sinter-ability and microstructure (Kang, 2005).

Variables related to raw materials (Material variables)	Powder: shape, size, size distribution, agglomeration, mixedness, etc. Chemistry: composition, impurity, non-stoichiometry, homogeneity, etc.
Variables related to sintering condition (process variables)	Temperature, time, pressure, atmosphere heating and cooling rate, etc.

Stage of sintering: The stage of sintering can be divided into 3 stages in dry sintering i.e., neck formation, shrinkage, and grain growth.

Mechanism of sintering: In general sintering process, temperature effects atomic motion; the atoms can be moved when getting high enough temperature. The mechanisms of atom motion exhibit different patterns such as, evaporation, condensation, volume diffuse, grain boundary, surface diffusion and plastic flow, as summarized in Figure 2.14.

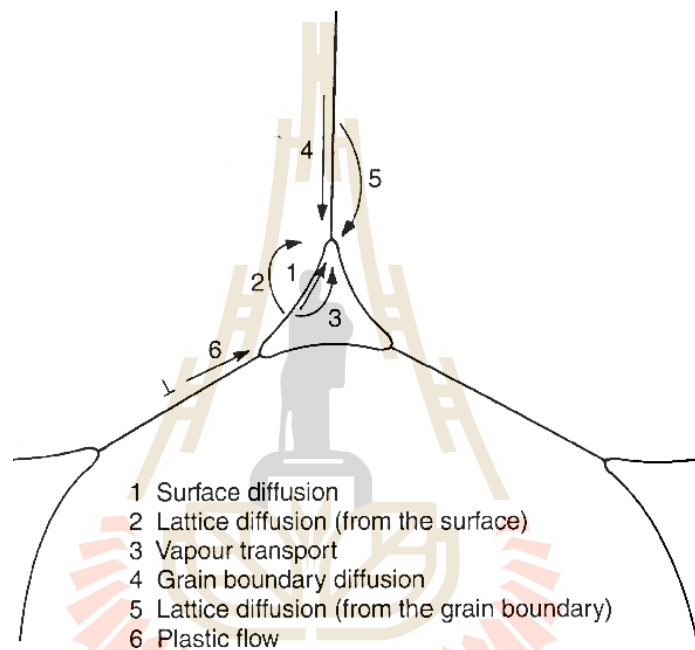


Figure 2.14 Various sintering mechanisms (Kang, 2005).

2.4 Diffusion

Diffusion occurs to reduce a decreasing Gibbs free energy and materials transport by atomic motion. Normally, diffusion begins from a high concentration to low concentration region. The diffusion coefficient is defined by Fick's law.

In an Isotropic medium, the physical and chemical properties are independent of direction. For anisotropic medium, they are dependent on direction. Example of, the isotropic cases are diffusions in gases, in liquids, in glassy solids, polycrystalline without textures. Two well-known Fick's laws are generally used for explaining diffusion in solids i.e., the Fick's first law and Fick's second law.

Fick's first law: This law expresses the relation between the flux of particles to a concentration gradient in one dimension (x-direction) for an isotropic medium while in a steady state i.e., the concentration does not depend on time, as presented in Figure 2.15.

$$J_x = -D \frac{\partial C}{\partial x} \quad \text{eq.1}$$

where J_x is the flux of particle or diffusion flux ($\text{mole m}^{-2}\text{s}^{-1}$), D is diffusion coefficient or diffusivity (m^2s^{-1}), and $\frac{\partial C}{\partial x}$ is a concentration gradient (mole m^{-4}).

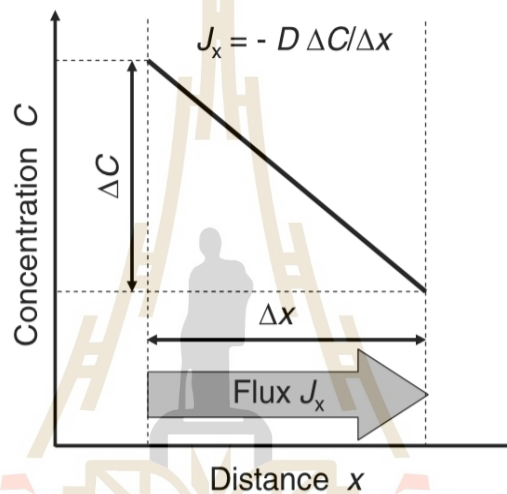


Figure 2.15 Illustration of the Fick's first law (Mehrer, 2007).

Fick's second law: It is a continuous solution from the Fick's first law with time-dependent concentration, which is referred as a non-steady state. The solution corresponds with continuity solution (eq.1).

$$-\nabla \cdot J = \frac{\partial C}{\partial t} \quad \text{eq. 2}$$

Combining the Fick's first law and the continuity solution,

$$\frac{\partial C}{\partial t} = \nabla \cdot (D \nabla C) \quad \text{eq. 3}$$

The diffusion equation considered only one dimension in the steady state, which is frequently used in thin film geometry. The Fick's second law can be rewrite as

$$\frac{\partial C}{\partial t} = -\frac{\partial J}{\partial x} \quad \text{eq. 4}$$

and

$$\frac{\partial C}{\partial t} = D \frac{\partial^2 C}{\partial x^2} \quad \text{eq. 5}$$

This second order differential solution is non-linear due to D is independent of x but depend on concentration. It may be solved for the value of concentration at desired position and time, and the solution is called a Gaussian solution, as given in eq., where $2\sqrt{Dt}$ is diffusion length.

$$C(x, t) = \frac{M}{\sqrt{\pi Dt}} \exp\left(\frac{-x^2}{4Dt}\right) \quad \text{eq. 6}$$

This solution is a relative diffusion coefficient with its solution given in eq.7.

$$D = D_0 \exp(-Q/RT) \quad \text{eq. 7}$$

where R is the universal gas constant (J/K.mole), D_0 is the diffusion coefficient of material constant (m^2s^{-1}), Q is the activation entropy (kJ/mole). The values of D_0 and Q can be obtained from experiments.

Diffusion coefficient in MnBi magnetic materials: Van Nguyen and Nguyen (2017) predicted diffusion coefficient in MnBi arc-melting after annealing at 300 °C. They described by one-dimensional time-dependent diffusion equation. The diffusion coefficient (D) was reported with the value of $\sim 10^{-12} \text{ cm}^2/\text{s}$, as shown in Figure 2.16.

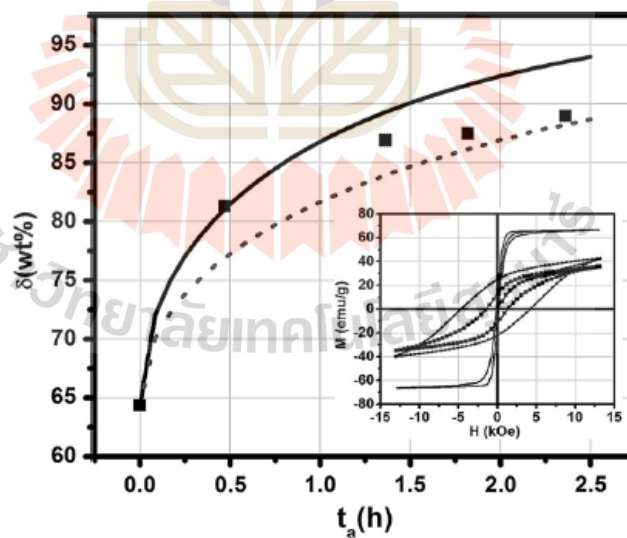


Figure 2.16 LTP content $\delta(t_a)$ of MnBi as a function of annealing time. The diffusion coefficients $D = 1 \times 10^{-12}$ (dotted) and $2 \times 10^{-12} \text{ cm}^2/\text{s}$ (solid). The square is the calculated results by endo peaks of the cycled DSC trace. The insert shows the VSM loops of MnBi powder ground from arc-melting (square), the 300 °C/3 hr (circle) and 300 °C/30 hr (line) (Van Nguyen and Nguyen, 2017).

2.5 Stability of magnetic materials

In previous reports, several authors tried to control the parameters in experiments for studying the changes in structural and magnetic properties as a function of time. The main factors that were found to affect the magnetic properties as a function time are humidity (Jacobson and Kim, 1987), oxidation (Janotová, Švec, Matko, Janičkovič and Sr., 2018; Ly et al., 2014; Villanueva et al., 2019), degradation (Ly et al., 2014; Sun, Xu, Liang, Sun and Zheng, 2016), and temperature (S. Cao et al., 2011; Y.-C. Chen et al., 2015; J. Cui et al., 2014; Zhang et al., 2014).

M. Y. Sun et al. (2016) prepared LTP-MnBi thin films by magnetron sputtering system at room temperature. They investigated stability of both the structure and perpendicular magnetization of LTP-MnBi thin films that were exposed to ambient atmosphere. They found M_s reduction of 35% and H_c enlargement of 23% after exposing to air for 14 days, as shown in Figure 2.17. These behaviours of M_s and H_c were explained by the oxidation of Mn and the weakened inter-grain exchanges at grain boundaries, respectively.

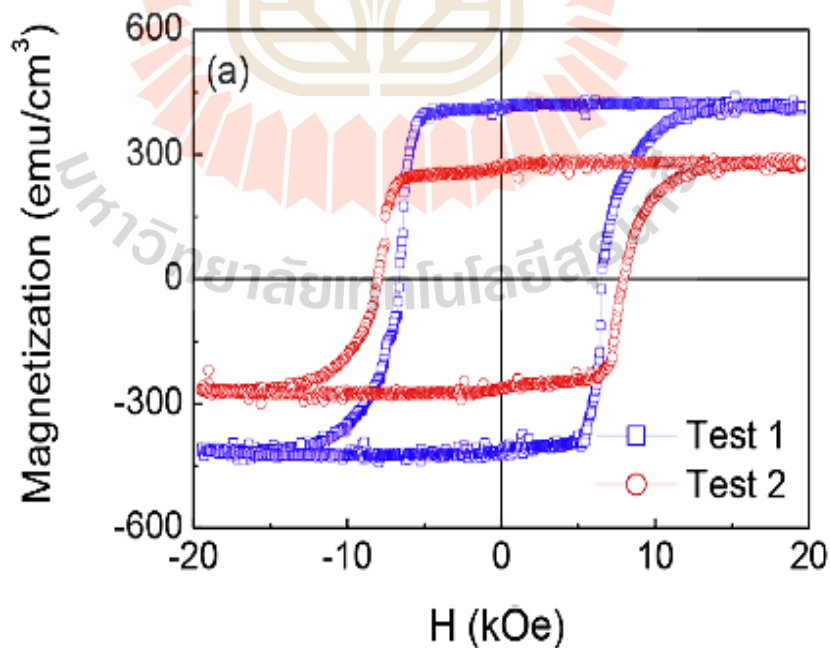


Figure 2.17 Magnetic hysteresis loops of LTP-MnBi thin film as fabricated (Test 1) and after 14-days exposure to air (Test 2) (M. Y. Sun et al., 2016).

Villanueva et al. (2019) also studied LTP-MnBi thin film degradation of magnetic properties prepared by DC-magnetron sputtering. They found M_s were decreased by 54% after 6 days and disappeared after 4 months, as shown in Figure 2.18. These results could be explained by the changes of the crystal structure.

Ly et al. (2014) studied the effect of room-temperature aging under ambient atmosphere on magnetization for LTP-MnBi ingot prepared by crystallization of a melt-spun precursor. They found the decrease of magnetization when exposed to the ambient atmosphere for longer than 7 days. This was caused by the oxidation of Mn, leading to a MnBi phase decomposition.

Janotová et al. (2018) observed the degradation of the Mn-Bi base ribbon fake over a period of one year. The sample was prepared by the rapid quenching technique under Ar atmosphere. The magnetic phase decreased after exposing to ambient atmosphere, this assigned to oxidation, resulting in the reduction of the content of MnBi with aging time.

Yoshida, Shima, Takahashi and Fujimori (1999) found the surface Mn-free MnBi ingot prepared by arc-melting technique exhibited almost no oxidation after exposing to ambient atmosphere for more than 1 year. This was interesting as the sample showed no sign of degradation. However, there was no other reports supporting this finding.

J. Cui et al. (2014) observed thermal stability of MnBi magnetic materials, which were prepared by arc-melting. M-H curves were measured for different particle sizes after heat treatment at 623K (350 °C) in air and Ar-2.75 % H₂. The M_s decreased with the particle sizes, as shown in Table 2.6.

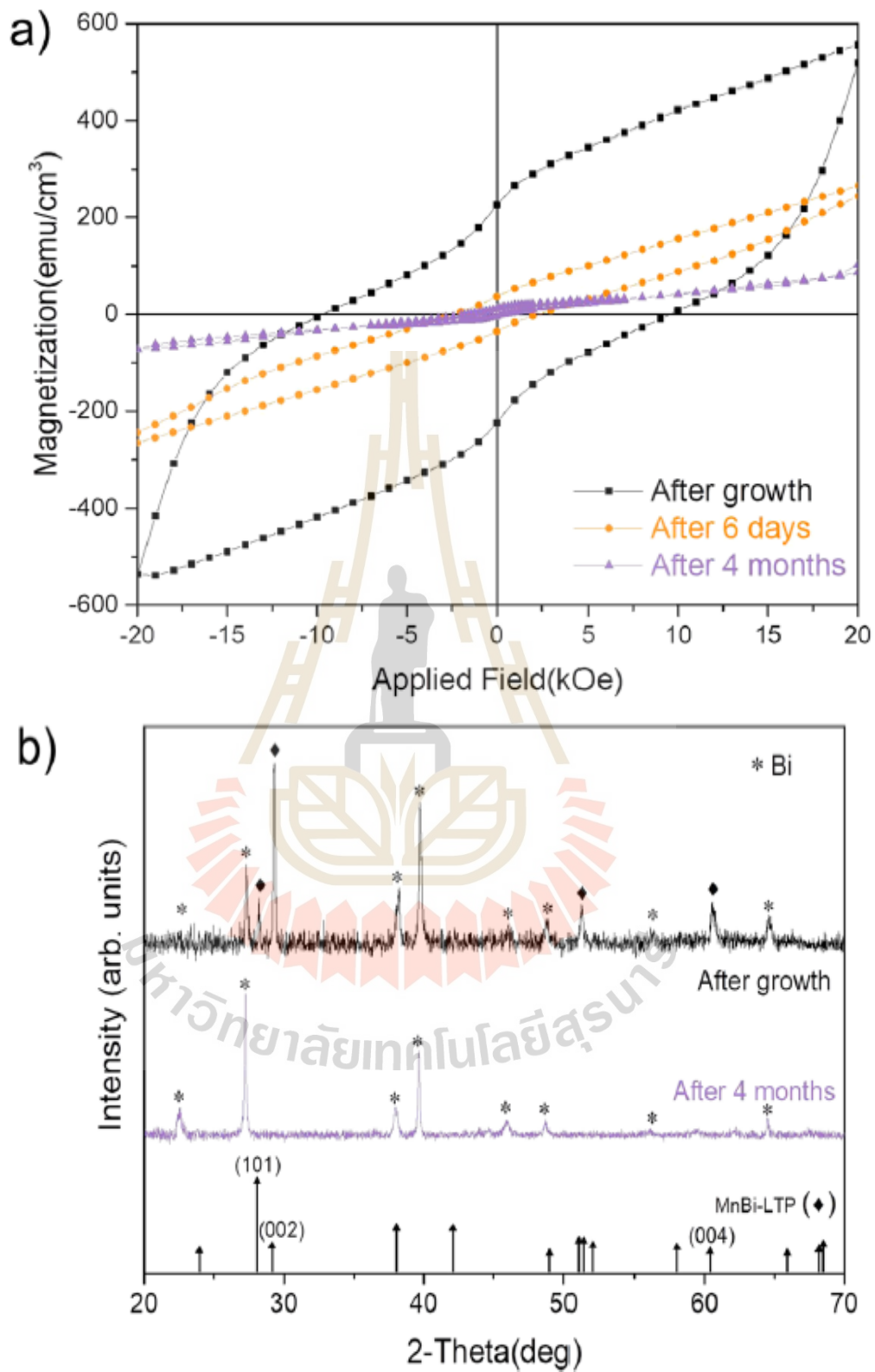


Figure 2.18 Magnetic hysteresis loop of LTP-MnBi thin film before and after degradation (a) and XRD diffraction after growth and 4 months (b) (Villanueva et al., 2019)

Table 2.6 The saturated magnetization (emu/g at 1 T) after heat treatments for the MnBi samples with different particle sizes. It is noted that, before the heat treatment, the saturation magnetization is about 63 emu/g (J. Cui et al., 2014).

	Air/350 °C	H ₂ -Ar/350 °C
60 mesh (<250 μm)	50.8	62.3
200 mesh (<74 μm)	22.8	61.2
400 mesh (<37 μm)	13.7	59.7



CHAPTER III

EXPERIMENTAL METHOD

This chapter describes the sample preparation and characterization techniques employed in this thesis work. LTP-MnBi powder was synthesized by sintering in vacuum. Different material characterization techniques were used to investigate the structural and magnetic properties of LTP-MnBi. The mechanisms for the formation and degradation/decomposition of LTP-MnBi were also studied. The principles and instrument set up of those analysis techniques are also given.

3.1 LTP-MnBi synthesis

3.1.1 Ball milling and sieving

The starting materials for synthesizing LTP-MnBi were Mn powder (> 99% purity, 40 mesh, particle size < 400 μm) and Bi powder (> 99.5% purity, 100 mesh, particle size < 149 μm) supplied by Acros Organics. To study the formation mechanism of LTP-MnBi, large particle sizes of Mn powders were used for an ease of sample preparation, especially cross-sectional SEM sample preparation. For the investigations of the structural and magnetic properties, Mn powder with particle size of less than 20 μm was used. This small Mn particle powder was obtained by ball-milling by using a planetary Micro mill (PULVERISETTE 7 classic line, Fritsch, Germany) at the rotation speed of 300 rpm for 3hr and then sieved with a 700-mesh screen to obtain the Mn powder with particle size of less than 20 μm . The ground Mn powder and Bi powder were mixed with 1:1 atomic ratio, or the weight ratio of 1.373: 5.224. To assure the homogeneity of the mixture before loading into the quartz tube of the effusion cell, the mixture was further mixed by using a Mini Mill Grinder (PULVERISETTE 23, Fritsch, Germany) with shaking frequency of 40 Hz for 15 mins. Figure 3.1 presents the procedures for mixing Mn and Bi powder before introducing into the quartz tube of the effusion cell.

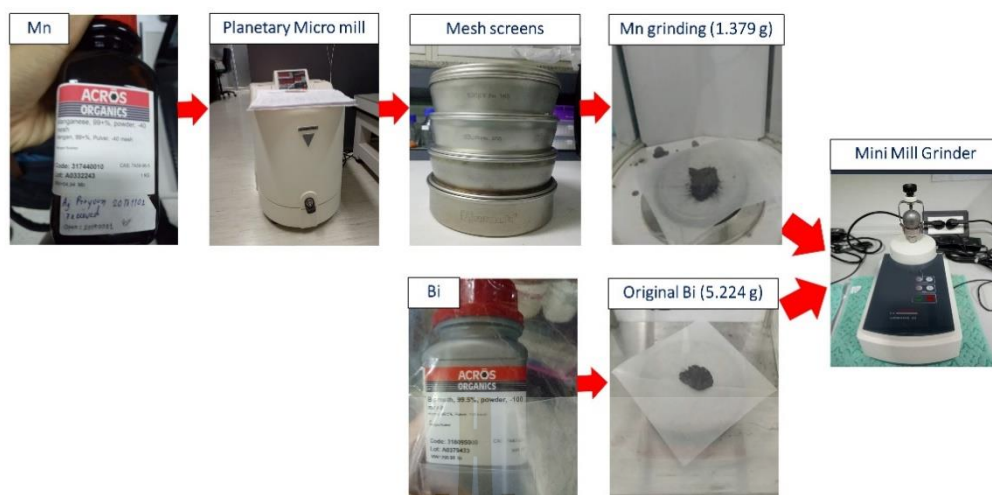


Figure 3.1 The graphical representation showing the procedures for preparing the mixture of Mn and Bi powders before sintering.

3.1.2 Sintering in vacuum

In this work, sintering of the mixture of Mn and Bi powder was performed in vacuum at temperature between 275 °C to 375 °C. The schematic diagram and the photo of an in-house made sintering system is shown in Figure 3.2 (a) and (b). The system consists of a small vacuum chamber evacuated by a 500 l/s turbomolecular pump backed by a scroll pump. The base pressure of this system is below 1×10^{-8} mbar, after pumping for 2 days without baking. The essential component of this system is a low temperature effusion cell (Dr. Eberl MBE-Komponenten GmbH, Germany). This cell is mounted on a 3-way vacuum fitting connected to the side port of the main chamber. This set up prevents accidents causing any materials to be fallen into the turbomolecular pump, which would cause expensive damage to the system. The effusion cell is water-cooled to maintain the out-gassing rate of materials of the effusion cell to be able for the pump to produce good vacuum. A 2048 EUROTHERM temperature controller was used to control the temperature of the effusion cell to be within ± 0.1 °C accuracy. In this work, sintering is rather low, below 375 °C, quartz tubes with capacity of 10 cc were used as a crucible or container of the sintered materials.

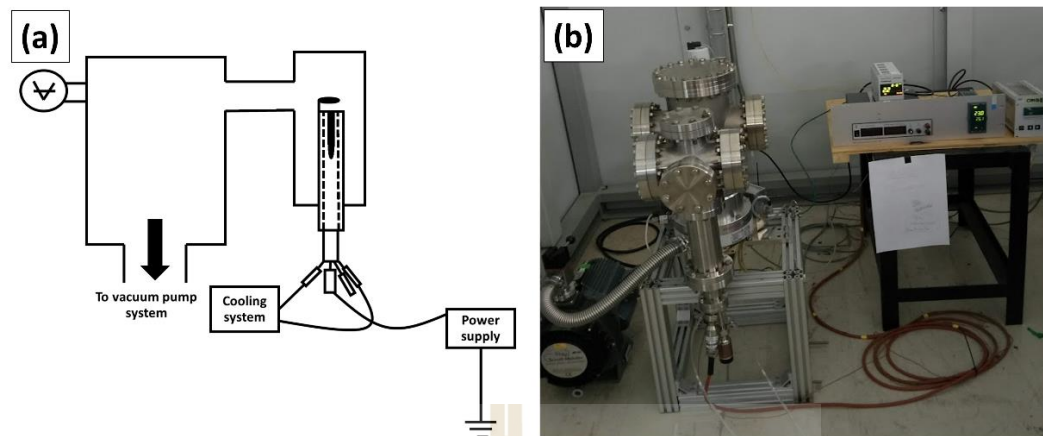


Figure 3.2 (a) A schematic diagram and (b) photo of an in-house made sintering system

To prevent possible damages to the equipment, careful operational procedures of this vacuum sintering system were taken seriously. To load materials for sintering, it is necessary to brake vacuum and remove the effusion cell out from the system. After insertion of the quartz tube containing the mixed materials into the effusion cell, the cell is again mounted to the system. Rough pumping was achieved by a scroll pump until the pressure reaches vacuum pressure level below 5×10^{-2} mbar, the turbomolecular pump was then turned on. The pressure will reach 2×10^{-8} mbar after 1 or 2 days pumping, depending on the amount of the loaded materials. The most important precaution is that the effusion cell MUST be operated below 5×10^{-7} mbar. This limitation is to prevent the lifetime shortening of the filament of the effusion cell.

3.1.3 Preparation of cross-sectional sample for SEM/EDS

One of the challenges in this work was to prepare cross-sectional samples of LTP-MnBi powder particles with particle size of tenth to hundredth micron in diameter. The larger diameter, the simpler would be expected. Advanced sample cutting/milling machines made this work possible. The preparation of the cross-sectional MnBi powder particles was taken place at the Thailand Science Park in Pathumthani.

The sample preparation begins with epoxy cast resin process, i.e., the sintered MnBi powder with selected size range was embedded into a mole and covered with epoxy resin on top of the sample. The MnBi embedded in resin was sandwiched between two microscope cover glasses with dimensions of $2 \times 7 \text{ mm}^2$, as shown in Figure 3.3. The samples were mechanically polished using the Target Surfacing System (EM TMP, Leica, Germany), shown in Figure 3.4, to obtain a surface roughness of less than $2 \text{ }\mu\text{m}$. It is noted that the target surfacing system is an equipment used for preparations a small sample with high precision for microstructure investigations. This target surfacing instrument can be equipped with diamond and tungsten carbide millers, diamond disc cutter, diamond core drill, and lapping foil inserts. Thus, this device can mill, saw, drill, grind, and polish the samples.

After processing with the mechanical target-surfacing system, the surface of the cross-sectional samples is milled by the Argon ion beam slope cutting device (EM TIC 3X, Leica, Germany), shown in Figure 3.5, at 5 kV for 7 hrs prior to the EDS line scan measurements. Milling by bombardments of Ar ions generates no mechanical stress to the sample that might induce damage to the sample. The mask is used to allow the ion beam to hit the area of the sample where the materials needed to be removed.

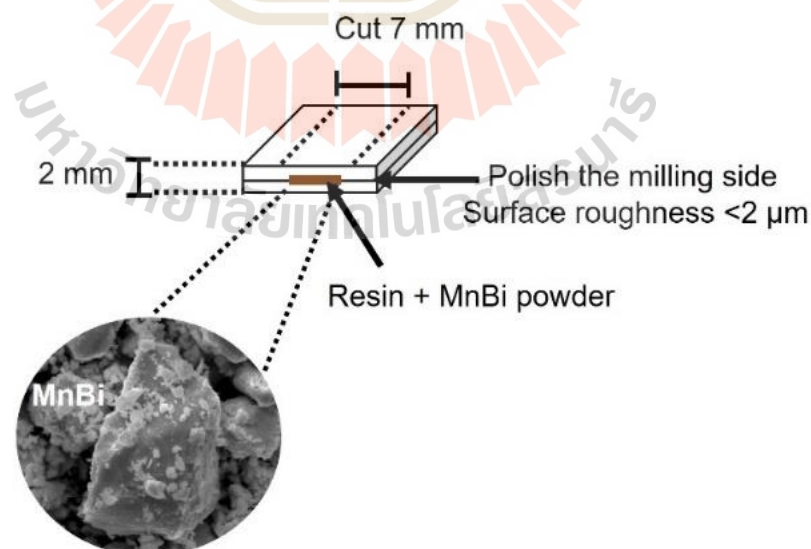


Figure 3.3 Graphical representation for the resin embedded with MnBi and sandwiched between microscope cover glasses.



Figure 3.4 Target surfacing system (EM TMP, Leica, Germany).



Figure 3.5 Argon ion beam slope cutting device (EM TIC 3X, Leica, Germany) at the Thailand Science Park.

3.2 Materials characterizations

3.2.1 X-ray diffraction (XRD)

X-ray diffraction (XRD) is a characterization technique widely used for phase identification of materials. XRD provides information related to crystal structure and

crystallite size. The technique relies on the measurement of intensity of X-ray reflected from crystal, which related to Bragg's law. This relation is formulated by W.L. Bragg in 1913, as illustrated in Figure 3.6. The relation of an incident X-ray beam with wavelength of λ and diffracted beam is given by

$$n\lambda = 2d'\sin\theta$$

where λ is wavelength of X-ray, n is order of diffraction, d' is the spacing of the atomic planes, θ is the incident angle with respect to the diffracting planes.

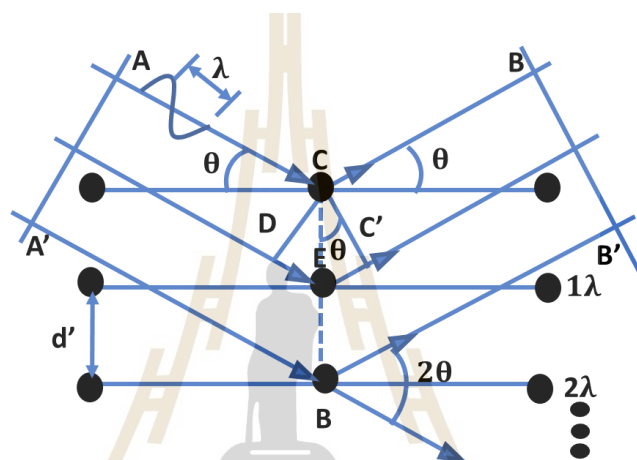


Figure 3.6 Schematic diagram showing X-ray diffraction from atomic planes.

Figure 3.7(a) and (b) show two X-ray diffractometers of the same manufacturer used in this research: XRD (Bruker D2 phaser) and XRD (Bruker D8). They are located at the Center for Science and Technological Equipment of Suranaree University of Technology. X-ray generator obtained using $\text{Cu K}\alpha$ ($\lambda = 0.154 \text{ nm}$). The angle between transmitted beam and reflected beam (2θ) is detected from 20 to 60 degrees with step time and step size of 0.5 s and 0.02 degrees, respectively. Moreover, a Rigaku Smart lab diffractometer (Rigaku) was analyzed crystal structure with a $\text{CuK}\alpha$ X-ray source ($\lambda = 0.154 \text{ nm}$), a voltage of 40 kV and a current of 30 mA. The scan range (2θ) is the similar value above and the photos of the equipment are shown in Figure 3.7(c). After that, qualitative phase analysis of MnBi powder can calculate by Rietveld refinement method with the FULLPROF program.

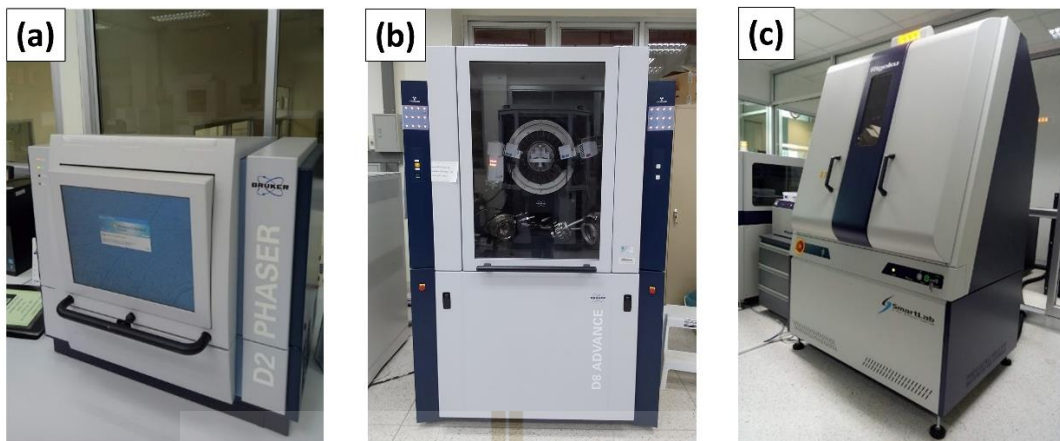


Figure 3.7 X-ray diffractometers used in this work: (a) Bruker D2 phaser, (b) Bruker D8 ADVANCE, and (c) Rigaku Smart lab diffractometers.

3.2.2 Scanning electron microscopy (SEM)

Figure 3.8 shows the working principle of SEM. Electrons are generated at the source and accelerated pass through the anode by an electric field. Vacuum pressure is necessary for the electron transport line. A condenser lens is employed to control the dimensions and, of course, divergence of the electron beam. The objective lens is employed to focus the electrons beam on the sample surface. A scanning coils are installed downstream of the objective lens to scan electron beam covering the area of interest on the specimen. When the electron beam impinges on the specimen surface, the electrons will travel into the material interacting with and deposit their kinetic energy to the atoms in the sample. The excited atoms in the materials may emit characteristic X-ray, luminescence, or Auger electrons. Of course, there are some electrons elastically back-scattered. Some back-scattered electrons and Auger electrons may lose part of their energy before coming out from the specimen surface. These electrons will be counted as secondary electrons. These phenomena are illustrated in Figure 3.9.

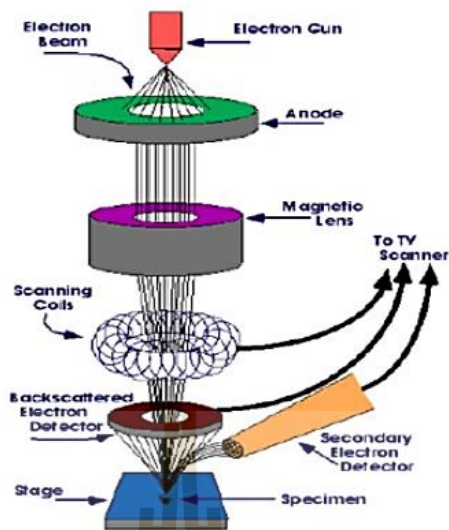


Figure 3.8 Principle of SEM operation. (Picture from <https://www.purdue.edu/epps/rem/laboratory/equipment%20safety/Research%20Equipment/sem.htm>)

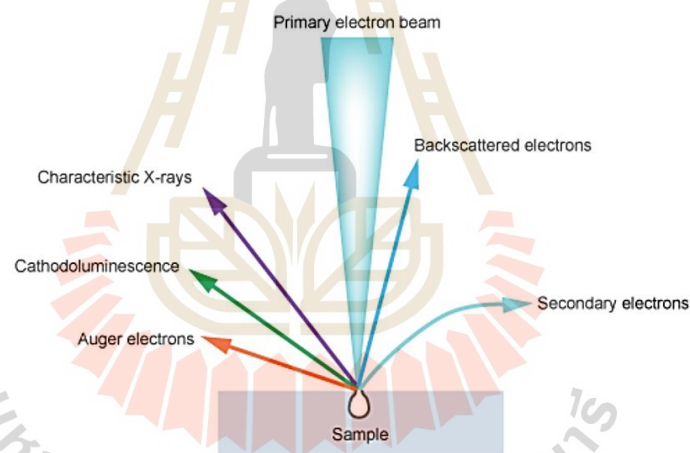


Figure 3.9 Interaction of an electron beam with the specimen. (Picture from <http://www.ammrf.org.au/myscope/common/images.php?module=sem#prettyPhoto>)

SEM and FE-SEM are used for studying microstructures of materials by using collecting secondary electrons and backscattered electrons. However, the names of SEM techniques are different from the electron source (electron gun); a thermal emission gun used for general SEM, while a field emission gun used for FE-SEM. General SEM uses a conventional thermionic source such as, Tungsten (W) and Lanthanum hexaboride (LaB_6) with a source size about 30-50 μm and 5-50 μm respectively.

In case of FE-SEM, a tungsten field emission gun (FEG) is used. Warm and cold field emission guns emit electrons with source size of 15 nm and 3 nm, respectively. Another advantage of using a field emission source is the small straggling of the kinetic energy of the emitted electrons. Thus, the performance of FE-SEM is, in general, better than that of SEM using a thermal emission gun. High spatial resolution with magnification up to 1,000,000 times could be obtained in FE-SEM, which is suitable for investigations of microstructures in a nano scale. Field emission sources also provide high brightness and long lifetime for the filament. The only disadvantage is that it is expensive source, requiring special vacuum requirement since the source must be in the ultrahigh vacuum range.

3.2.3 Energy dispersive spectroscopy (EDS)

EDS is an optional extended technique of SEM. EDS is the technique that collect elemental information of SEM images by detecting characteristic X-ray emitted from the excited atoms in the specimen. Thus, it is used for identifying elemental composition with spatial resolution. The phenomena are shown in Figure 3.10 illustrate inner-shell photoionization that emits characteristic X-rays.

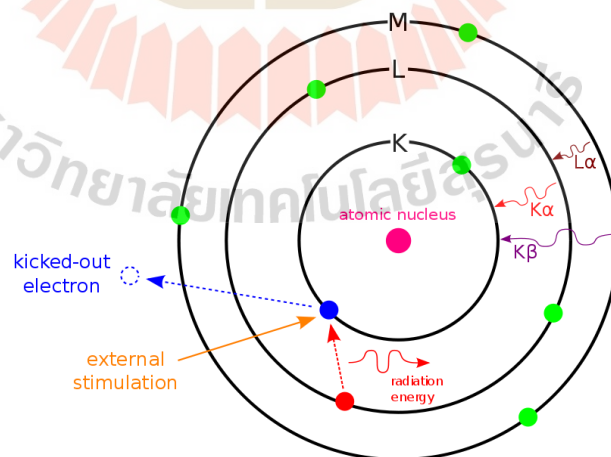


Figure 3.10 Principle of EDS. (Picture from https://en.wikipedia.org/wiki/Energy-dispersive_X-ray_spectroscopy)

SEM that can generate EDS spectra is equipped with a detector for measuring X-ray emission such as lithium-drifted silicon (Si(Li)) and a high purity Germanium (HPGe). Si(Li) and HPGe are suitable for detecting characteristic energy ranges of about 1-3 keV and 3-20 keV, respectively. The detector is located near to the specimen to provide large solid angle for the detection. The detector converts the energy of X-ray to a voltage pulse by preamplifier. The signals are sent to the multichannel analyzer. The EDS spectra are then shown on the computer display. Typical EDS spectra is shown in Figure 3.11.

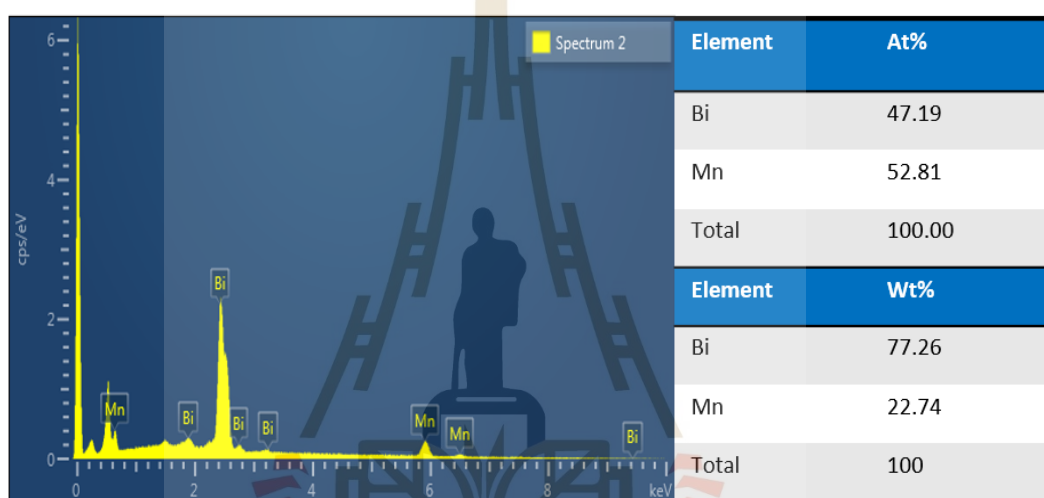


Figure 3.11 MnBi powder spectrum of the EDS analysis.

Finally, this work employed the JEOL JSM-6010LV SEM/EDS and JEOL JSM-7800F Prime FE-SEM/EDS systems for the investigations of the surface morphology and elemental composition at the Center for Science and Technological Equipment of Suranaree University of Technology and National Metal and Materials Technology Center (MTEC), as shown in Figure 3.12. Selecting SEM/EDS measured general morphology of secondary electron image (SE) and backscattered electron image (BSE), which used the parameters of accelerating voltage for electron (HV) and the working distance (WD) approximated 15-20 kV and 10-15 mm, respectively. For high resolution FE-SEM/EDS, the operating HV and WD were about 10-12 kV and 10 mm, respectively.

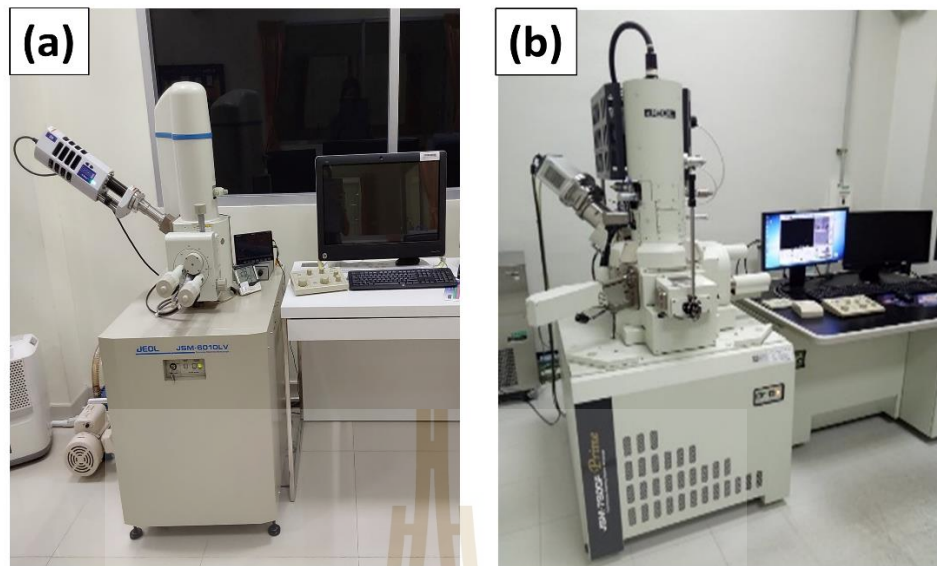


Figure 3.12 (a) SEM/EDS (JEOL JSM-6010LV) and (b) FE-SEM/EDS (JSM-7800F Prime).

3.2.4 Vibration Sample magnetometer (VSM)

VSM is used to measure the magnetic properties of magnetic material, which corresponds to the Faraday' law. The changing magnetic field will generate an electric field in a coil. The diagram of VSM is shown in Figure 3.13. The pickup coils are placed near the sample that vibrates in the Z axis with a fixed amplitude. The sample is placed in a homogeneous magnetic field and installed in the end of the sample holder and the top connected to the vibration system with a controlled frequency. After the sample oscillated or vibrated, the sample was magnetization. the magnetic dipole moment will produce magnetic field around the sample which is called magnetic stray field. The magnetic stray field can change as a function of time where the sample moves up and down, also detected by pickup coil or some sensor. This based on the Faraday's law of induction, the changing of magnetic stay field responds to the magnetic flux at pickup coil that was induced by the voltage. The voltage is proportional to magnetization. This induction voltage can be fed to an amplifier for signal amplification. Then, the amplified signal is converted by software to generate a Hysteresis loop.

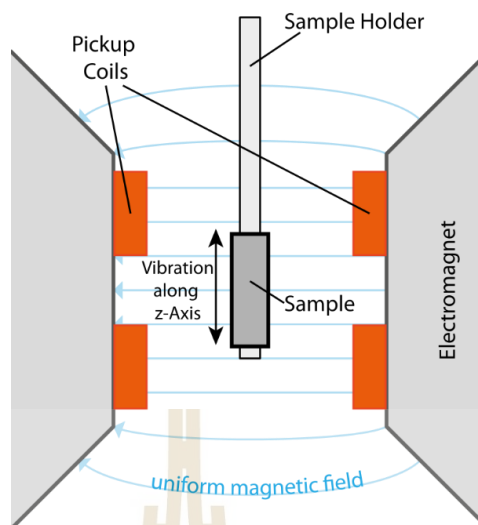


Figure 3.13 VSM schematic. (Picture from https://en.wikipedia.org/wiki/Vibrating_sample_magnetometer#/media/File:VSM_en.svg)

Figure 3.14 shows the VSM (Quantum Design Inc., VersaLab series) system that is installed at Khon Kaen University. M-H curves were achieved by applied magnetic field between -30 kOe to +30 kOe. This system is capable for cryogen-free cryocooler-based physical property measurements. The temperature range for the measurements can be varied from 50 to 400 K and the maximum magnetic field is 3 T. The amplitude is fixed for 1-3 mm (peak), frequency is 40 Hz and sensitivity is smaller than 1 μ emu magnetic moment change with 1 s data averaging.



Figure 3.14 VSM (Quantum Design Inc., VersaLab series) was used at Khon Kaen University.

Demagnetizing field correction: In fact, the raw data of the VSM loop are obtained with an open loop measurement set up by nature. Hence, it is essential to correct the effects of the demagnetizing field to obtain the internal field of the true intrinsic material parameters. The demagnetizing field depends on the sample geometry. Moreover, the internal magnetic field (H_{int}) and external magnetic field ($H_{applied}$) of materials had different values that can be explained as follows. The corrected internal magnetic field is $H_{int} = H_{applied} - 4\pi N_D M$, where N_D is the sample demagnetization factor (SI units) and M is the volume magnetization in emu/cm^3 . The obtained H_{int} equation was replaced in the magnetic induction $B = H_{int} + 4\pi M = H_{applied} + 4\pi M(1 - N_D)$. In this work, the VSM sample holder was placed transversely with the external field. The formula of N_D for the cylinder sample (transverse orientation with the field) is $N_D^{-1} = 2 + \frac{1}{\sqrt{2}} \frac{a}{b}$ (Prozorov and Kogan, 2018) where $2a$ and $2b$ are the diameter and length of the sample, respectively. For $2a = 2 \text{ mm}$ and $2b = 3 \text{ mm}$, N_D is 0.4. The unit of H_{int} , M , and B is gauss (G) unit; $1 \text{ G} \sim 1 \text{ Oe} = 4\pi \text{ emu/g}$.

3.2.5 X-ray absorption spectroscopy (XAS)

X-ray absorption spectroscopy (XAS) is used to study local atomic structure, which may be classified into 2 regions of the X-ray absorption spectra: X-ray absorption near edge structure (XANES) and extended X-ray absorption fine structure (EXAFS). This technique relied on X-ray absorption to observe the local structure, chemical state, oxidation state, and coordination number. Normally, the X-ray is an electromagnetic wave constituting the electric field and perpendicular magnetic field, it is also conserved as the smallest wave particle called a photon. Figure 3.15(a) shows the fundamental processes of X-ray absorption. When the specimen is incident by X-ray photon, the photon interacts with a core electron of atom (K, L, or M shell). The atom is excited by the transition of an electron from a ground state to an excited state i.e., the transition from a lower to a higher energy level. In the X-ray absorption process, the excitation photon energy must be higher or equal to the energy difference between the excited electron level (initial state) and the empty electron level (the final state). The minimum excitation energy required is called the threshold energy, referred as the edge energy in the absorption spectra. The relaxation of the excited

atom to the ground state by the transition of an electron dropping from the high electron energy level to the core hole. This decay process accommodates either with the release of photon energy, which is called fluorescent X-ray emissions as shown in Figure 3.15(b) or with Auger electron emission as shown in Figure 3.15(c)

XANES and EXAFE measurements of the sintered MnBi samples were carried out in a fluorescence mode at the beamline 5.2 of the Synchrotron Light Research Institute (SLRI), Thailand. In general, X-rays from a synchrotron light source is used in XAS measurements due to an extremely powerful source of X-rays with continuous spectrum. Synchrotron light is an electromagnetic wave generated by a charge particle moving with high speed as compared to speed of light in a curved motion. The graphical drawing of the synchrotron light source at SLRI is shown in Figure 3.16. Starting with the electron gun, which produces free electrons by thermal emission. The filament of the electron gun is held at negative potential. This gun is electrically isolated by a ceramic tube. The extraction part is held at ground potential. Thus, the electrons are then extracted by the electric field. The buncher first accelerates the electrons up to 6 MeV to be in a bunched pattern. The electrons are further accelerated by two linear microwave cavity acceleration tubes to increase the energy of the electrons to 40 MeV. Then, they are injected into the booster synchrotron for further acceleration. The electron travel in the booster ring and gain more energy every time when passing through the RF acceleration cavity. After traveling in the booster ring for about 0.6 seconds, the energy of the electrons reaches 1.2 GeV. The electrons are then kicked out from the booster ring and transported to the storage ring. The characteristics of the electron beam is defined mainly by the magnetic fields of the dipole (bending), quadrupole, and sextupole magnets of the storage ring. In the bending magnet, the electrons are bended and thus synchrotron light is emitted. There are also insertion devices such as undulator and wigglers installed in the straight section of the storage ring to produce synchrotron radiation with much high intensity and shorter wavelength, respectively. The synchrotron light is delivered by an optical system, namely optical beamline, to the experimental station. The characteristics of the light beam such as beam size, beam divergence and wavelength range are defined by the optical components of the beamline.

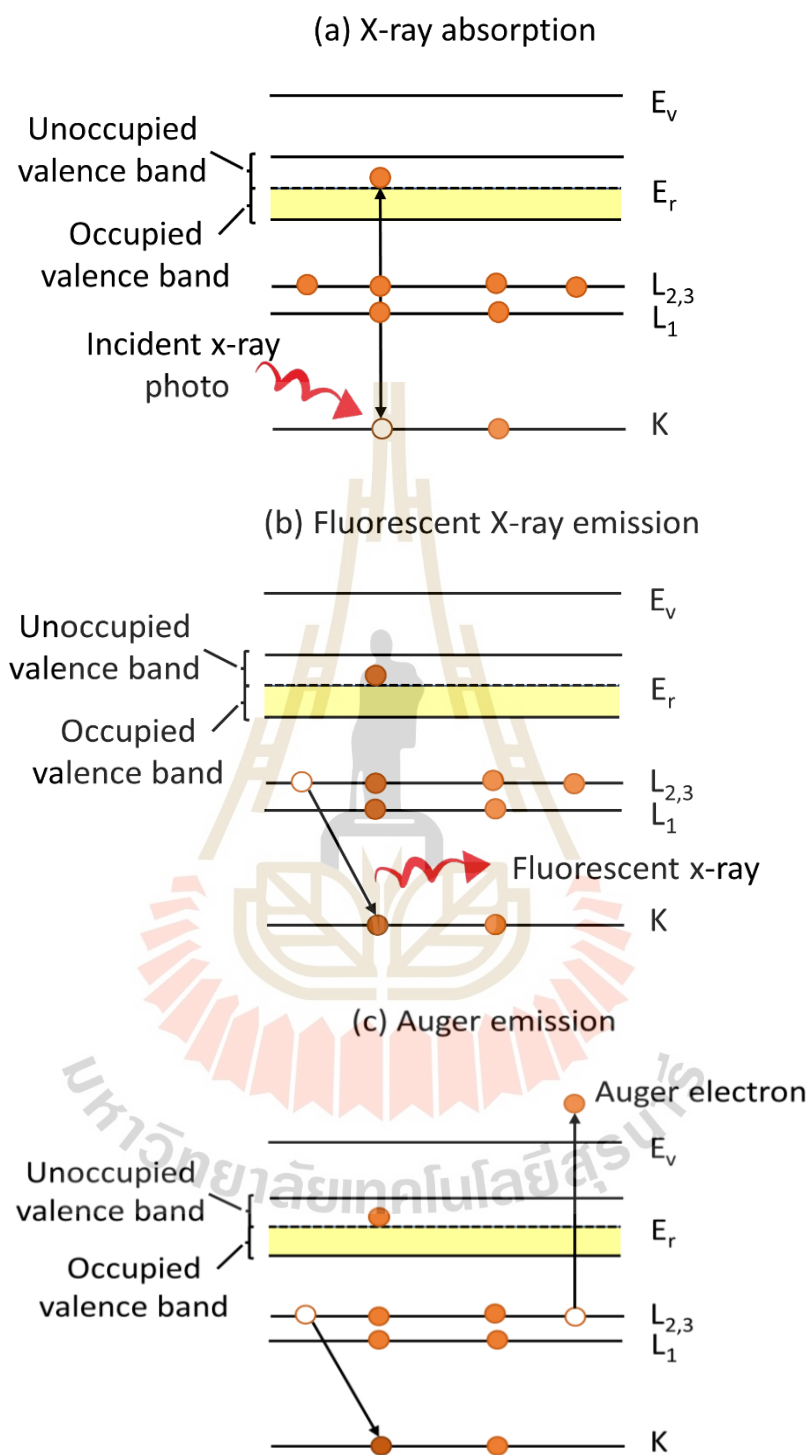


Figure 3.15 Fundamental processes of X-ray absorption, showing the excited state (a), fluorescent X-ray emission (b), and Auger emission (c) at the relaxation to ground state (Klysubun, 2006).

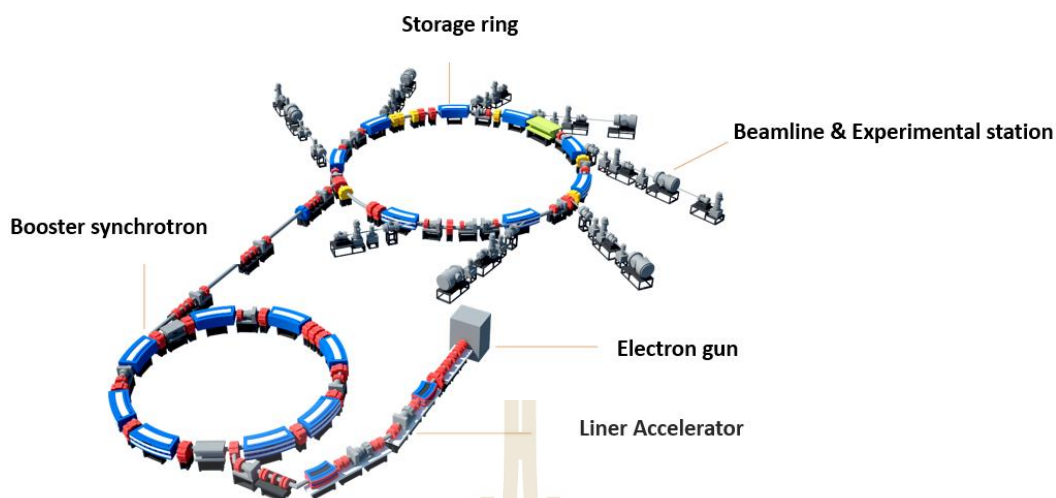


Figure 3.16 Schematic diagram of the synchrotron light source at SLRI. (Picture from <https://www.slri.or.th/en/102-uncategorised.html>)

The schematic of the beamline 5.2 set up is shown in Figure 3.17. The synchrotron light has a continuous spectrum covering from infrared to X-rays. A double crystal monochromator (DCM) equipped with crystal to select monochromatized light with photon energy ranging from 1240 to 12100 eV. InSb (111) and Ge (220) crystals are used in the monochromator to fill the photon energy range from 1830-7000 and 3440-12100 eV, respectively. This beamline allows the K-edge absorption spectra from Mg to Ge elements to be measured. There are 2 modes of measurement of XAS measurements i.e., transmission and fluorescence modes of measurements. The transmission mode corresponds to the absorption coefficient ($\mu(E)$) that is measured from the intensity of the X-ray beam (I_0) passing through the material thickness (t), giving the formular is $I = I_0 e^{-\mu(E)t}$ where I is the intensity of the transmitted X-ray beam. For the fluorescence mode, the X-ray fluorescence is detected by a 4-element silicon drift detector. The absorption coefficient $\mu(E)$ is proportional to the I_f/I_0 ratio.

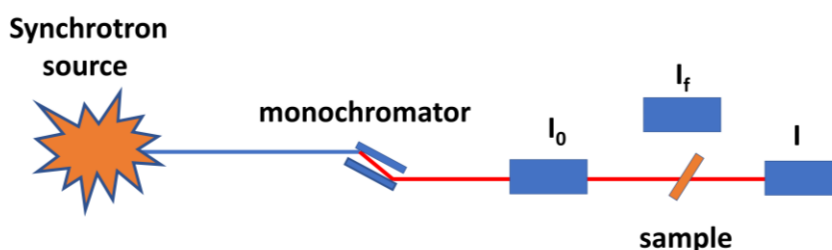


Figure 3.17 A schematic of the beamline 5.2 at SLRI.

3.3 Experimental procedures

This section provides the information of experimental procedures for different sub-topics of the investigations. Since the magnetic properties of LTP-MnBi depends on many parameters of starting materials, synthesis processes and final form of the materials. The flow-charts summarize the procedures covering experimental works in in this thesis.

Figure 3.18 are for the experiments to study the magnetic properties, crystal structure, morphology, and elemental composition of the LTP-MnBi material sintered in vacuum at temperature range of 275-375 °C. The starting Mn powder used in the sintering was ball-milled and sieved to be below 20 μm . The selected temperature range was considered with the fact that it must be above the melting point of Bi and below the temperature where HTP-MnBi is formed. This allows the sintering to be liquid-phase sintering where solid Mn is immersed or covered by liquid Bi. The sintering product is a rod with a shape of the containing quartz tube. The sintered product was not hard and, thus, could easily be ground to powder form.

The experimental procedures for the investigations of the formation mechanism of the sintered LTP-MnBi are given in Figure 3.19. The challenging work was to prepare the cross-sectional SEM/EDS MnBi particle samples. Thus, the size of the initial Mn powder particle for sintering shall be as large as possible. The Mn powder was used as received from the supplier. The larger particle, the easier sample preparation was expected. Cross-sectioned MnBi particles were necessary to observe the formation of the LTP-MnBi on the surface of the particles. Cracks in the Mn particle were observed unexpectedly, and lead to the study of diffusion in MnBi during sintering, which later turn to be interesting experiments.

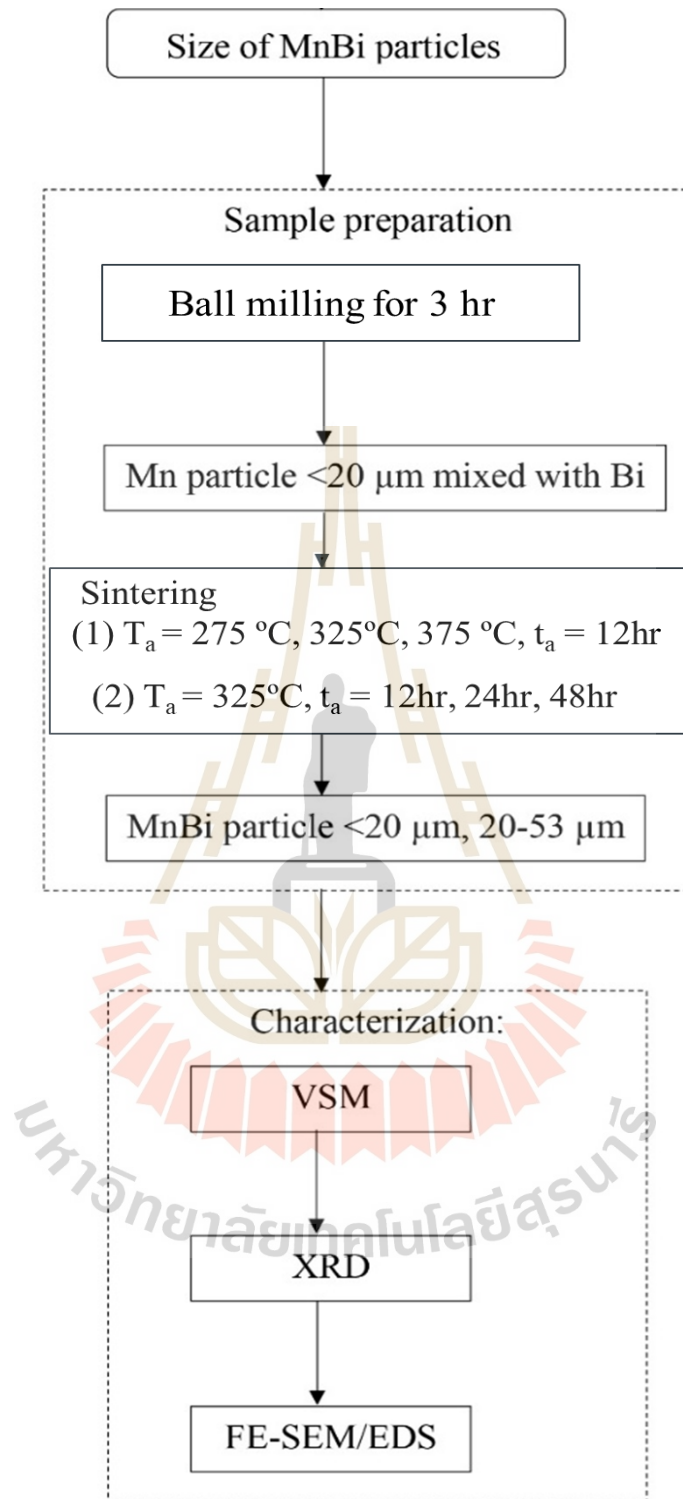


Figure 3.18 Flow-chart of the experimental procedure for the study of the magnetic properties, crystal structure, morphology, and elemental composition of the LTP-MnBi material sintered in vacuum at temperature range of 275-375 °C.

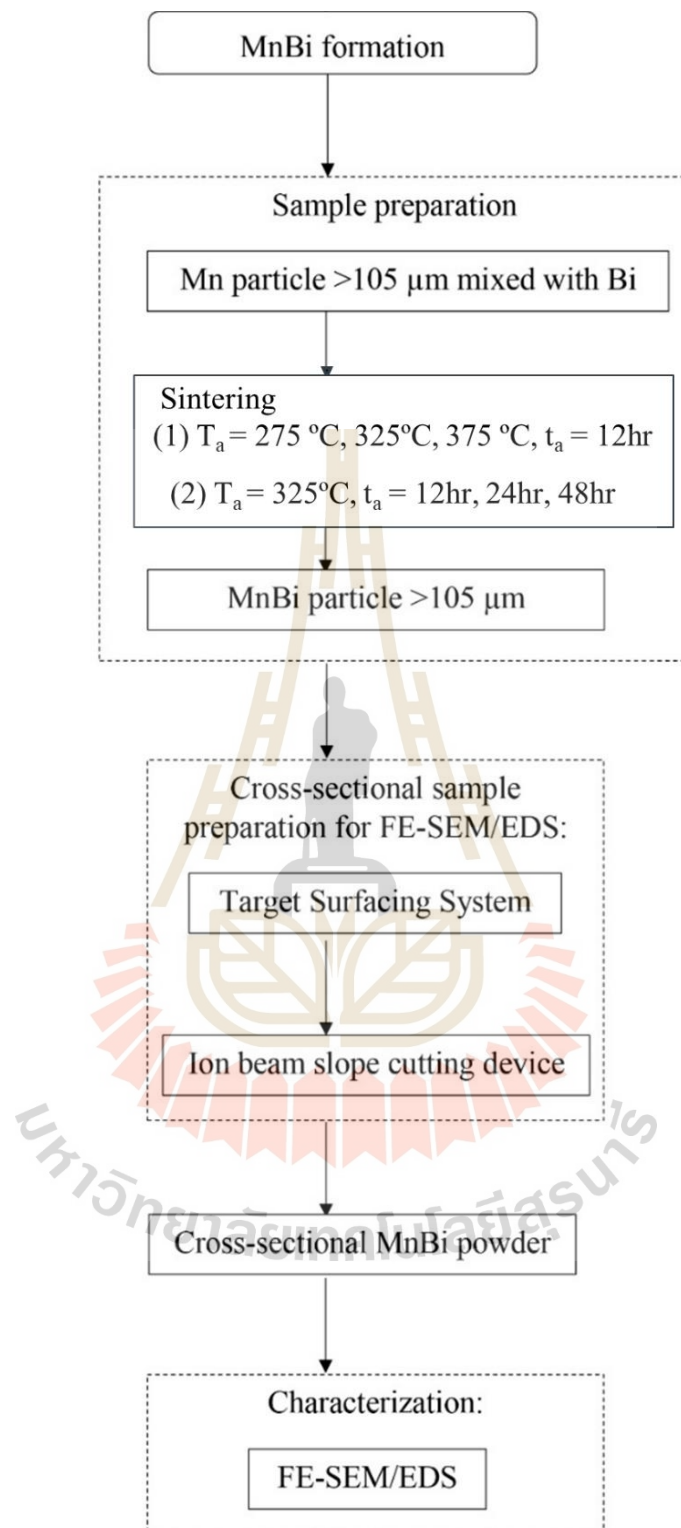


Figure 3.19 Flow-chart of the experimental procedure for the study of the formation mechanism of the sintered LTP-MnBi material sintered in vacuum at temperature range of 275-375 °C.

For the investigations of the stability of the sintered product or LTP-MnBi material at room temperature, the starting LTP-MnBi layers were formed by sintering of a mixture of Mn powder (particle size $<20\ \mu\text{m}$) and Bi powder at $275\ ^\circ\text{C}$ for 12 hrs. The magnetic properties of the fresh (newly prepared) and aging MnBi samples were studied by VSM. The important information of this experiment was about the aging sample which was loaded into a standard Quantum Design powder sample holder (P125E), shown in Figure 3.20, which is referred to a sealed tube from time to time. The $0.075\ \text{g}$ MnBi powder (mass; m) was densely compressed into the tube with diameter of $2\ \text{mm}$ and length of $3\ \text{mm}$. The volume of cylindrical Quantum Design VSM powder holder (V) is $9.42\ \text{mm}^3$. Using the relation $\rho = \frac{m}{V}$, the density (ρ) is $8.00\ \text{g/cm}^3$. The MnBi powder had a limited space in a sealed tube as seen in Figure 3.20. The powder sample was kept in the holder for the period of 18 months without taking it out. VSM measurements were performed during the 18 months. The investigations of the stability of the sintered product or LTP-MnBi material at room temperature were conducted by following the procedures in Figure 3.21.

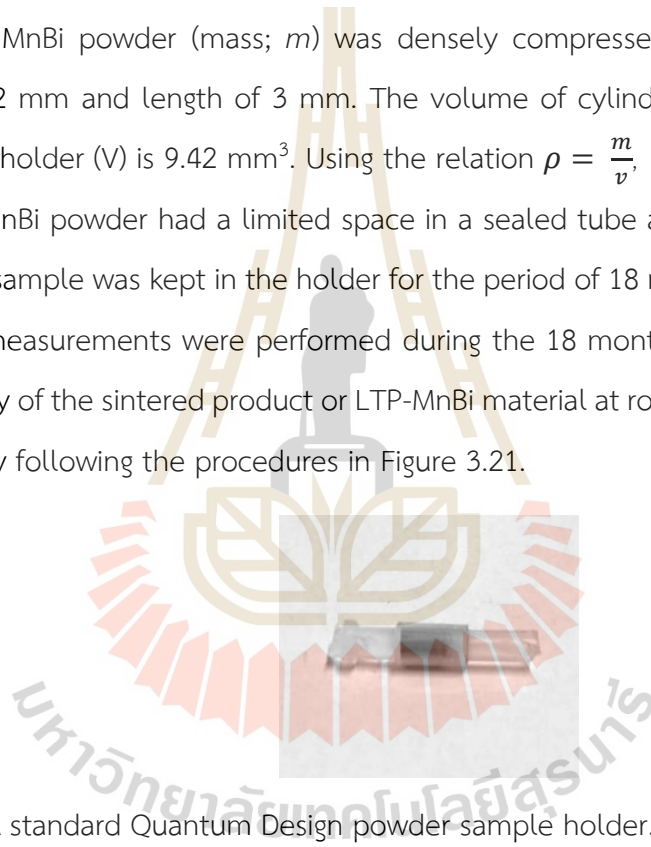


Figure 3.20 A standard Quantum Design powder sample holder.

Figure 3.22 shows the flow-chart of the experimental procedures for the study of the decomposition of LTP-MnBi at $150\ ^\circ\text{C}$. This elevated temperature was an accelerated test for degrading of the LTP-MnBi sample sintered at $275\ ^\circ\text{C}$ for 3 hrs. The starting Mn powder with particle size of less than $20\ \mu\text{m}$ was used in the sintering. Thin layers of MnBi were expected for this short duration of sintering and, thus, providing a complete decomposition of the material to be investigated. The decomposition was introduced by annealing the material at $150\ ^\circ\text{C}$ in air for different periods.

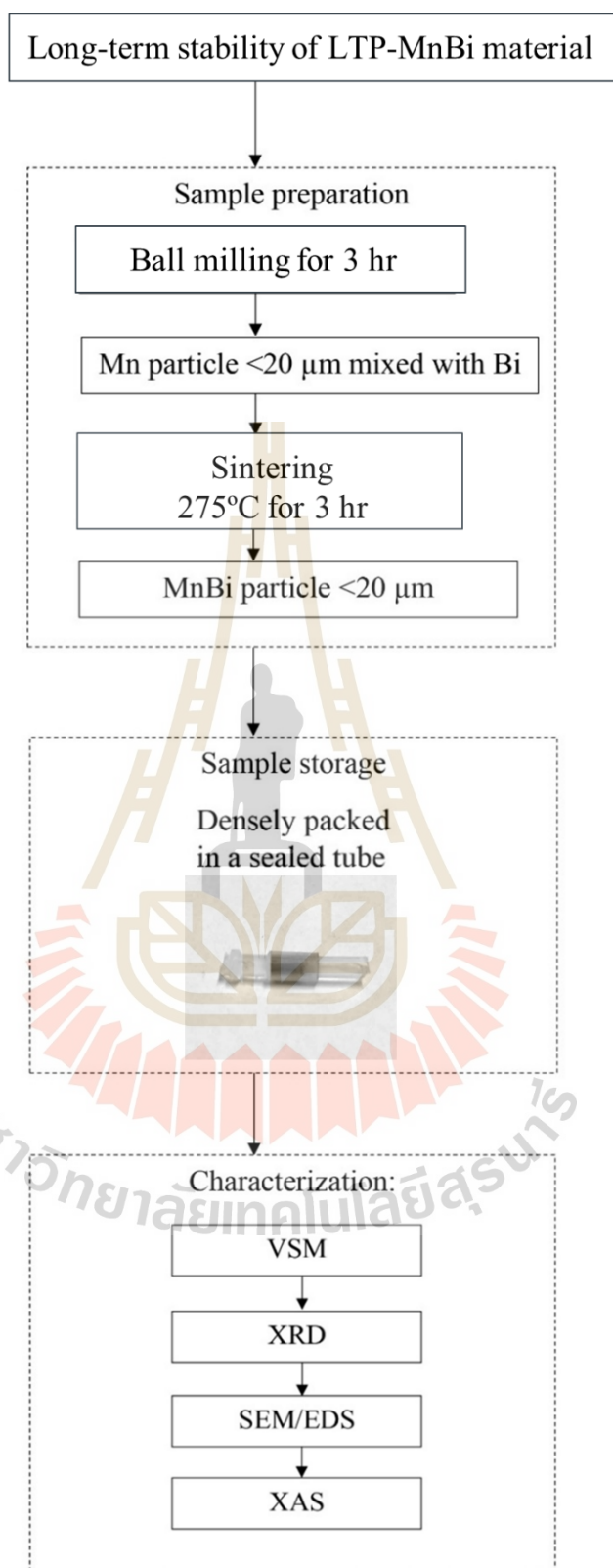


Figure 3.21 Diagram of long-term stability of LTP-MnBi material at different aging time, including MnBi characterization.

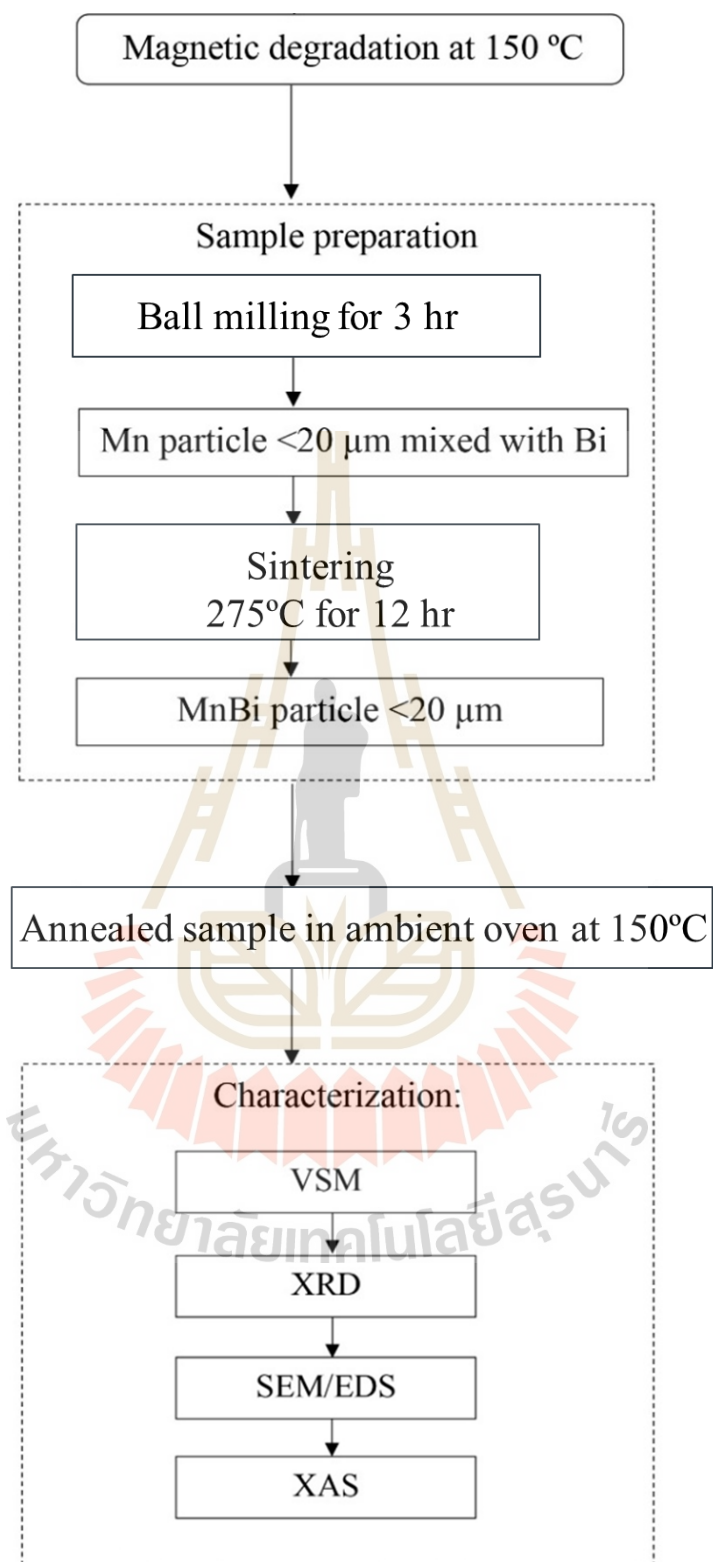


Figure 3.22 Diagram of a magnetic degradation with an evaluated heating time in ambient oven, including MnBi characterizations.

CHAPTER IV

RESULTS AND DISCUSSION

Sintering of a mixture of Mn and Bi powders is adopted for synthesizing LTP-MnBi due to its possibility for scaling up in production. To greatly reduce post-processing steps such grinding and low-temperature annealing, sintering was performed at temperatures just above melting point of Bi and low enough that high-temperature phase MnBi was not formed. This low temperature allows sintering to be in liquid phase, i.e., liquid-phase sintering (LPS). One more important consideration in designing the conditions for LPS is that the process must be taken place in an absence of oxygen to avoid formation of Mn oxides. It is noted again that the sintering was performed at vacuum pressure below 5×10^{-7} mbar.

The first two sections of this chapter report the phases, morphology, elemental composition, and magnetic properties of the sintered product. More importantly, the mechanism for the formation of LTP-MnBi during LPS is also explained. Two set of samples were investigated. The first set of samples was sintered at 275 °C, 325 °C and 375 °C for 12 hr. The second set sintered at 325 °C with different durations of 12, 24, and 48 hr, respectively.

The stability of magnetic properties is also essential when magnetic materials will be used in devices. It is known that the magnetic properties of LTP-MnBi could be affected by different factors such as crystal structure, and microstructure as oxidation (Janotová, Švec, Matko, Janičkovič and Sr., 2018; Ly et al., 2014; Villanueva et al., 2019) that could be altered by decomposition (Ly et al., 2014; Sun, Xu, Liang, Sun and Zheng, 2016) by exposure to humidity (Jacobson and Kim, 1987) and elevated temperature (S. Cao et al., 2011; Chen et al., 2015; J. Cui et al., 2014; D. T. Zhang et al., 2014) for an extended period of time. The studies of long-term stability of LTP- MnBi are reported in the third section of this chapter. The last section of this chapter covers the investigation of the decomposition of LTP- MnBi at 150 °C.

4.1 LTP-MnBi sintered at 275, 325 and 375 °C for 12 hours

4.1.1 Phase identification

After sintering, the sintered product was a rod with the inner shape of the quartz tube used in the effusion cell. The sintered product was ground and sieved into 2 sets of MnBi powder sizes, i.e., less than <20 μm defined as the small particle size and large particle size is defined for the 20-53 μm size. It is noted that the initial size of Mn was less than 20 μm prior to sintering. Thus, the large particles were resulted from agglomerations of smaller particles. The MnBi powders were characterized to study crystal structure by the X-ray diffraction technique (XRD) using a Bruker D2 phaser X-ray diffractometer. Figure 4.1 shows the XRD patterns taken from all sintered MnBi samples. The Bi phase (card No. 96-231-0890), MnBi phases (card No. 96-900-8900), and MnO phases (card No. 96-101-0394) were identified, appearing as diffraction peaks in the figure. However, Mn phase could not be detected due to the limit of X-ray penetration depth (P.-K. Nguyen, Jin and Berkowitz, 2013). The unreacted Mn was expected to be remain in the Mn powder particle under the forming MnBi layer. The thickness of the newly formed MnBi layer is thicker than the X-ray penetration depth, preventing the unreacted Mn in the powder particles to be detected. In addition, there is Bi covering on the particles, and thus the Bi further reduce the chance for X-ray to detect the Mn phase in this sintered product.

The obtained XRD patterns were analyzed to determine the crystallization quality. The crystallization quality could be calculated from the average full width at half maximum (FWHM), the first four main MnBi peaks i.e. (101), (002), (012) and (110) planes peaks were selected. The FWHM values of MnBi-275, MnBi-325 and MnBi-375 were 0.176, 0.194, and 0.214 degrees, for the small particle size and 0.164, 0.170, and 0.169 deg for the large particle size. Next, the crystallite size could be estimated from the Scherrer equation, that is $D = \frac{K\lambda}{B \cos\theta}$, where $K = 0.9$ is the shape factor constant. The crystallite size values of 51.4, 45.9 and 41.2 nm for the small particle size and 55.0, 52.1 and 53.3 nm for the large particle size, respectively. It is obvious that these values of all samples have similar values in range of 41-55 nm.

For more detailed analysis, the different phase contents for the small and large samples were estimated by using the Rietveld refinement method of XRD data using the FULLPROF program. The MnBi phase contents were found to be 56.1, 59.5, 52.8 wt% for the small particle size and 69.3, 70.1, 66 wt.% for the large particle size with sintering temperature at 275 °C, 325 °C and 375 °C, respectively. For both sample sizes, it is indicated that the MnBi content increased with sintering temperature from 275 °C to 325 °C and decreasing at 375 °C. The slight increase in MnBi content when sintering temperature increase from 275 °C to 325 °C may be due to the increase in the diffusion rate with temperature. A significant reduction in MnBi content of the MnBi sintered at 375 °C could be explained by the Mn-Bi segregation during LTP- to HTP-MnBi phase transition at temperature above 350 °C (Jun Cui et al., 2018). Due to the shallow X-ray penetration depth, Mn cores could not be detected, the content values reported here does not represent the exact MnBi ratio. One more interesting point obvious in the XRD pattern is that more Bi was observed in the smaller samples. This might be due to the fact that the unreacted Bi in the sintered product could easily be ground to powder with particle sizes smaller than 20 μm .

It is interesting to point out that MnO was also observed in the XRD patterns. The amount of the oxide was estimated to be less than a few wt.% for all samples. The base pressure of the sintering system was about 2×10^{-8} mbar, and the vacuum pressure during sintering process was controlled to be below 5×10^{-7} mbar, which is the upper limit pressure for filaments of the effusion. It is understood that at the sintering temperatures used in this work, Mn powder particles were coated or immersed in liquid Bi. More importantly, there is no significant difference in the amount of the oxide formed on the samples sintered at the three different temperatures. Oxidation rate is generally known to increase with temperature. Thus, oxide formation during sintering must be very low and below our detection limit. However, it was observed that the amount of the oxide increased with time after the sintered MnBi was exposed air. The formation of oxide at this stage might be considered as the degradation as there has been a report earlier (Janotová et al., 2018).

It is worth to emphasize that the single-step vacuum sintering method can be considered as a facile MnBi preparation method. Moreover, the purity of MnBi can be further enhanced by using magnetic separation (S. Kim et al. 2017), optimizing the Mn content (B.A. Jensen et al., 2019) or, in principle, reducing the starting Mn particle size.

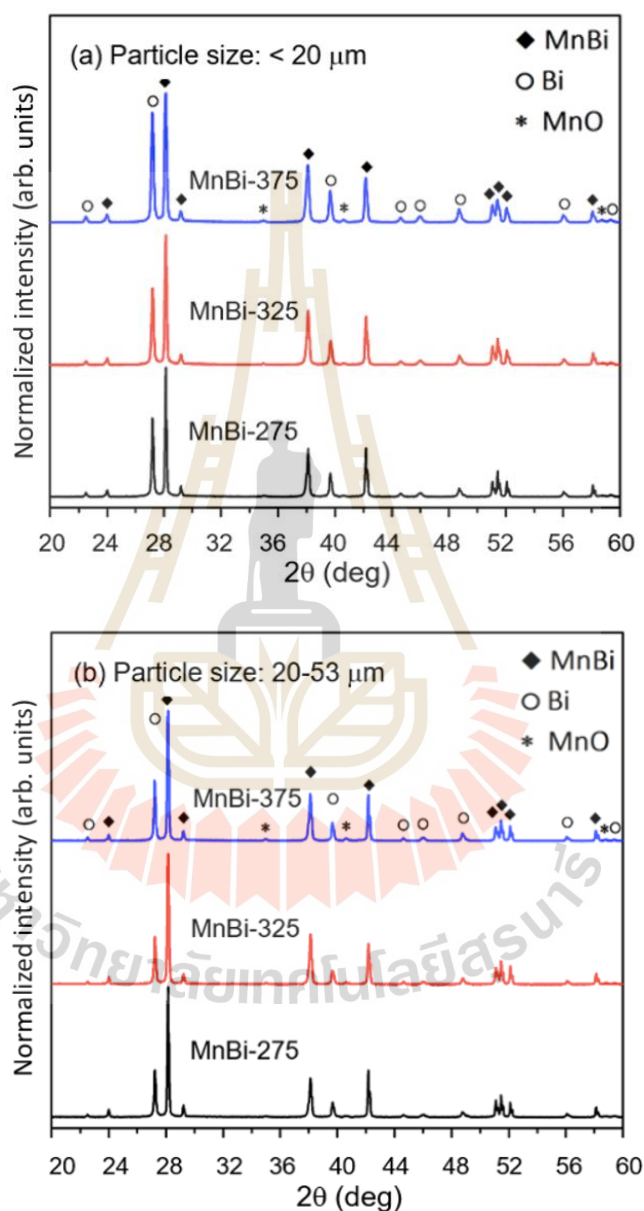


Figure 4.1 XRD patterns of LTP-MnBi powder prepared at various annealing temperature at 275 °C, 325 °C and 375 °C for small particle size of (a) $< 20 \mu\text{m}$ and (b) $20\text{-}53 \mu\text{m}$.

4.1.2 Morphology and size distribution

Figure 4.2(a) and (b) show SEM images of the MnBi-275 powder particles for two different size ranges illustrating their typical morphologies. The starting material of Mn powder particles was prepared to be less than 20 μm in size, and the individual Mn particles shall still be less than 20 μm in size because the sintering temperature is below the melting point of Mn. Thus, there is virtually no changes in particle size for Mn before and after sintering. The formation of MnBi is assumed to be mainly controlled by diffusion mechanism of the melted Bi. The single MnBi particle size was measured to be about 8 μm , as seen in Figure 4.2(a). It is obvious that the larger particle size is likely an agglomeration of several MnBi particles, bonded with Bi, with a total size of around 29 μm , as shown in Figure 4.2(b).

The elemental composition of the sintered product was investigated by the SEM/ EDS technique. EDS measurements of the MnBi powder particle sample, shown in Figure 4.2(a) were performed at three specific points. Since this technique cannot probe very deep into the bulk. The composition reported here is mainly surface composition. It was observed that the surface composition of the selected particle varies from position to position, as indicated by the white (point A and B) and grey (point C) areas. The calculated Bi/Mn content ratios are given in the inset of Figure 4.2(a). It was found that there are two main distinguished areas two different ratios; those are the MnBi rich area with Bi/Mn ratio ~ 1 and the Bi-rich area with Bi/Mn ratio $\gg 1$. It is noted that the area Mn-rich area (Bi/Mn ratio $\ll 1$) was not observed.

From the analysis of SEM images and EDS spectra, the whole MnBi formation process can be explained as follows. At a sintering temperature higher than the Bi melting point, Bi is melted to be liquid migrating over the surfaces of Mn powder particles. It is expected that the Mn powder particles were covered by liquid Bi. At the interface between solid Mn and liquid Bi, there is the chemical interactions between Bi and Mn to form an MnBi layer. The thickness of the MnBi layer is increased by diffusion of Mn and/or Bi across the forming MnBi layer. Since the atomic ratio of 1:1 for the starting Mn and Bi powder was used in

the sample preparation, the single-phase MnBi could be expected in the completed sintering process.

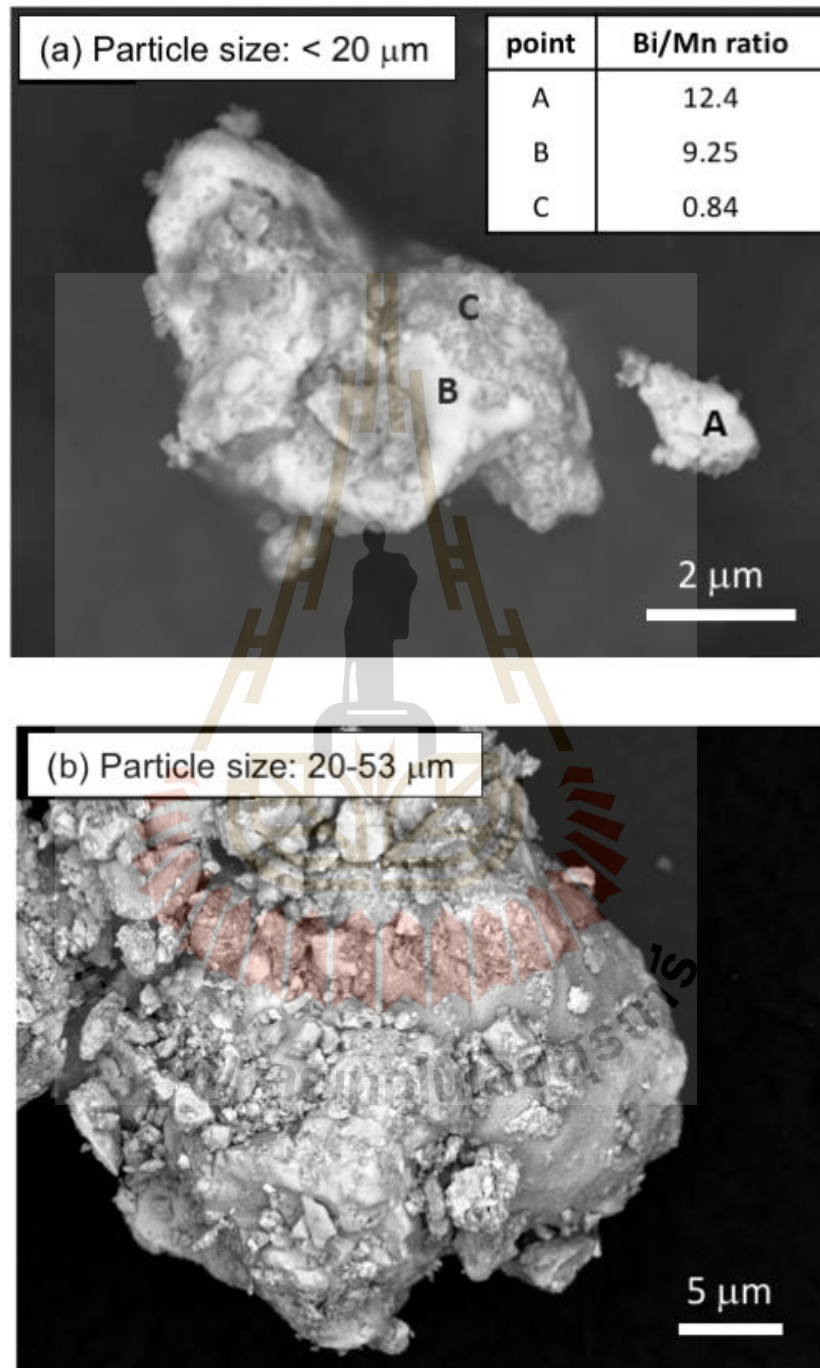


Figure 4.2 SEM images of the MnBi samples sintered at 275 °C with particle sizes of (a) $< 20 \mu\text{m}$ and (b) $20\text{-}53 \mu\text{m}$. The inset in (a) is the Bi/Mn ratio obtained from the EDS analysis of three specific locations.

However, because the starting Mn powder particle is large, the formation of the MnBi layer is, thus, limited by the diffusion mechanism. The evidence of an incomplete process can be observed by the excessively Bi-rich areas (points A and B of Figure 4.2(a)) and the Bi phase detected from XRD results. From above arguments, it is expected that unreacted Mn shall remain in the sintered product even though this unreacted Mn could not be detected by the XRD and SEM/EDS measurements. Cross-sectional MnBi powder particle sample for EDS measurement was required to identify this assumption, which are to be shown below.

4.1.3 Magnetic properties

Figure 4.3(a) and (b) show the experimental room-temperature M-H curves with a demagnetizing field correction for the small and large MnBi particle sizes, respectively. The inset of Figure 4.3(a) shows the demagnetization curves of raw M ($N = 0$), corrected M ($N = 0.4$), corrected B ($N = 0.4$) and the $(BH)_{max}$ area (dashed rectangle) of the small MnBi particle size sample. Demagnetizing field correction is necessary for analysis of the M-H curves taken from strong magnetic materials because VSM measurements are open-loop measurements. The corrected magnetic field is $H_{int} = H_{applied} - 4\pi N_D M$, where N_D is the sample demagnetization factor (SI units) and M is the volume magnetization in emu/cm^3 . This H_{int} parameter can be calculated the magnetic induction equation is created from $B = H_{int} + 4\pi M = H_{applied} + 4\pi M(1 - N_D)$. The area of the largest square in the second quadrant multiplied by the value of point B and H is the maximum energy produce. The square loop with a demagnetizing field correction is improved while the value of H_{ci} and M_s has not changed. It is noted that the measured samples were in the powder form, not in a compressed bulk, composing of Mn particles with LTP-MnBi surface layer and Bi.

The values of weight percentage of MnBi content and important magnetic properties of all sintered MnBi samples are given in Table 4.1. The small particle sizes samples sintered at 275 °C, 325 °C and 375 °C have the intrinsic coercivities (H_{ci}) of 4.88 ± 0.24 , 4.98 ± 0.24 and 6.0 ± 0.30 kOe, and the saturation magnetizations (M_s) of 44.99 ± 2.25 , 45.79 ± 2.29 and 39.61 ± 1.98 emu/g, respectively.

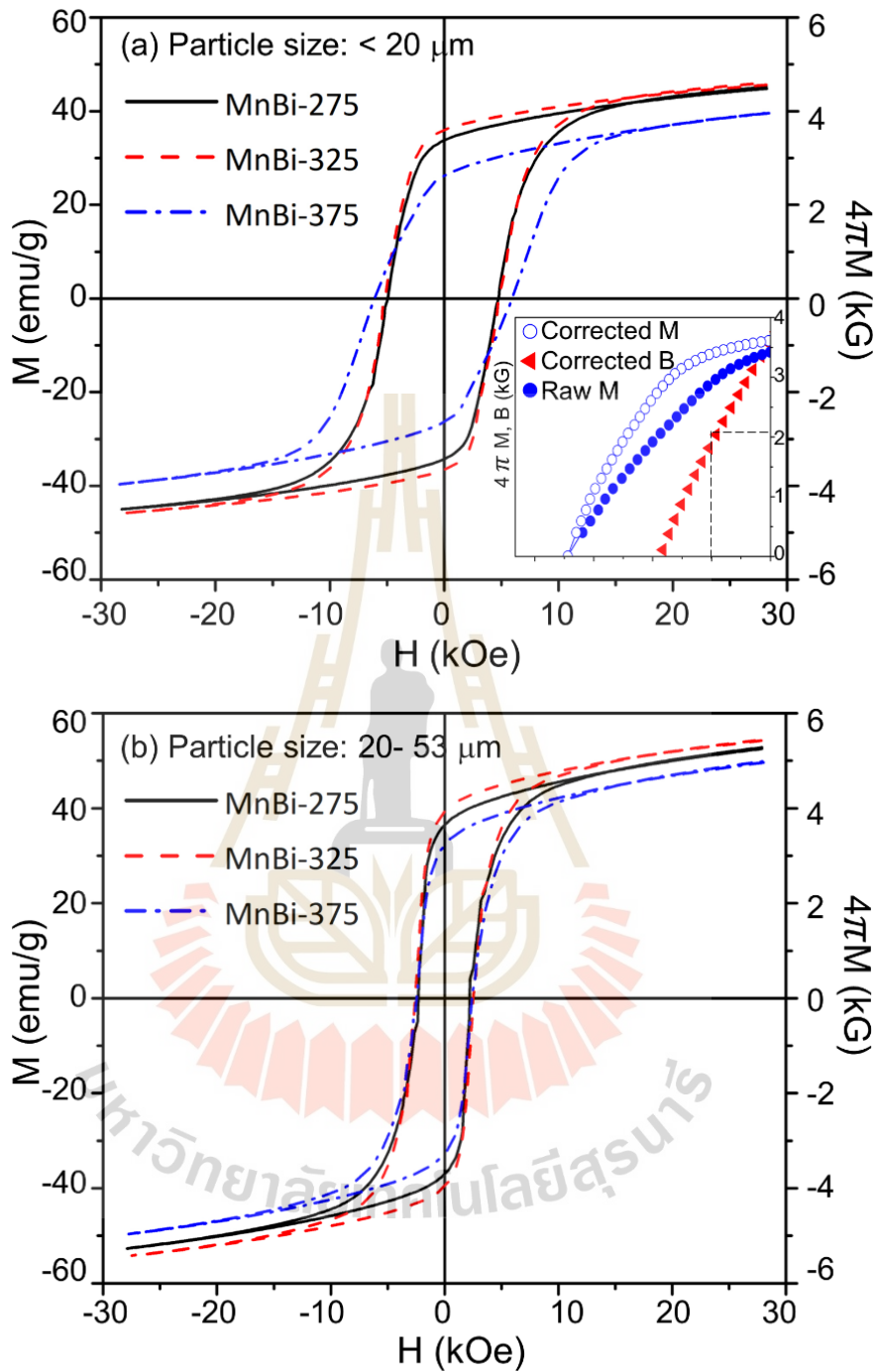


Figure 4.3 The M - H curves with demagnetizing field correction of the MnBi samples sintered at 275, 325 and 375 °C for particle sizes of (a) $< 20 \mu\text{m}$ and (b) $20-53 \mu\text{m}$. The inset in (a) shows the demagnetization curves of raw M ($N = 0$), corrected M ($N = 0.4$), corrected B ($N = 0.4$) of the small MnBi sintered at 325 °C. The $(BH)_{max}$ is the dashed rectangle with maximum area.

The M-H curve of the small MnBi size sample sintered at 325 °C shows better performance magnetic properties than the small MnBi sample sintered at 275 °C. This may be explained by a higher formation rate of MnBi layer at higher sintering temperature, leading to high LTP-MnBi content in the sintered product. It is important to note that the shape of M-H curve for small size MnBi sample sintered at 375 °C is different from those sintered at lower temperatures. The value of H_{ci} increases but the M_s decreases. The M_s is related to MnBi content, therefore it is suggested that sintering at 375 °C might cause the formation of HTP-MnBi. The formation of HTP-MnBi consequently is affected to achieve the low MnBi content. This observation from VSM is similar what have been observed in the XRD patterns reported above.

Table 4.1 The weight percentage of MnBi content and magnetic behaviors of all sintered MnBi sample.

Sample ID	MnBi (wt.%)	M_s (emu/g)	H_{ci} (kOe)	$(BH)_{max}$ (MGOe)
small MnBi-275	56.1	44.99 ± 2.25	4.88 ± 0.24	2.46
small MnBi-325	59.5	45.79 ± 2.29	4.98 ± 0.24	2.84
small MnBi-375	52.8	39.61 ± 1.98	6.00 ± 0.30	1.48
big MnBi-275	69.3	52.64 ± 2.63	2.09 ± 0.12	2.33
big MnBi-325	70.1	54.27 ± 2.73	2.49 ± 0.10	2.63
big MnBi-375	66.0	49.71 ± 2.48	2.54 ± 0.14	1.78

From the data presented in Table 4.1, it is obvious that the small particle size MnBi sample exhibits higher H_{ci} but slightly lower M_s , which is agreed with other reports (J. Cao et al., 2019; X. Li, Pan, Zhen, Lu and Batalu, 2019). The H_{ci} of small MnBi particle is approximately higher 2 times than that of the large one. The higher H_{ci} observed in

smaller particles could result from the refinement of MnBi grains, leading to more uniform rotation of magnetic moments (B. Li et al., 2018; Y. Zhang et al., 2017). There has been a report of the theoretical saturated magnetization of for LTP-MnBi, which was calculated to be 80 emu/g at room temperature (Sarkar and Basu Mallick, 2020). This theoretical value of the saturated magnetization may be used to estimate the LTP-MnBi fraction or content, assuming a linear relation between the fraction and the saturated magnetization. For the small and large particle size samples sintered at 275 °C, the LTP-MnBi was found to be 56% and 65.6%, respectively. The results deduced from VSM measurements are consistent with the XRD results showing that patterns for smaller particle sizes contain higher diffraction intensity peaks from elemental Bi. There has been also a report showing that the decrease in magnetization could be (Kharel et al., 2013). It is apparent that samples with diverged particle sizes have a similar tendency of $(BH)_{max}$ with varied sintering temperature. The highest $(BH)_{max}$ of 2.84 MGOe was obtained in the small MnBi sample sintered at 325 °C. The magnetic properties of all MnBi powders are summarized in Table 4.1.

Figure 4.4 shows the M-H curves of fresh and 10-month-old MnBi-275 measured at different sample temperatures. These MnBi sample was sintered at 275 °C for 12 hours. There is an obvious difference in the M-H curves for the fresh and old sample. The old sample exhibits the degradation since the sample was left in air for extended time (M. Y. Sun et al., 2016) which is the topic for the last section of this chapter. The interesting result is the measurement results taken from the 10-month-old sample at different sample temperatures, i.e., 300K, 350K and 400K. There are continuous changes in shape of the M-H curve when the temperature increases from 300K to 400K. The M_s decreases while the H_c increase with the sample temperature which is similar to what have been observed with MnBi prepared by different techniques (J. Cao et al., 2019; Chen et al., 2016; J. Cui et al., 2014). It is noted that the kinks of magnetization curve are larger at higher measuring temperature, which created from the weakened coupling between different magnetic phases such as MnBi, Mn, Bi and amorphous (Xie et al., 2016; Yang et al., 2014), including to the possible formation of new phases at elevated temperature during the VSM measurements.

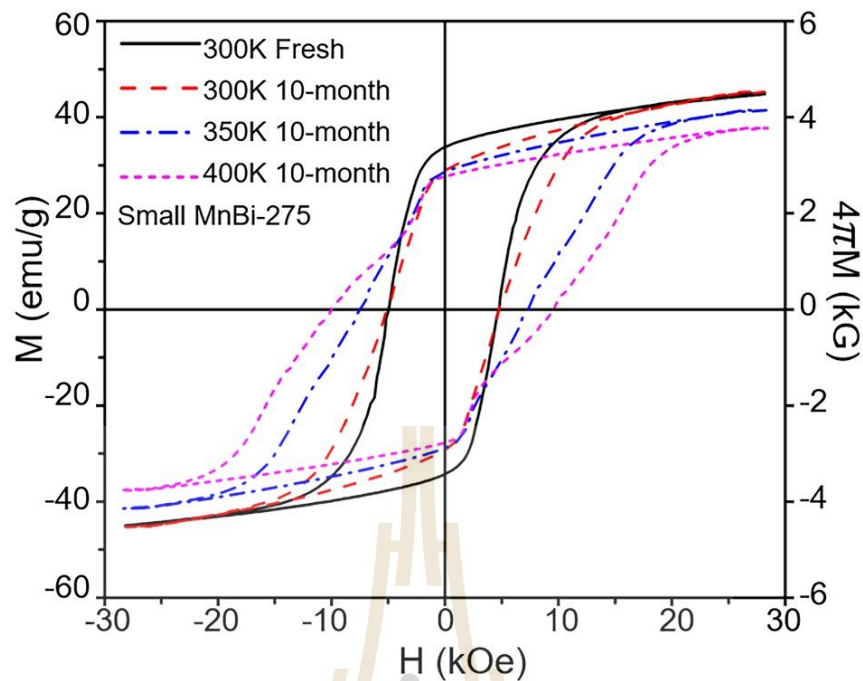


Figure 4.4 M-H curves measured at sample temperature of 300K, 350K and 400K for the fresh and 10-month-old MnBi samples sintered at 275 °C showing the increase of coercivity with temperature.

4.1.4 Depth profile and diffusion in MnBi layers

Huge efforts have been spent in preparing cross-sectional powder particles for SEM/EDS measurements for investigation of elemental depth profile and diffusion of Bi and Mn in MnBi layer. A cross-sectional SEM micrograph of an as-received Mn powder particle with size of about 100 μm is shown in Figure 4.5(a). Even without any sample treatments, there many cracks in the Mn powder particle as shown in the figure. For this study, this as-received Mn powder was mixed with Bi powder and then sintered at temperatures in the vicinity of liquid-phase sintering (LPS), in which Mn remains solid while the Bi transforms to liquid. It was expected that, upon LPS, Bi transforms to liquid covering the Mn powder particles. Some Bi flows into the cracks in the Mn particles. Bi atoms interact with Mn atoms at the surface of the particle and at both surfaces of the cracks. LTP-MnBi formed at the external surface of Mn particles and the interior-surfaces along the cracks.

After sintering process, the cross-sectional SEM for MnBi powder particles sintered at 275 °C, 325 °C and 375 °C which are shown in Figure 4.5(b), (c) and (d), respectively. All-sintered cross-section MnBi samples show a spider-web feature composite of white areas (Bi rich), and gray areas (Mn rich) in the Mn particles. The white areas appear near the cracks and the external surface of Mn particles, and these areas is expected to be LTP-MnBi layers formed during. At melting point of Bi, Bi transformed to liquid Bi while Mn remains solid. Bi interact with Mn to form MnBi layer at the external surface of Mn particles and the interior-surfaces along the cracks.

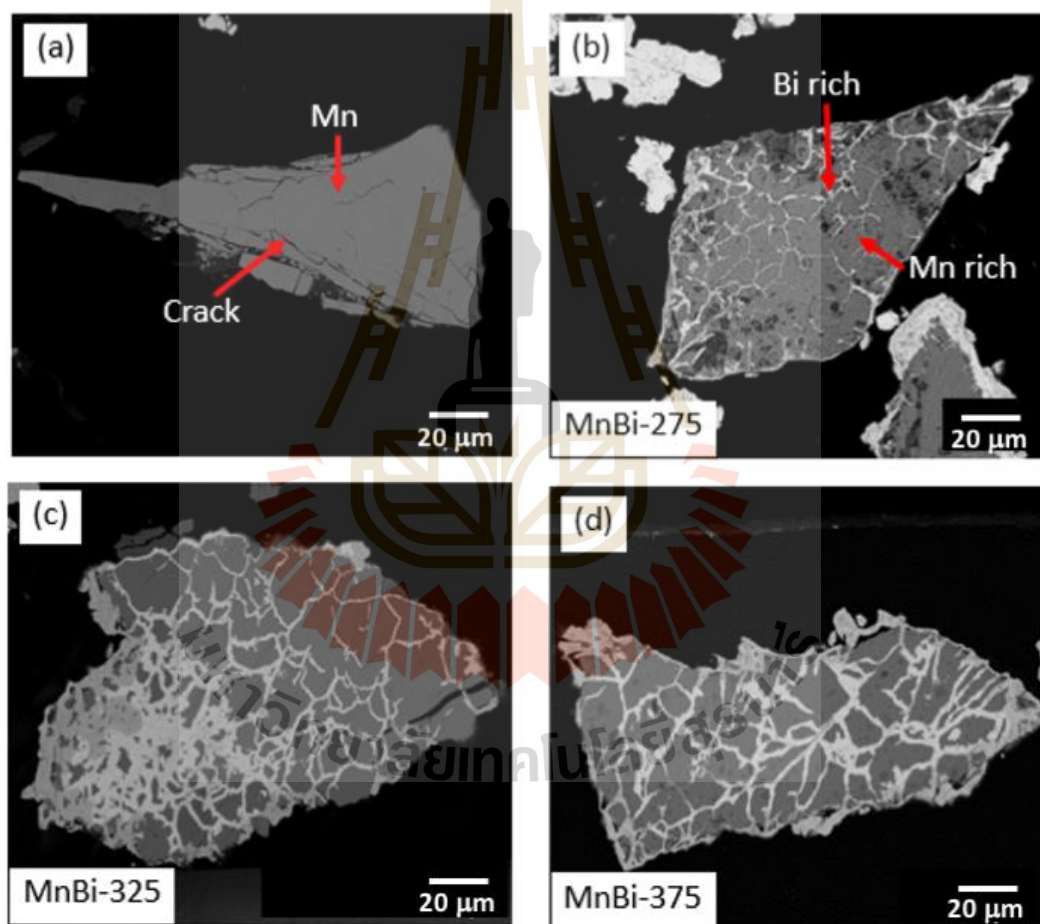


Figure 4.5 The cross-sectional SEM images of (a) as-received Mn powder particle (b) Mn powder particles sintered at 275 °C (c) at 325 °C and (d) at 375 °C.

Figure 4.6(a) shows the typical zoom-in cross-sectional SEM micrograph near the crack in MnBi particle sample sintered at 325 °C, which appears as a vertical grey line in the middle of the figure. The formation of MnBi layers occurred at both side-surfaces of the crack and extended deep into the bulk. This results in the formation of MnBi layers along crack surfaces, which appear as the bright stripes along both sides of the crack in the SEM image. Further from cracks, only unreacted bulk Mn is observed: the grey areas on both sides. The observed thicknesses of the MnBi stripes formed on opposite sides of a crack are different. There is no symmetry reason for the MnBi layers formed on opposite banks of the Bi river to grow at precisely the same rate. The difference may be dominated from the effect of sample preparation being conducted at an angle to the crack as shown in the inset of Figure. 4.6(a).

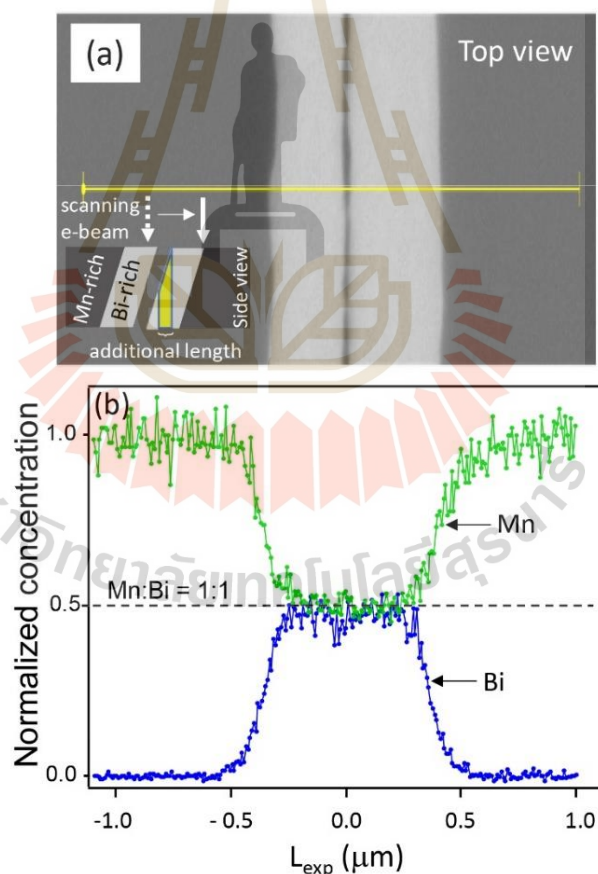


Figure 4.6 (a) Zoom-in cross-sectional SEM image of the MnBi sintered at 325 °C. Inset illustrates the side-view schematic which may yield to different forming thickness between each side of the crack. (b) The Bi and Mn concentration profiles along the yellow line of (a).

The elemental depth profiles of the MnBi layers were obtained from EDS line scans along the yellow line in Figure. 4.6(a) The Mn and Bi depth profiles taken from the MnBi sample sintered at 325 °C are shown in Figure. 4.6(b). They indicated that the sintered MnBi layers are composed of homogenous and graded regions. Near the surface of the cracks, homogenous MnBi regions formed with Mn and Bi in an atomic ratio of 1:1. Beyond this homogenous region, the concentration of Bi decreases with depth. For this EDS line scan shown in Figure. 4.6(b), the Bi concentration is saturated over the distance of 0.3 μm apart from the side-surface of the crack. The concentration significantly drops in the range of 0.3 μm to 0.5 μm where tiny amount of Bi was detected afterwards. This trend is opposite for the Mn concentration profile.

The MnBi layers formed at the surfaces of the cracks in the Mn powder particles were used for investigation of the diffusion coefficient (D_c) because the thickness of MnBi layers from elemental depth profiles provide an opportunity to estimate D_c . In this work, net diffusion is defined as the diffusion through a growing MnBi layer during sintering, which includes the effect of Bi flow into the Mn bulk and Mn flow towards the crack surface. The average value of D_c can be simply estimated using the diffusion relation $D_c=L^2/t$, where t and L are the diffusion duration and length, respectively (Van Nguyen and Nguyen, 2017). The diffusion length (L) is the thickness of MnBi layers measured from the cross-sectional SEM images. For each sintered MnBi powder particle shown in Figure. 4.5(b)-(d), the thickness of the MnBi layer was measured at 120 different regions over the whole area of the cross-sectional SEM images using ImageJ program (Schneider, Rasband and Eliceiri, 2012). The width of the two MnBi fringes, on opposite sides of the crack, typically differ by a factor of order ten percent (which may be a geometric factor related to the orientation of the crack relative to the cleaved surface). Accordingly, we take the average of the two fringes as a reasonable representation of the typical thickness of MnBi layers.

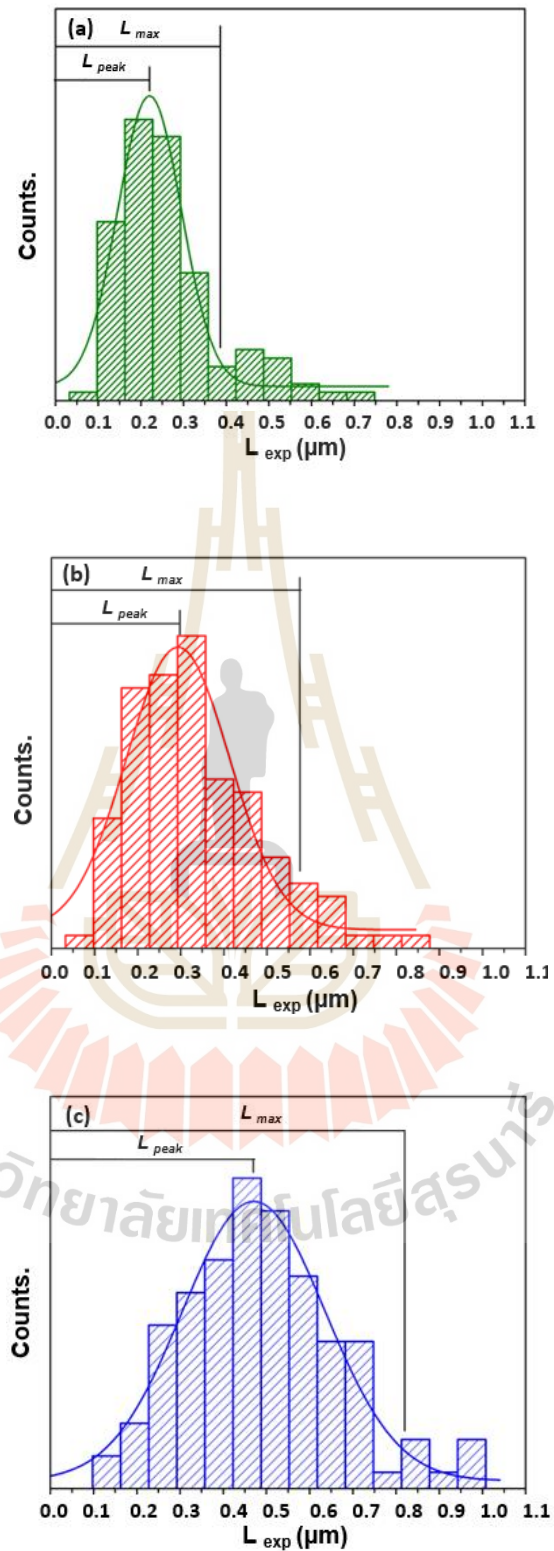


Figure 4.7 Histograms of the thickness of MnBi layers in the MnBi samples sintered at 275 °C, 325 °C and 375 °C. Each bin of the histogram is 0.05 micron.

The histograms of the measured thicknesses of the MnBi layers sintered at 275, 325 and 375 °C are shown Figure 4.7. The variation in layer thickness evident from the histograms reflects the complex nature of LPS kinetics. Indeed, the growth of layers must result from the flow of liquid Bi through irregular cracks and the resulting diffusion of Bi perpendicular to the liquid streams into the surrounding Mn landscape. It is not surprising that this process, dependent on the crack properties, on the Mn-Bi interface at the crack edges and the subsequent diffusion rate into the sample, gives rise to a range of MnBi layer growth rates. Nevertheless, the statistical properties of the distribution of layer thickness provides insight into diffusion averages in experimental conditions.

To characterize the distributions, the histograms were fitted with Gaussian distributions. The mean (L_{peak}) and standard deviation (σ) are reported in Table 4.2. The thickest MnBi layers (L_{max}) that contribute significantly to the distribution can be represented by $L_{\text{max}}=L_{\text{peak}}+2\sigma$. One might expect that such thick MnBi layers are similar to those formed on the external surface of Mn powder particles, where the growth rate is not limited by the flow of liquid Bi through the crack (i.e., when the supply of Bi is always sufficient). This suggests that L_{max} can be used as a reasonable lower-end estimate of the diffusion length D_c for the net diffusion in the sintered MnBi layer at 275, 325 and 375 °C was found to be 1.41×10^{-14} , 2.49×10^{-14} and 5.72×10^{-14} cm²/s, respectively. The obtained D_c is of the same order of magnitude as the experimental data for other alloys reported earlier (S. Yoshida, Okumura, Kita, Takahashi and Ushioda, 2014). However, our values are up to 2 orders of magnitude smaller than that previously reported for diffusion in the arc-melted MnBi (Gupta, Anil Kumar and Khanra, 2018). This large discrepancy might be due to the difference in the material systems where large D_c in previous report was obtained by observing the change in size of Mn embedded in the arc-melted MnBi annealed at 300 °C.

One of the basic characteristics of diffusion processes is activation energy. This activation energy is generally estimated from the well-known Arrhenius equation; $D_c = D_0 \exp(-E_a/K_B T)$, where D_c , D_0 , E_a , K_B and T are diffusion coefficient, pre-exponential factor, activation energy of diffusion, Boltzmann constant and

temperature in Kelvin, respectively. By linear fitting of $\ln(D)$ and $(1/T)$, the D_0 and E_a could be obtained as shown in Figure 4.8. The coefficient follows the Arrhenius equation with the pre-exponential factor of $5.33 \times 10^{-10} \text{ cm}^2/\text{s}$ and activation energy of 0.45 eV.

Table 4.2 The mean, standard deviation, diffusion length, and diffusion coefficient of MnBi prepared by different sintering temperatures.

Sintering Temperature (°C)	Peak position, $L_{peak} \pm \sigma/2$ (μm)	Diffusion Length, $L=L_{peak}+2\sigma$ (μm)	D_c (cm^2/s)
275	0.247 ± 0.035	0.387	3.47×10^{-14}
325	0.328 ± 0.062	0.576	7.68×10^{-14}
375	0.497 ± 0.079	0.813	15.30×10^{-14}

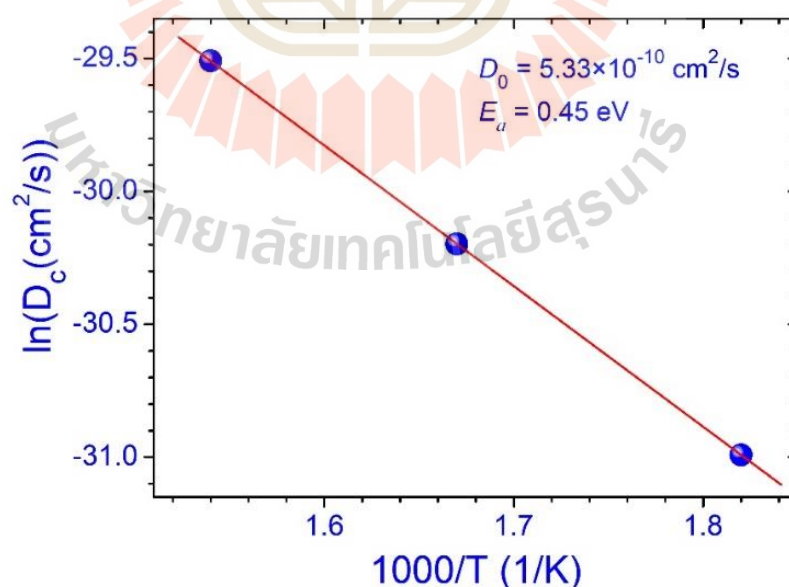


Figure 4.8 Arrhenius plot of the diffusion coefficient as a function of inverse temperature.

4.2 LTP-MnBi sintered at 325 °C for 12, 24 and 48 hours

It was shown in section 4.1 that among the three sintering temperatures, LTP-MnBi sintered at 325 °C yield the highest value of $(BH)_{max}$. In this section, the experimental results to verify that the value of $(BH)_{max}$ could still be increased when the LTP-MnBi content increases. By sintering at 325 °C with longer sintering times, the LTP-MnBi shall be produced with thicker layers and, thus, higher content of LTP-MnBi in the sintered product. In this section, the results from the investigations of the sintered MnBi products prepared at 325 °C for 12, 24 and 48 hr are reported.

4.2.1 Phase identification

Figure 4.9 shows the XRD patterns of the small MnBi powder (particle size $< 20 \mu\text{m}$) and large MnBi powder (particle size of $20\text{-}53 \mu\text{m}$) measured by using a Rigaku Smart Lab Diffractometer ($\text{CuK}\alpha$, 1.54 \AA) with 2θ of $20\text{-}60^\circ$. The MnBi powders were sintered at vacuum pressure below 5×10^{-7} mbar at 325 °C for 12, 24, and 48 hours, denoted as 325 °C_12hr, 325 °C_24hr, and 325 °C_48hr samples, respectively. Three main phases could be identified from the XRD patterns, which are Bi phase (card No. 96-231-0890), MnBi phases (card No. 96-900-8900), and MnO phases (card No. 96-101-0394). It is noted that MnO was also detected. This oxide was discussed in the previous section that it might be formed after the sintered product was taken out from the vacuum and exposed to air. The MnBi/Bi content ratio was estimated from the height of the MnBi and Bi intensity ratio. For the small particle size samples, the MnBi/Bi content ratio was found to be 1.68, 3.13 and 1.98 for the samples sintered for 12, 24, and 48 hrs, respectively. While the large samples, these ratios were 2.67, 4.79 and 3.40 for 12-, 24-, and 48-hr sintered samples, respectively. The two tends increase and decrease after the sintering temperatures increase. The MnBi/Bi content ratio did not increase as a linear function of sintering time as expected. This expected result is one of the issues for further study.

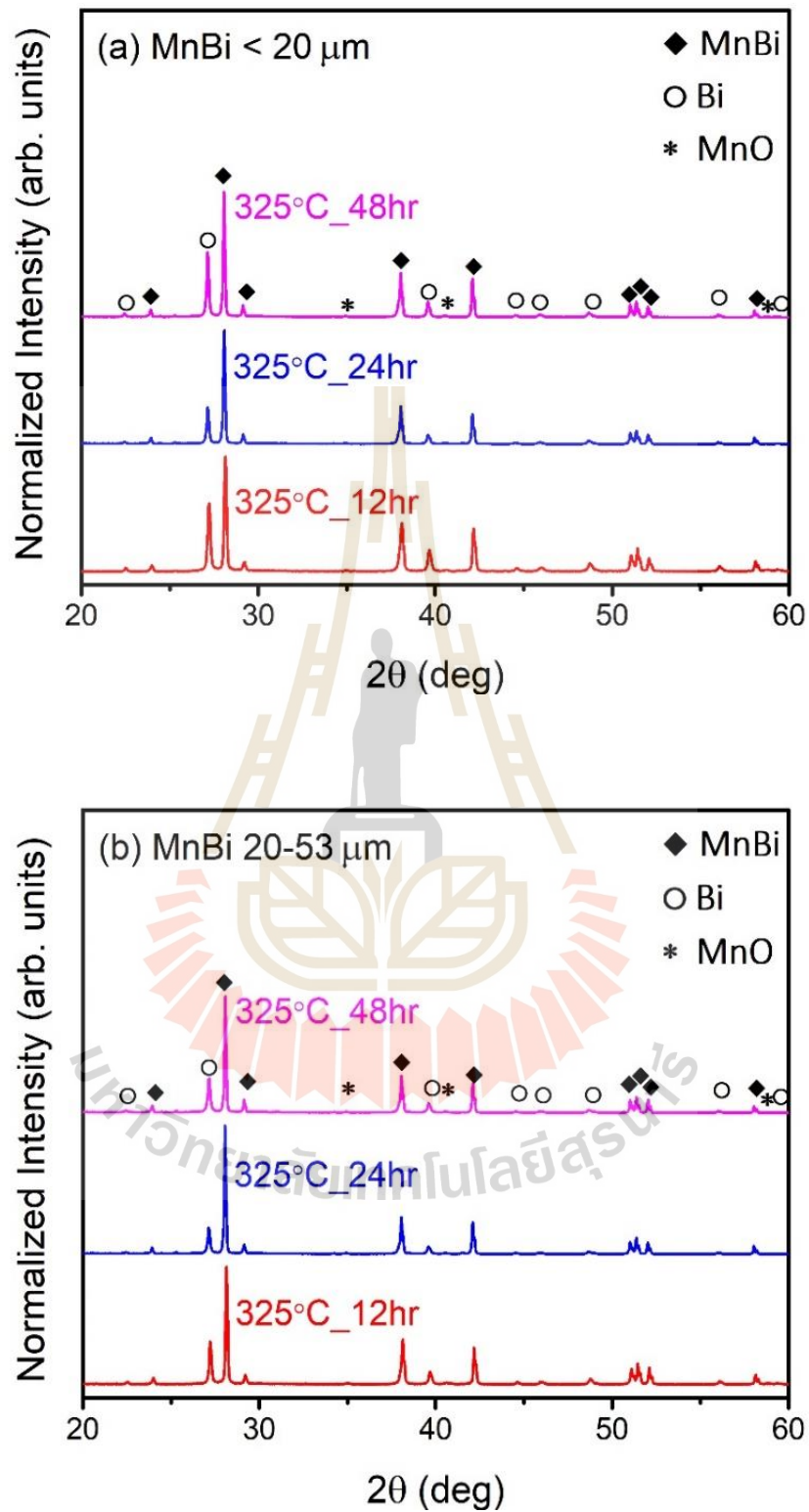


Figure 4.9 XRD patterns of the MnBi samples with (a) small particle size ($< 20 \mu\text{m}$) and (b) large MnBi particle sizes (MnBi 20-53 μm). The MnBi samples were sintered at 325 °C for 12, 24, and 48 hrs.

4.2.2 Magnetic properties

Figure 4.10 shows the room temperature M-H curves with demagnetization field correction of the MnBi powder samples sintered at 325 °C for different durations. For the sintered MnBi sample with small particle size, the H_{ci} are 4.98 ± 0.24 , 2.74 ± 0.13 and 2.04 ± 0.10 kOe, and M_s are 45.79 ± 2.28 , 55.07 ± 2.75 and 55.78 ± 2.78 emu/g for sintering times of 12, 24, and 48 hrs, respectively. For the samples with large particle size, the H_{ci} are 2.49 ± 0.12 , 1.55 ± 0.07 and 1.71 ± 0.08 kOe, and M_s are 54.27 ± 2.71 , 59.89 ± 2.99 and 62.79 ± 3.13 emu/g for sintering times of 12, 24, and 48 hrs, respectively. It is apparent that the H_{ci} decreases and M_s increases with increasing particle size. This is in an agreement with the results obtained from the MnBi samples sintered at 275, 325 and 375 °C for 12 hrs, as reported and discussed in the previous section that the lower values of H_{ci} is from the fact that large particles are the agglomerations of smaller particles bonded with Bi and, thus, the rotations of particles is more restricted. For the same set of sample size, the increase of M_s may be explained by the increase of LTP-MnBi content since longer sintering times result in more LTP-MnBi is formed.

It is interesting to point out the difference in shape of the M-H curves for the samples sintered for different durations. For small particle samples, the H_{ci} decreased 45% from 4.98 to 2.74 kOe when the sintering time increased from 12 to 24 hrs. However, when the sintering time increased from 24 to 48 hrs, the H_{ci} decreased only by 25% from 2.74 to 2.04 kOe. It is well understood that the value of H_{ci} increases with decreasing of MnBi particle size. For the 12-hr sintering sample, the thickness of LTP-MnBi layers formed on the exterior of the particles and interior surface on the crack surface in the particles are thinner than that for the 24- and 48-hr sintered samples. These thin layers, as compared to the magnetic domain, give rise to a higher value of H_{ci} than that for the thicker LTP-MnBi layers.

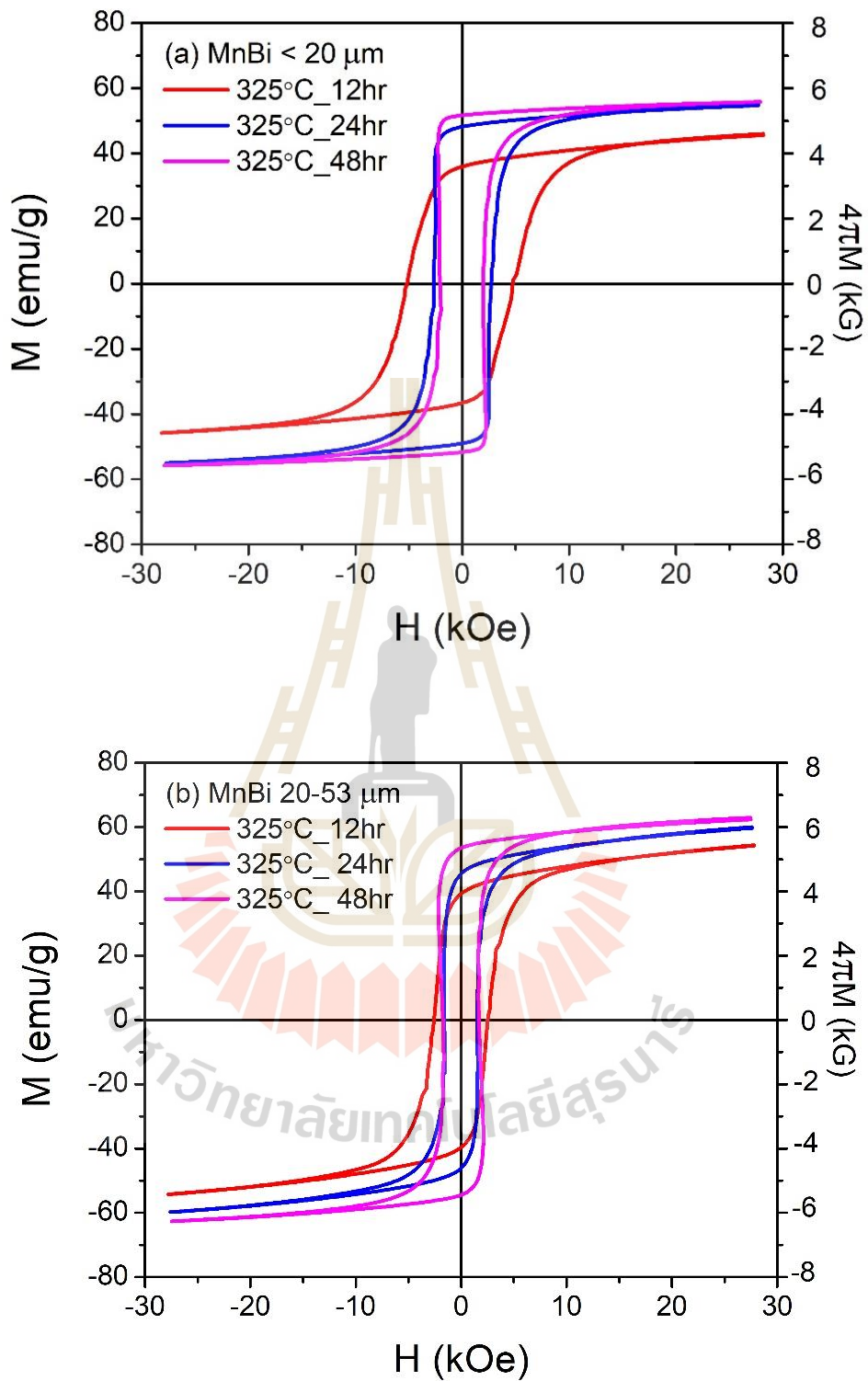


Figure 4.10 Room temperature M-H curves with demagnetization field correction of (a) the small MnBi particle size and (b) large MnBi particle size samples sintered at 325 °C for 12, 24, and 48 hrs.

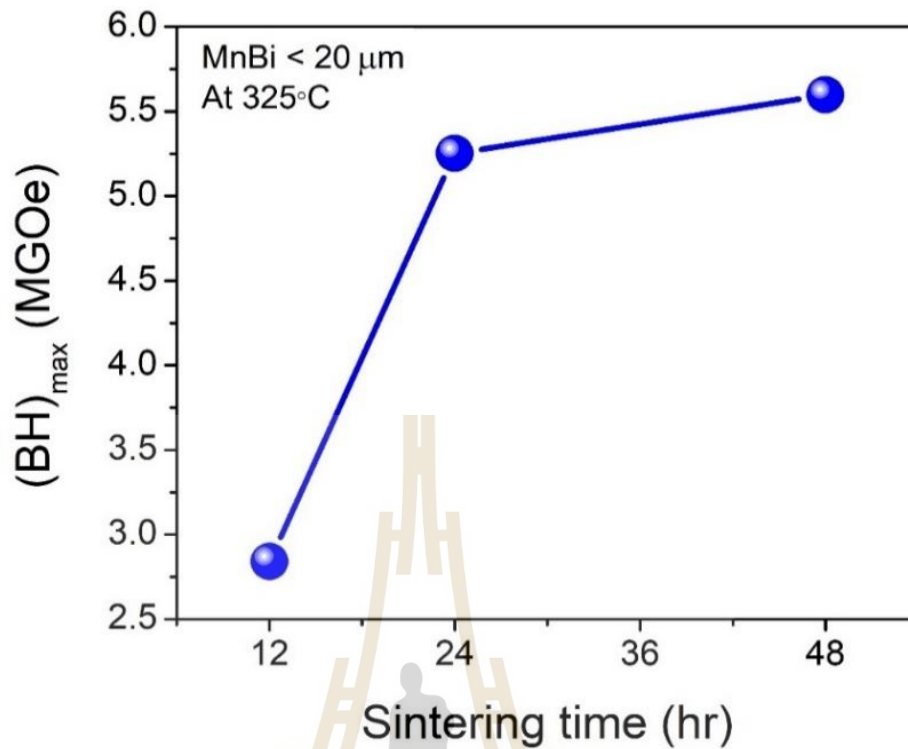


Figure 4.11 The energy product, $(BH)_{max}$, of the MnBi samples with particle sizes less than 20 μm as a function of sintering time.

Figure 4.11 shows the value of $(BH)_{max}$ as a function of sintering time. Only the small particle size samples are of interest in order to avoid the considerations of the effects from the particle agglomerations. The energy product is in general considered as one of the performance indicators of magnetic materials and magnets. The higher energy product, the higher potential for the magnetic materials and magnets to generate energy. The values of $(BH)_{max}$ are 2.84, 5.25, and 5.59 MGOe for the samples sintered for 12, 24, and 48 hrs. This trend of $(BH)_{max}$ is similar to the trend in earlier report (Mican, Hirian, Isnard, Chicinaş and Pop, 2015). It is interesting to note that LTP-MnBi prepared in this work yields $(BH)_{max}$ for as high as those synthesized by melt-spinning process (Kim et al., 2017; Yang et al., 2012), even though the values of the melt-spinning samples were from the pre-magnetic aligned samples. This, again, confirms that the low-temperature vacuum-sintered LTP-MnBi exhibits comparable performance with other advances technique. However, the technique used in this work consumes less energy and time and can be up scale easily for mass production.

4.2.3 Diffusion in MnBi layers

A cross-sectional MnBi powder particle sintered at 325 °C for 48 hrs, as shown in Figure 4.12(a), was prepared by an Ar ion beam slope cutting device.

The brightest areas, mostly, surrounding the MnBi powder particle are Bi. There are also the areas with brightest tone on the powder particle, which are also identified to be also Bi. This indicates that the powder particle was, in fact, partially cross-sectioned, only the central part of the particle was well cross-sectioned. More materials should have been removed to obtain good cross-sectional sample for the whole MnBi particle, however, it was not necessary for this study. The grey areas, mostly in the central part of the particle, are the un-interacted Mn. MnBi observed on the sample were from the MnBi formed at the exterior surface of the Mn particle, seen as the bright continuous area on the outer part, and the MnBi formed at the side-surfaces of the crack in the Mn powder particle, seen as a spider-web feature extending from the outer to inner parts. The formation of the MnBi layers on the crack surfaces were observed as two bright stripes sandwiching the crack, as shown in the higher resolution SEM images in Figure 4.12(b), (c), and (d) for the particle samples sintered at 325 °C for 12, 24 and 48 hrs, respectively. The processes involving this formation of MnBi were discussed in the previous section. The main mechanism for controlling the thickness of these MnBi is diffusion Mn and Bi through the forming MnBi layer. As expected, a longer sintering time, the thicker MnBi layer was formed. This is of course the result from the diffusion limited mechanism. The symmetry of the MnBi layers observed was the resulted from the fact that the crack surface was not perpendicular to the surface of the cross-sectional sample (Borsup et al., 2022).

The same method, as employed in the previous section, for estimating the thickness of the MnBi layers form on the inside surface of the crack was carried out. Figure 4.13(a), (b), and (c) show the histogram of the thickness of the MnBi layers formed on the crack surfaces for the particles sintered at 325 °C for 12, 24, and 48 hrs, respectively. Each histogram was obtained from measuring the zoom-in SEM image as shown in Figure 4.12 for a total of 120 data points using the program Image J (Schneider et al., 2012).

Then, the histograms were fitted with a Gaussian function. The average diffusion length was estimated to be $L_{peak} + 2\sigma$, where L_{peak} , σ are the peak position and the standard deviation of the Gaussian function, respectively. The results were used to calculate the mean, standard deviation, and a maximum MnBi layer thickness as shown in Table 4.3.

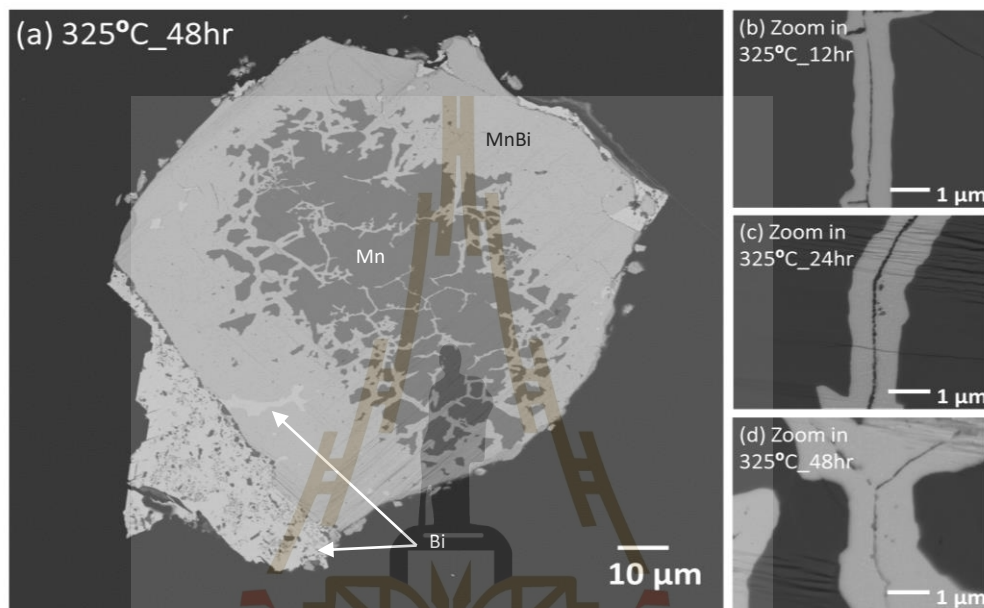


Figure 4.12 (a) A cross-sectional MnBi powder at 325 °C for 48 hr was prepared by ion beam slope cutting device and the zoom-in SEM images of a cross-sectional MnBi powder in the (b) 325 °C_12hr, (c) 325 °C_24hr, and (d) 325 °C_48hr at nearly the crack, respectively.

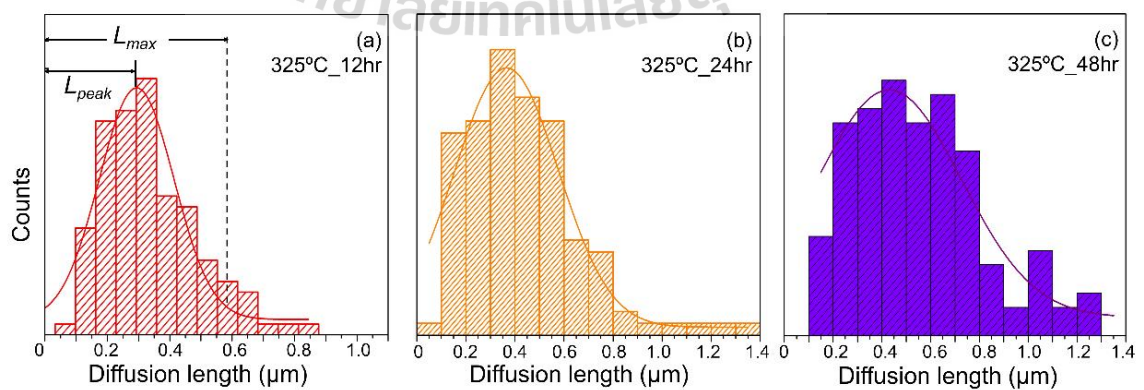


Figure 4.13. Histogram of the thickness of MnBi layers in the (a) 325 °C_12hr, (b) 325 °C_24hr, and (c) 325 °C_48hr. Each bin of the histogram is 0.05 μm.

Table 4.3 The mean, standard deviation, and the maximum MnBi layer thickness prepared at different sintering time.

ID Sample	Peak position, $L_{peak} \pm \sigma/2$ (μm)	Diffusion length, $L_{max} = L_{peak} + 2\sigma$ (μm)
325 °C_12hr	0.328±0.062	0.576
325 °C_24hr	0.366±0.105	0.786
325 °C_48hr	0.431±0.148	1.023

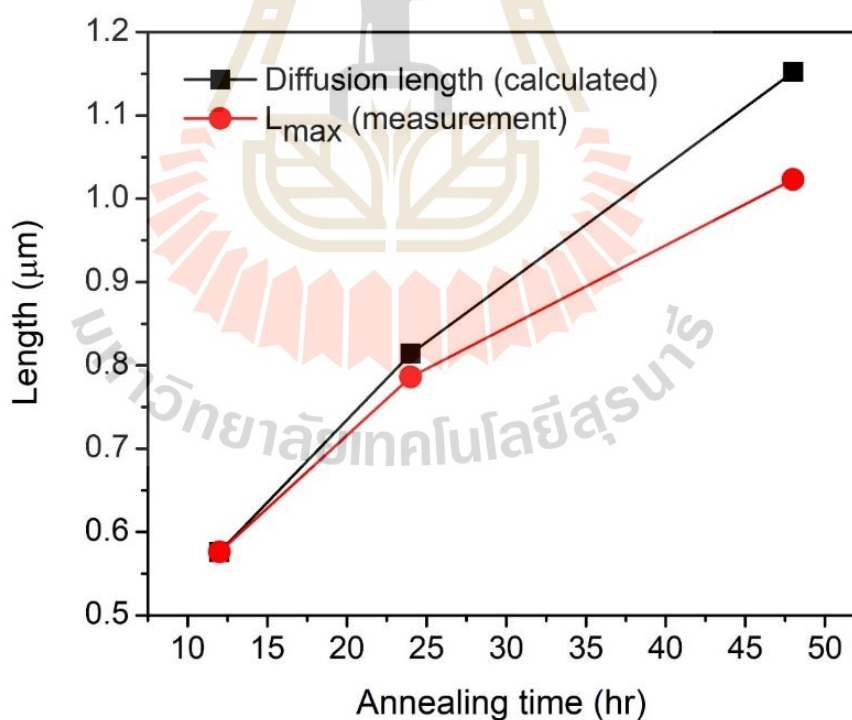


Figure 4.14 Comparison of calculating MnBi layer thickness in the 1st order diffusion equation and experimental MnBi layer thickness prepared at 325 °C for 12hr, 24hr, and 48hr, respectively.

Figure 4.14 presents the comparison of the MnBi layer thickness calculated from the first order diffusion equation and the experimentally measured MnBi layer thickness formed by sintering at 325 °C for 12, 24, and 48 hrs. In previous section, the diffusion coefficient of the MnBi powder (D_c) were deduced from the samples sintered at 275, 325 and 375 °C for 12 hrs. $D_c = L^2/t$ where t is a duration time and L is the diffusion length or the MnBi layer thickness. The D_c values were 3.47×10^{-14} cm²/s, 7.68×10^{-14} cm²/s, and 15.30×10^{-14} cm²/s for sintering temperatures of 275 °C, 325 °C, and 375 °C, respectively. With the known diffusion coefficient, the diffusion length or the thickness of the MnBi layers could be calculated from the relation $L = \sqrt{D_c t}$. The calculated MnBi layer thickness values were 0.576 μm, 0.814 μm, and 1.152 μm for the samples with sintering time 12, 24, and 48 hrs, respectively. The calculated values were close to the experimentally measured MnBi layer thicknesses which were 0.576 μm, 0.786 μm, and 1.023 μm. There is the difference in the calculate and measured values, and the difference increases with sintering time. This might be that the 1st order diffusion equation may not be adequate for prolonged sintering. The 1st order diffusion equation is generally accurate for diffusion in a short distance or short diffusion time. That is the case shown in the figure.

4.3 Long-term stability of LTP-MnBi

The product from liquid-phase sintering a mixture of Mn and Bi powders at low-temperature in vacuum composed LTP-MnBi, Bi and Mn. Thermal stability of this sintered product is of great important for future utilizations. This section reports the changes in magnetic property, structures and chemical of the sintered product over an extended period. Mn and Bi powder with atomic ratio of 1:1 was mixed and sintered at 275 °C for 3 hrs in vacuum. The particle size of Mn powder was below 20 μm. After sintering, the sample was ground and sieved to select powder particles with size of less than 20 μm. The fresh and 18-month-old MnBi samples were investigated by different characterization techniques i.e., VSM, XRD, SEM/EDS, and XAS. The 18-month-old MnBi sample was the sintered MnBi powder packed in a sealed tube, which is in fact a sample container of the VSM system.

4.3.1 Magnetic properties

The room temperature M-H curves with demagnetization field corrector of the MnBi powder stored in a sealed tube as a function of storing time are shown in Figure 4.15. The important parameters of the magnetic property are given in Table 4.4. It is noted that sealing of the VSM container is not vacuum sealing, it is just an ordinary lid of a plastic container. For over the 18 months, the sample was always kept in the tube. It is obvious that there were almost no changes in the M-H curve after the sample was stored for 2 months. The dramatic changes were observed when the sample was 7 months old. Both coercivity and remanent magnetization increased by approximately 30%. After storing for another 7 months, the coercivity and remanent magnetization kept increasing but with lower increasing rates. For the 18 months old sample, the coercivity increased but the remanent magnetization decreased slightly as compared to the 14 months old sample. It is interesting to note that, for the whole storing period of 18 months, the energy product increase with storing time while the saturated magnetization remained almost unchanged, very slight reduction though. The change pattern of the M-H curve for MnBi have not been reported before. Thus, it was worthwhile for in-depth investigations to understand physics behind the change.

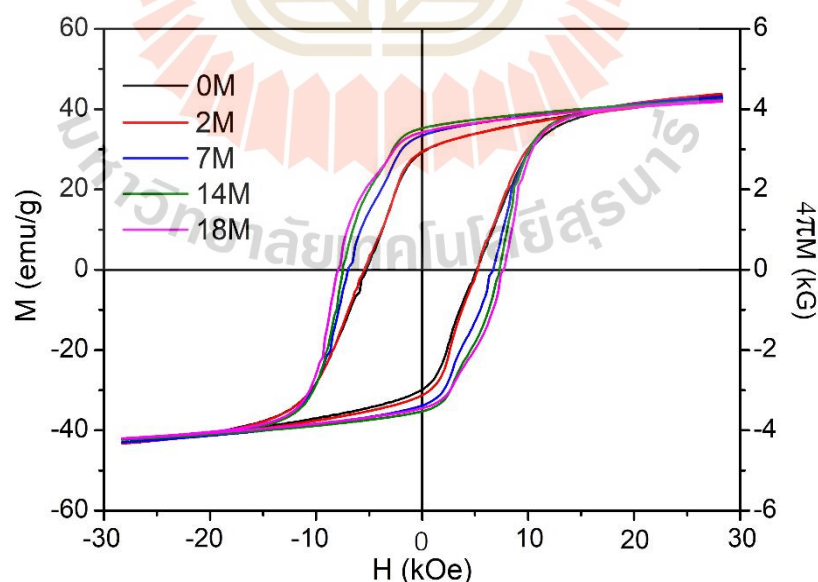


Figure 4.15 Room temperature M-H curves with demagnetization field correction of the samples stored in a sealed tube up to 18 months.

Table 4.4 Magnetic properties (H_c , M_s , $(BH)_{max}$) of MnBi sample at different ages or storing periods.

Sample or ID/Storing time	H_c (kOe)	M_s (emu/g)	$(BH)_{max}$ (MGOe)
0M	5.15 ± 0.26	43.23 ± 2.16	1.77
2M	5.34 ± 0.27	43.21 ± 2.16	1.92
7M	6.87 ± 0.34	43.05 ± 2.15	2.50
14M	7.43 ± 0.37	42.34 ± 2.11	2.84
18M	7.81 ± 0.39	41.98 ± 2.15	2.70

4.3.2 Surface morphology of LTP-MnBi powder

Figure 4.16(a) and (b) are SEM micrographs showing the morphology of the fresh and 18-month-old MnBi powder samples. The analysis of particle size was carried out by using the ImageJ software. It was found that the average particle size of the MnBi powder increased from 9.7 μm for the fresh sample to 33.9 μm for the 18-month-old sample, as seen in Figure 4.16(c) and (d). This scenario could be expected by the nature of small and light particles with high magnetic strength. The substantial of large particle size may occur by self-magnetic attraction assisted by environmental humidity and sample storage. There are additional factors playing an important role in the 18-month-old sample. Figure 4.16(a1) and (a2) show the zoom-in SEM image of the individual MnBi particle, respectively. The selected two areas of EDS square scan were presented in Figure 4.16(e). The quantities results of EDS square analysis for the fresh sample and 18-month-old are composed of Mn, Bi, and O elements. The atomic percentage of O increased from 12.73% for the fresh sample to 35.30% for the 18-month-old sample. The atomic percentage trend of O increases while Mn decreases, and Bi remains almost unchanged. The Mn fluctuates with O more than Bi, indicating that Mn is highly sensitive to oxygen.

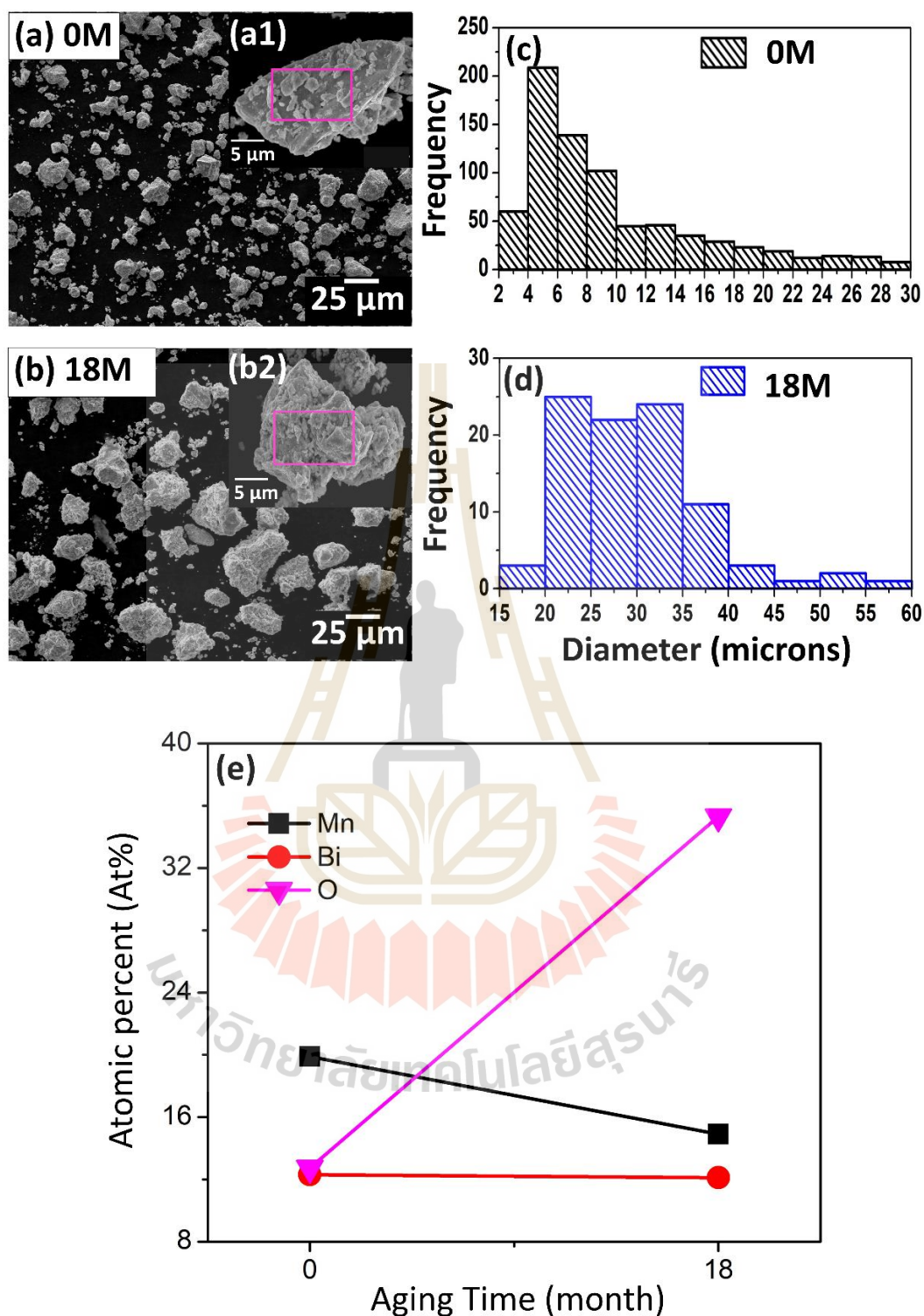


Figure 4.16 SEM images of (a) fresh and (b) 18-month-old MnBi powders. The particle size distribution of MnBi powders shown in (c) and (d). The red squares in (a) and (b) are the areas for EDS measurements to determine the elemental composition, as shown in (e).

4.3.3 Phase identification

XRD measurements and analysis were performed to identify not only the phase structure but also the degree of randomly phase distribution. As seen in Figure 4.17(a), the wide scan XRD patterns of all samples present the dominant peaks of MnBi phase (card No. 96-900-8900) and Bi phase (card No. 96-231-0890) as well as tiny peaks of Mn phase (card No. 96-901-1109) and MnO phase (card No. 96-101-0394). The crystallite size (D) can be calculated by full width with half maximum (FWHM; B) with formula is ($D = \frac{K\lambda}{B \cos\theta}$), where is $K = 0.9$ is shape factor constant. The crystallite size and FWHM are 51.75 nm, 35.53 nm, and 0.17 deg., 0.26 deg. for the fresh and old samples, respectively. The old sample had a smaller crystallite size than the fresh sample. The percentage of crystallinity of two samples are 93.64% and 85.86%, respectively. They can be estimated by Integral Gaussian fitting of peak (sum area/area all of peak*100). This is a very clear evidence result that sample exposure to air can be found slightly low crystallinity.

After exposing to the air of up to 18 months, the XRD patterns are rather similar to the fresh sample indicating the robustness of our LTP-MnBi prepared by vacuum sintering which is in contrast to other reports (Janotová et al., 2018; M. Y. Sun et al., 2016; Villanueva et al., 2019). It is noticeable that the ratio of the main Bi ($\theta \sim 27^\circ$) and MnBi ($\theta \sim 28^\circ$) peaks of the old sample is distinct from the fresh sample. This result has been described elsewhere by the role of randomly magnetic distribution (RMD) (V. Nguyen et al., 2014).

The degree of RMD can be determined by the relative intensity ratio (γ) between the out-of plane and in-plane XRD peaks commonly be referred to the MnBi (002) and MnBi (101) with angle of 28.2 and 29.2 degrees, respectively. A formula is $\gamma = \left(\frac{I(\text{MnBi}(002))}{I(\text{MnBi}(101))[0.102]} \right)$, where a fully isotopic MnBi powder of theoretical value is 0.102 (Poudyal et al., 2016; Truong and Vuong, 2015).

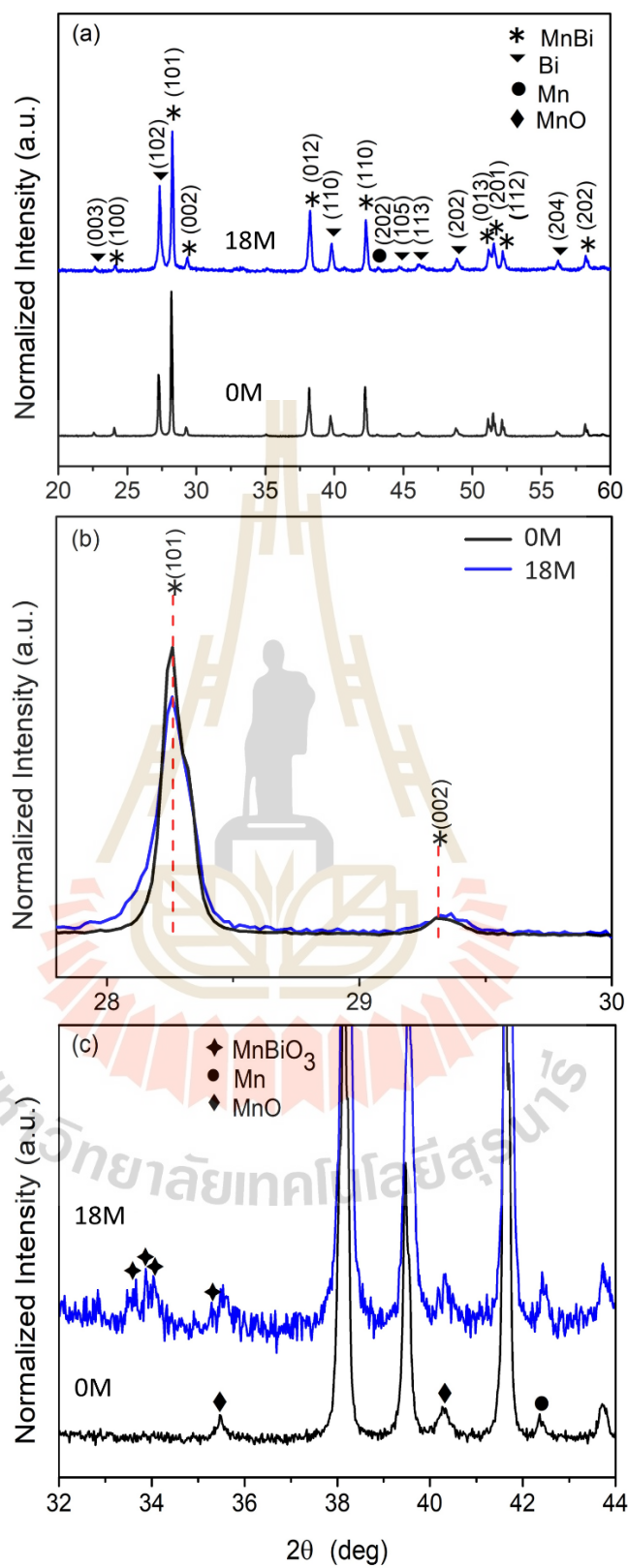


Figure 4.17 XRD patterns of the fresh and 18-month-old LTP-MnBi showing at different 2θ ranges (a) 20 - 60 deg. (b) 27.79 – 30 deg. And (c) 32 – 44 deg.

The zoom-in XRD patterns between $2\theta = 25^\circ$ - 30° are shown in Figure 4.17 (b), where γ can be calculated to be 0.71 and 0.84 for the fresh and 18-month-old samples, respectively. The 18-month-old sample possesses the higher γ indicating better magnetic self-alignment as compared to the fresh sample. This result may be caused by the storage environment of the 18-month-old sample which was squeezed in the limited space and aligned multiple times during VSM measurements. The degree of magnetic self-alignment is strongly related to H_{ci} (Poudyal et al., 2016). In principle, if the sample is better aligned, higher force is required to flip the magnetic domain than the randomly aligned sample resulting in higher H_{ci} (Jain, 2010). This would describe the enlargement of H_{ci} in the 18-month-old sample (Figure 4.15). In view of oxidation, the zoom-in XRD patterns near the baseline are presented in Figure 4.17 (c). Some additional tiny peaks (assigned to MnBiO_3 (card No. 96-434-0613) and MnO phases) were revealed in 18-month-old samples. The low oxides contents could be described by the low free-Mn content on the surfaces which is the advantage of the LTP-MnBi prepared by vacuum sintering. A similar result with Yoshida et al. were observed, they found a low free-Mn content in MnBi ingot at zone-melting, the selecting temperature prepared during phase transformation of HTP to LTP (H. Yoshida, Shima, Takahashi and Fujimori, 1999).

4.3.4 Local structure of Mn atoms

The X-ray absorption (XAS) technique was used to determine the changes of local structure and the oxidation around Mn atoms of the MnBi samples. The experimental and theoretical results of XAS measurement were analyzed by ATHENA software (Ravel and Newville, 2005) and the Feff code version 9 (Rehr, Kas, Vila, Prange and Jorissen, 2010).

Figure 4.18(a) shows the simulated MnO and MnBi XANES spectra. It was found that MnBi possesses broader spectrum with higher positions of the edge-shift and the highest peak energies than MnO. Figure 4.18(b) represents a consistency between our measured Mn K-edge XANES spectrum of the 0M sample and the MnBi:MnO (1:1) linearly combined spectrum. This feature refers to the initial composition of MnO which may cause to the low magnetic performance of our as-prepared sample.

Figure 4.18(c) shows the Mn K-edge spectra of the fresh and 18-month-old samples as well as the standard Mn-foil (Mn^0) and MnO (Mn^{2+}) spectra. It was found that XANES spectra of all samples are similar to the MnO confirming oxides were initially formed on the fresh MnBi samples. The absorption edge of 18-month-old sample seems to be unchanged. The white-line intensity of 18-month-old sample was lower compared to the fresh one indicating more oxidation upon aging.

To better understand such behavior, the Fourier transform magnitude in r-space of experimental and standard samples were computed from EXAFS spectra and represented in Figure 4.18(d). The curves of all samples were closed to the MnO than Mn spectra. We focus on the first Mn-O and Mn-Mn shells which were assigned peak position at $R = 1.6$ and 2.6 \AA , respectively (Nieminen et al., 2019). Interestingly, The Mn-Mn bond of the 18-month-old sample is located at the same position but its Mn-O bond is shifted outward from the reference. This may be implied that the 18-month-old was a small amount of oxidation. We have not an experimental fingerprint of LTP-MnBi to reference the 18-month-old sample. LTP-MnBi is the hexagonal NiAs ($P6_3/mmc$) structure (Bandaru, Sands, Weller and Marinero, 1999). The calculated Mn-Bi bonded lengths are 2.88 \AA (Persson, 2016), which is close to Mn-Mn peak as seen in Figure 4.18(d). Hence, the MnBi powder stored in the 18-month-old sample has virtually no degradation. The oxide layer only occurs on the surface (Mn-O bonding) while the Mn core is unchanged (Mn-Mn bonding) upon aging.

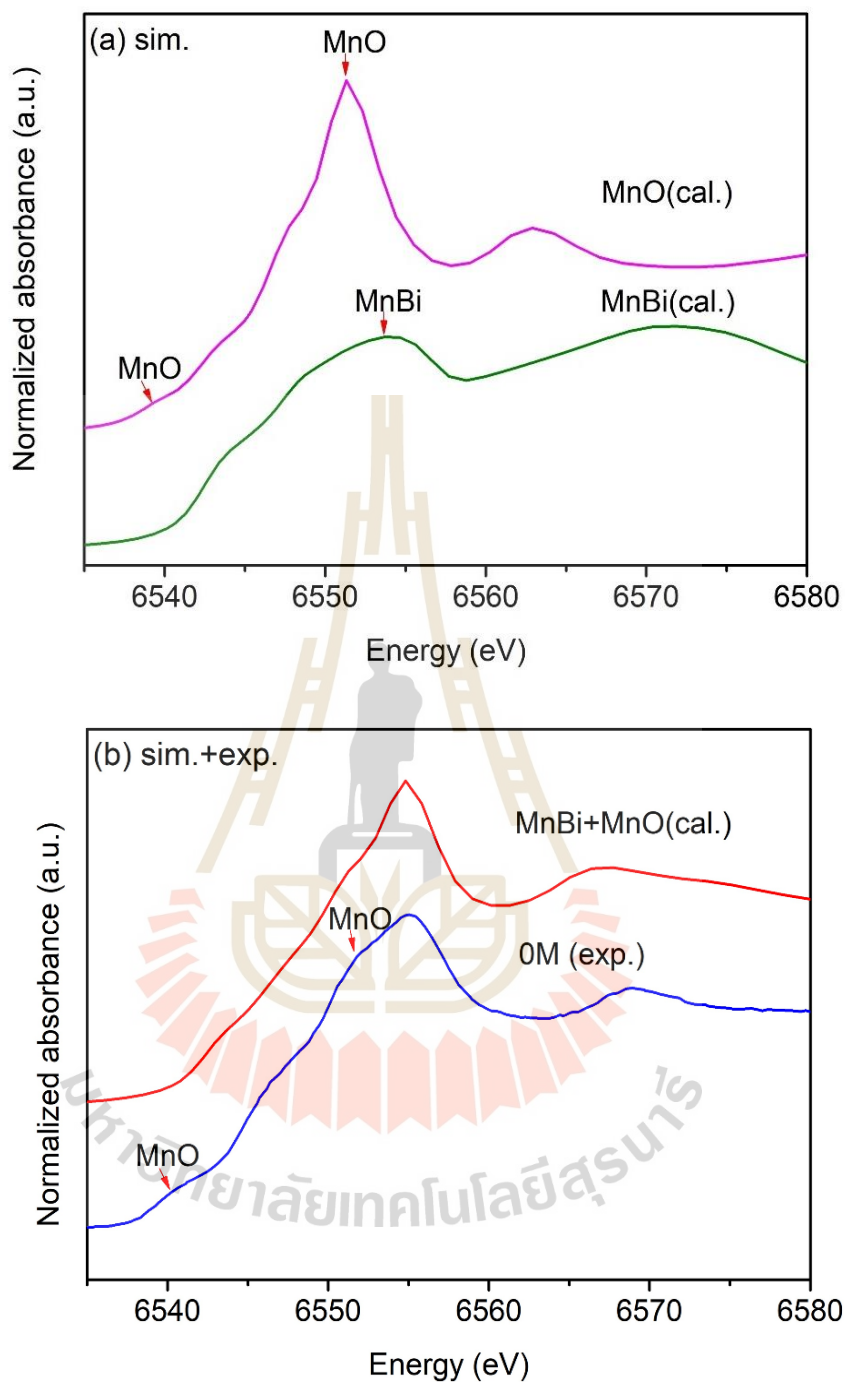


Figure 4.18 (a) Theoretical K-edge XANES spectra of MnO (cal.) and MnBi (cal.), (b) the comparison of theoretical XANES spectrum for MnBi+MnO and experimental XANES spectrum of fresh MnBi, respectively, (c) Mn K-edge XANES spectra of LTP-MnBi and standard samples, (d) Fourier transform of EXAFS spectra of previous samples (fresh MnBi, old MnBi, and standard samples).

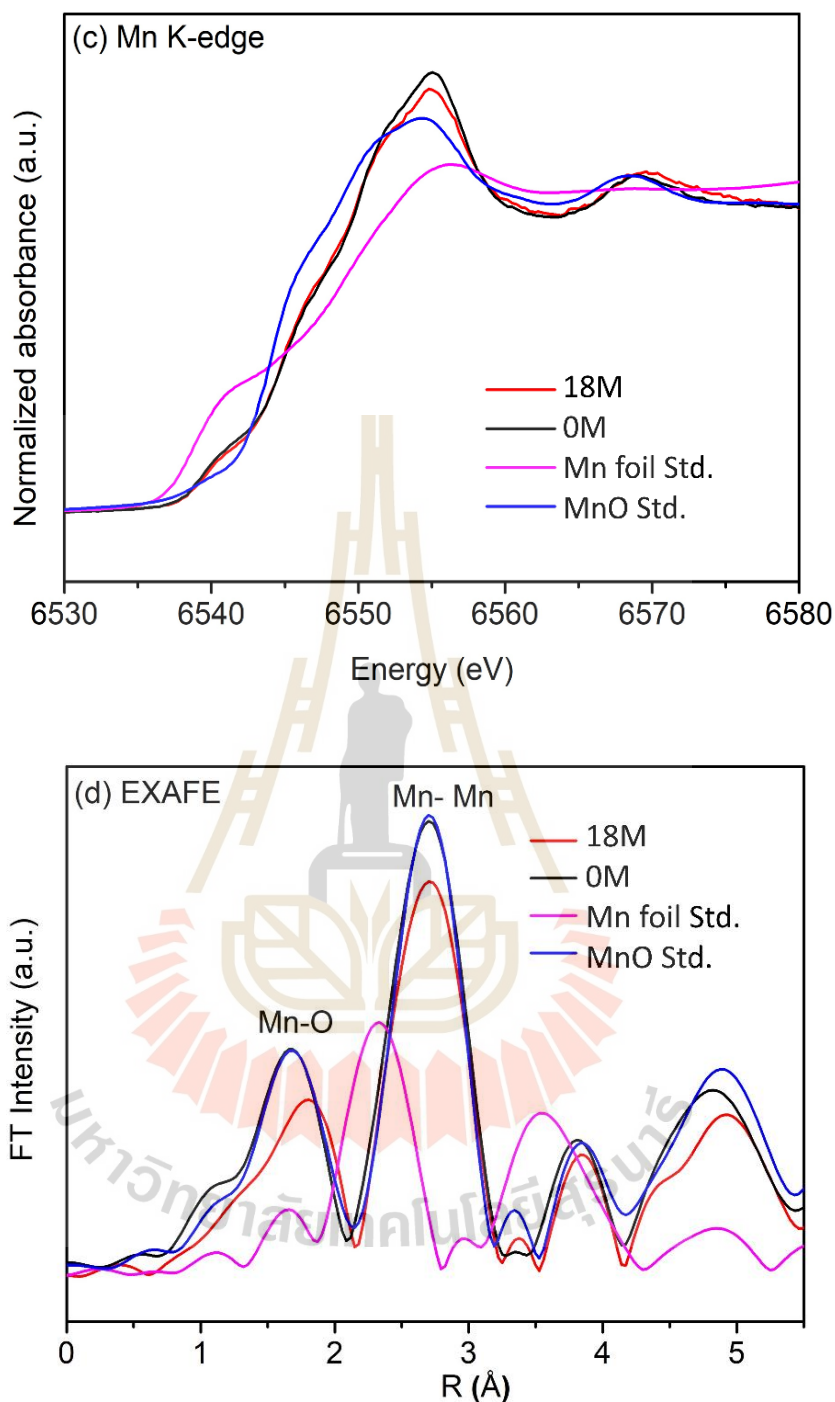


Figure 4.18 (Continue) (a) Theoretical K-edge XANES spectra of MnO (cal.) and MnBi (cal.), (b) the comparison of theoretical XANES spectrum for MnBi+MnO and experimental XANES spectrum of fresh MnBi, respectively, (c) Mn K-edge XANES spectra of LTP-MnBi and standard samples, (d) Fourier transform of EXAFS spectra of previous samples (fresh MnBi, old MnBi, and standard samples).

In this part, the diffusion mechanism is introduced as a key role to explain overall experimental results analytically and logically. Since an increase of $(BH)_{max}$ and the opposite tendency of Fourier transform magnitude in r-space could not be interpreted without adding this term. As mentioned in our previous work (Borsup et al., 2022), the formation of LTP-MnBi during vacuum sintering were described by the diffusion mechanism. The MnBi concentration is directly related to the diffusion length which can be calculated using the diffusion relation $D_c = L^2/t$, where t and L are the diffusion duration and length, respectively (Van Nguyen and Nguyen, 2017). Because the sample reported in this work were sintered at 275 °C for only 3 hr, the $(BH)_{max}$ of 68.50 % compared to our previous work (sintered at 275 °C for 12 hr) is reasonable. Applying the diffusion coefficient of 3.47×10^{-14} cm²/s (at 275 °C), the calculated diffusion length of 204 nm has been obtained for the fresh sample. This is about 53% of the diffusion length reported earlier ($L_{max} = 387$ nm) which is quite consistent with its $(BH)_{max}$.

From the fact that the diffusion process can be continued in much lower rate even at room temperature. By applying Arrhenius plot of activation energy, the diffusion coefficient can be calculated to be $1.45995E-17$ cm²/s at room temperature. An additional diffusion length of 260 nm can then be obtained after storing in the VSM sample container for 18 months. Hence, overall diffusion length could be estimated, by the summation between initial and additional lengths, to be 464 nm. This value is closed to those obtained in previous work with comparable $(BH)_{max}$, as depicted in Figure 4.19. The $(BH)_{max}$ of the 18-month-old sample increases from fresh to 14-month-old samples. The highest $(BH)_{max}$ was observed in the 14-month-old sample whose is then slightly dropped after 18 months. This is due to the large number of magnetic domains in the MnBi layer, as the thickness of MnBi layer increases with increasing aging time, increasing H_{ci} and in part due to the oxide formation affects to the degradation of MnBi magnet exposed to air.

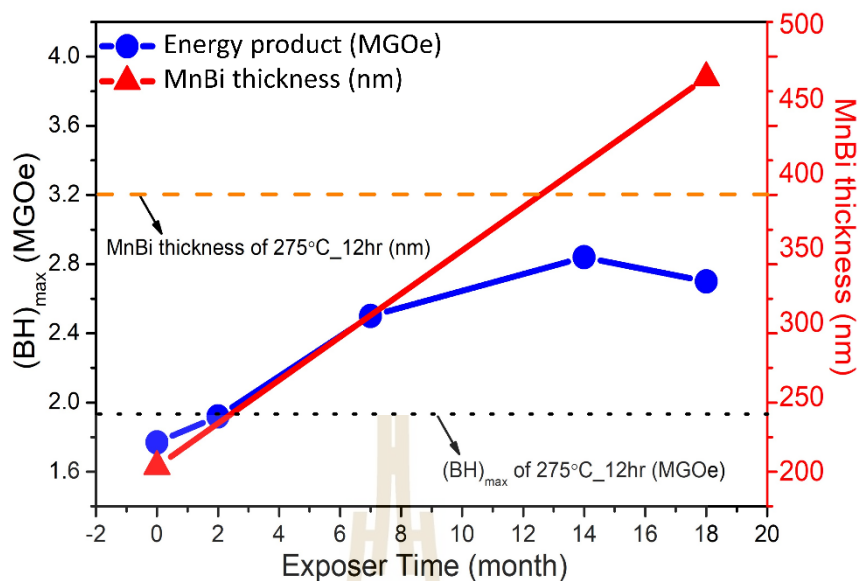


Figure 4.19 Discussion: a relationship of the maximum energy product and diffusion length with a difference period.

4.4 Decomposition of MnBi at 150 °C

This section reports the study of decomposition of LTP-MnBi at elevated temperature. LTP-MnBi powder was prepared at 275 °C for 12hr. After sintering, the samples were heated at 150 °C for different duration in an oven atmosphere (0, 0.5, 3, 6, 12, 24, and 48hr). Annealing time was used as an aging accelerator to monitor the degradation. The ID samples were formatted as MnBi_time. For example, MnBi_48 is the sintered MnBi sample that was heated at 150 °C for 48 hr. Then, the properties of their samples heated at various duration were characterized by several techniques; SEM/EDS, XRD, VSM, and XANES have presented in the details below.

4.4.1 Surface morphology and chemical composition

Figure 4.20 shows the SEM images and their corresponding colors (inset) of the LTP-MnBi powder heated at 150 °C for different periods of time. The surfaces of MnBi_0 was contributed with the white and grey areas, corresponding to the Bi and MnBi phases which are detected by EDS analysis, as seen in Figure 4.20(a). The excess of liquid Bi on the surfaces can be understood as the residue of incomplete diffusion

process during liquid-phase sintering (LPS) (Van Nguyen and Nguyen, 2017). The average particle size of the sintered sample is 20 μm which is approximately three times larger than the milled-Mn particles ($\sim 9 \mu\text{m}$) resulting from the Mn-Bi densification during LPS. It is seen that the proportion of Bi phase decreases as a function of heating time (reduction of white area ratio) where most of the Bi areas are obviously appeared as white circular particles labelled by green narrow. As a function of heating time, the oxygen content increases as seen in points A and D of Figure 4.20(h). In addition, point C has more Mn than point B, resulting in a higher oxygen content. This could be described by the reactive nature of Mn which is oxidized much easier than Bi.

By considering the colors at each condition, the MnBi_0 possesses the light brown color which is rather similar to the starting Bi powder. This is possibly related to the numerous coverages of Bi on the surfaces as seen in the SEM image (Figure 1(a)). Its color turns to darker brown and then navy blue after 0.5 and 3 hr heating time, respectively. The color slightly changes to dark green afterwards, however, not obvious. The changes in sample's color might be described by the formation of manganese oxide in different oxidation states. For example, the Mn^{2+} is pale pink, Mn^{4+} is brown/black and Mn^{6+} is green. 3+, or any incorrect color. (Received from <https://www.chemicool.com/elements/manganese.html>). The striking color changes are consistent with the domination of oxide areas as seen in the SEM image.

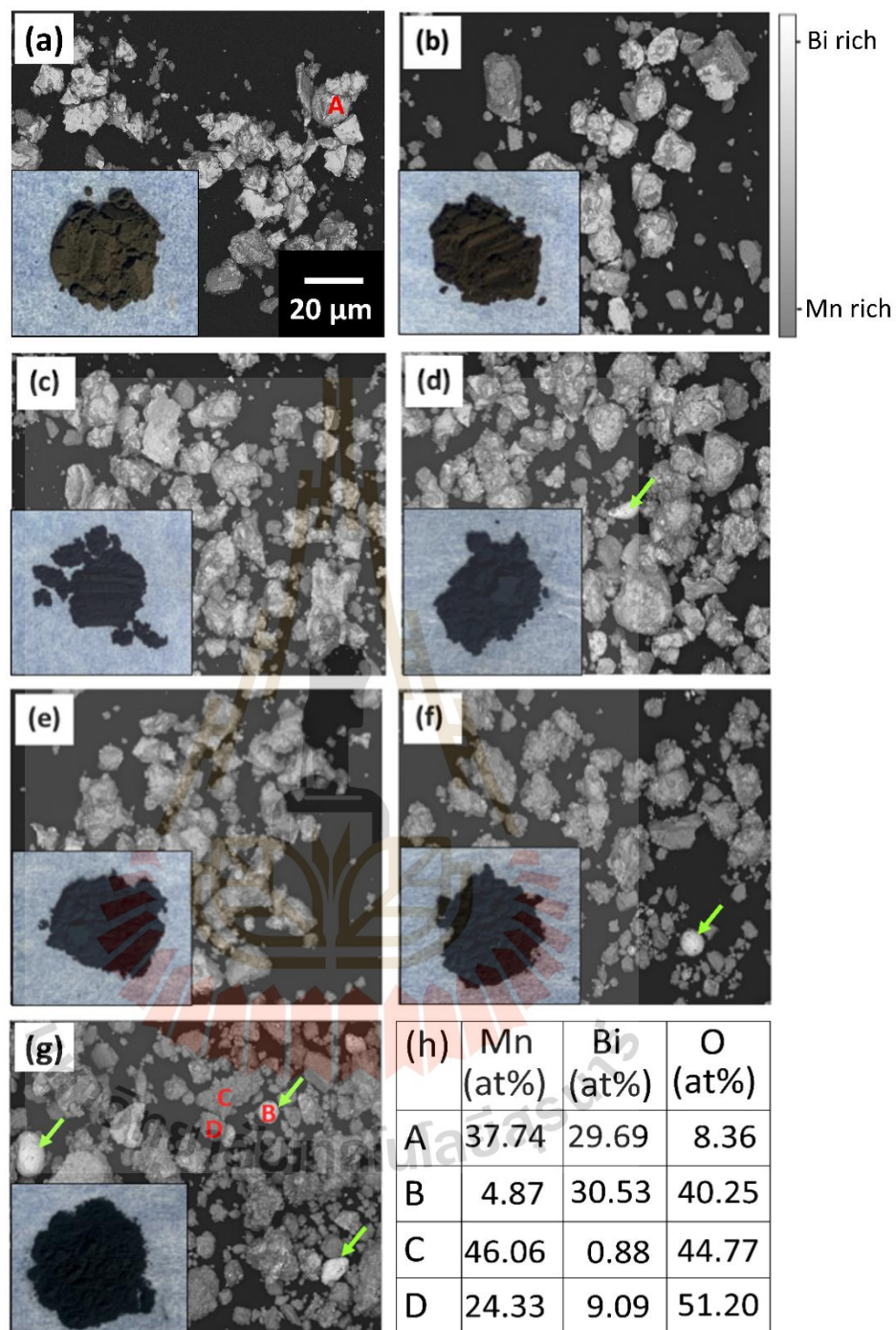


Figure 4.20 SEM images of LTP-MnBi powder heated at 150 °C at different duration; (a) 0, (b) 0.5, (c) 3, (d) 6, (e) 12, (f) 24, and (g) 48hr. Inset shows their corresponding colors of all samples, and the specific points of EDS analysis (A, B, C, and D) in (h).

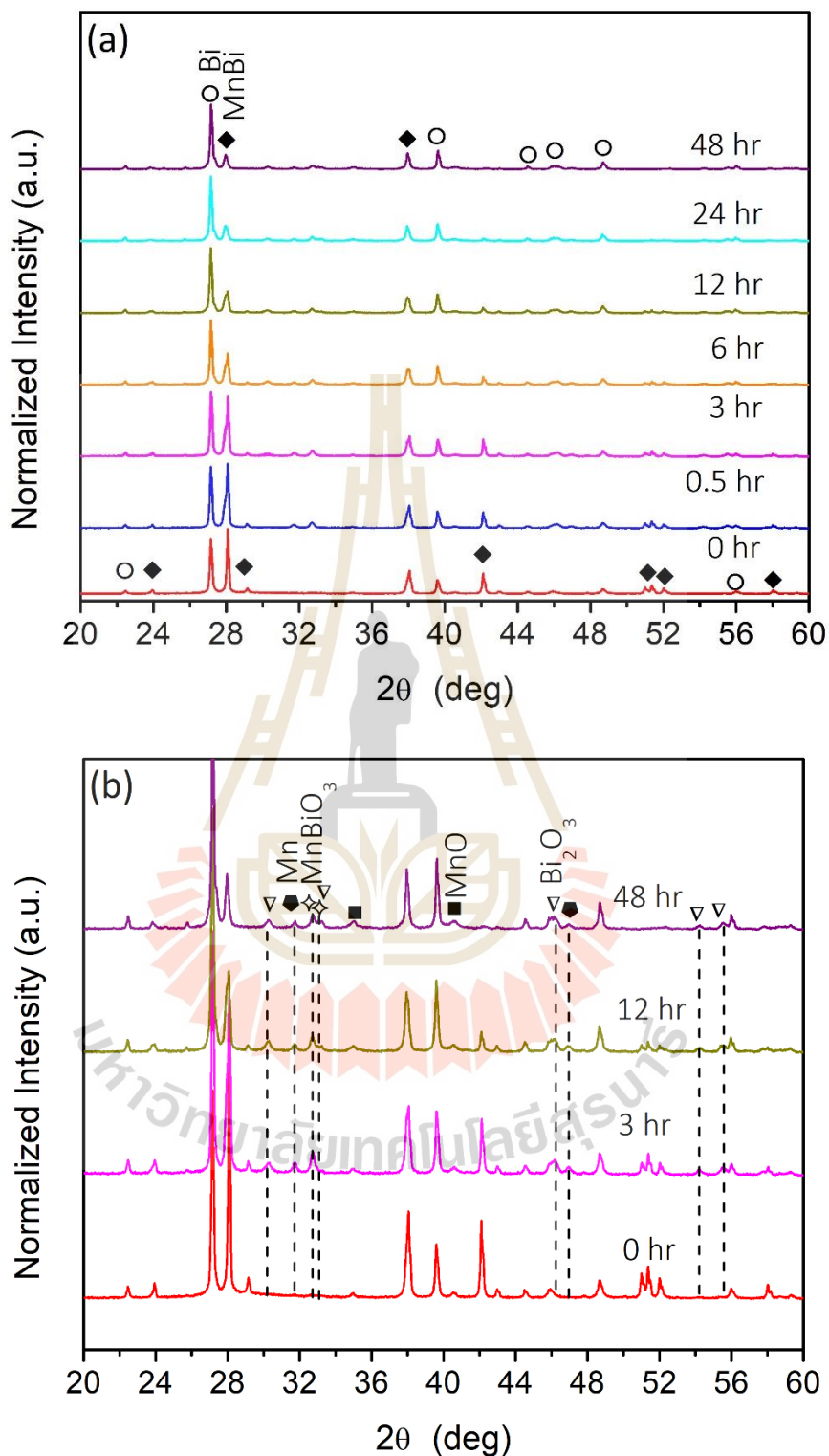


Figure 4.21 (a) X-ray diffraction patterns of LTP-MnBi powder heated at 150 °C for different duration. (b) The zoom-in patterns of selected conditions revealing several forms of impurities.

4.4.2 Phase identification

The XRD patterns of MnBi samples after thermal annealing as a function of heating duration and the zoom-in XRD patterns of selected conditions revealing several forms of impurities are shown in Figure 4.21(a) and Figure 4.21(b), respectively. The as-sintered sample (red spectrum) has mainly contained MnBi (card No. 96-900-8900) and Bi phases (card No. 96-231-0890), also including to the tiny peaks of MnO phase (card No. 96-101-0394). After heating duration, the intensity of MnBi main peaks decreased whereas the Bi and Mn peaks experienced an increase as a function of heating time. The oxide peaks were $2\theta = 30.27, 31.75, 32.76, 33.18, 46.17, 46.96, 54.23$ and 55.5 deg, which indicated by the vertical black dot. The tendency of those peaks increased with increasing heating time. Those peaks corresponded to MnO (card No. 96-101-0394), MnBiO_3 (card No. 96-434-0613) and Bi_2O_3 (card No. 01-074-1375) phases, respectively. The percentage of MnBi concentration were calculated approximately using the relative area ratio between the intensity of main MnBi and Bi peaks ($2\theta = 27.27$ and 28.07 deg, respectively) to be 51.9, 48.8, 40.8, 31.7, 23.6, 15.8 and 12.4 wt% for MnBi_0, MnBi_0.5, MnBi_3, MnBi_6, MnBi_12, MnBi_24 and MnBi_48, respectively. However, the oxide content is relatively low, not more than 5% of MnBi_48. The oxide formation was likely formed at the surface. The high residual Bi content is due to the fact that Bi is more difficult to oxidized than Mn (Villanueva et al., 2019). The XRD results support the MnBi decomposition, Mn and Bi segregated from MnBi during heating, leading to MnBi phases decreased (J. Cui et al., 2014).

4.4.3 Chemical composition

Figure 4.22 shows the Mn-K edge XANES spectra of the selected conditions (MnBi_0, MnBi_12 and MnBi_48), references spectra (MnO and Mn_2O_3), and the old theoretical results of calculated MnBi in Feff code version 9 (Rehr et al., 2010). It can be seen that the edge energy and lineshape of the as-prepared sample is similar to the reference for both MnO and MnBi (cal.), indicating that the MnBi oxidation state is close to Mn^{2+} . The edge energy of all experimental spectra was slightly shifted to Mn_2O_3 reference (Mn^{3+}) and the whiteline increased as elevated heating duration implying an increase of oxides.

The changes in oxidation states of the aged samples were determined by using the linear interpolation between edge energy of MnO (Mn^{2+} , edge energy = 6544 eV) and Mn_2O_3 (Mn^{3+} , edge energy = 6548 eV). The oxidation states were calculated by the form: $x = 3 - z$, where x is oxidation state, and z is a MnO fraction (the 100% of MnO fraction = 1 at edge energy of 6544 eV.) Note that, only the MnO fraction were used as qualitative oxidation state determination and we admitted that other forms of manganese oxides are also expected in the heated sample. The calculated oxidation states are 2, 2.75 and 3 for MnBi_0, MnBi_12 and MnBi_48, respectively.

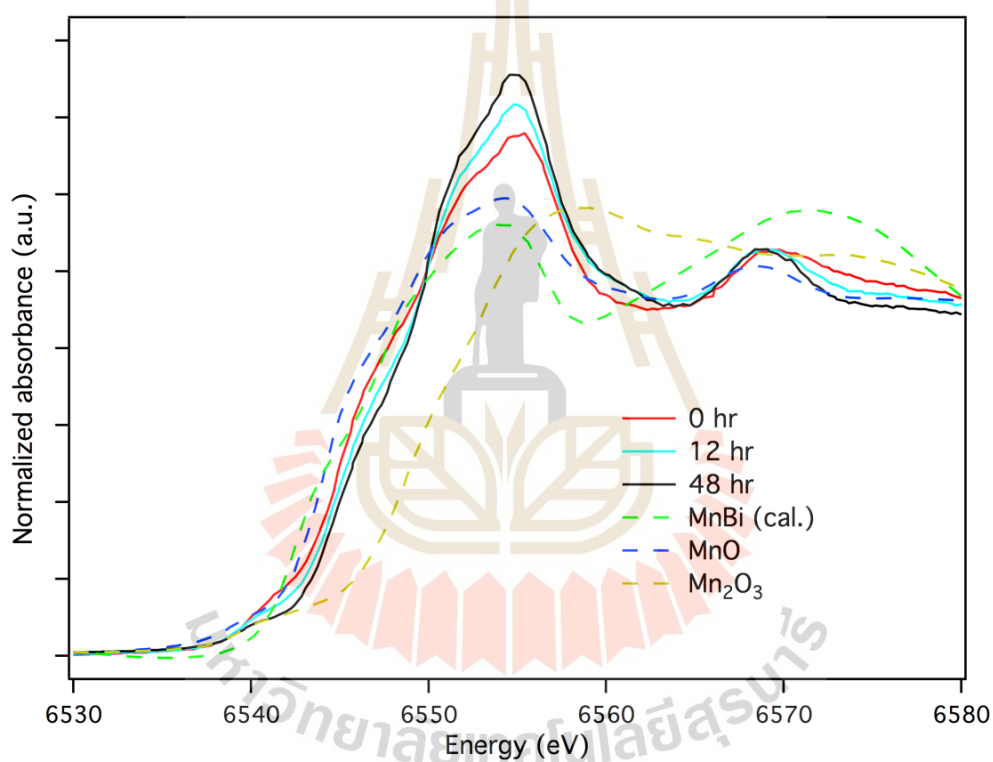


Figure 4.22 The Mn K-edge XANES spectra of MnBi powder heated at 150 °C for different duration. Dashed lines represent MnO, Mn_2O_3 and calculated MnBi spectra.

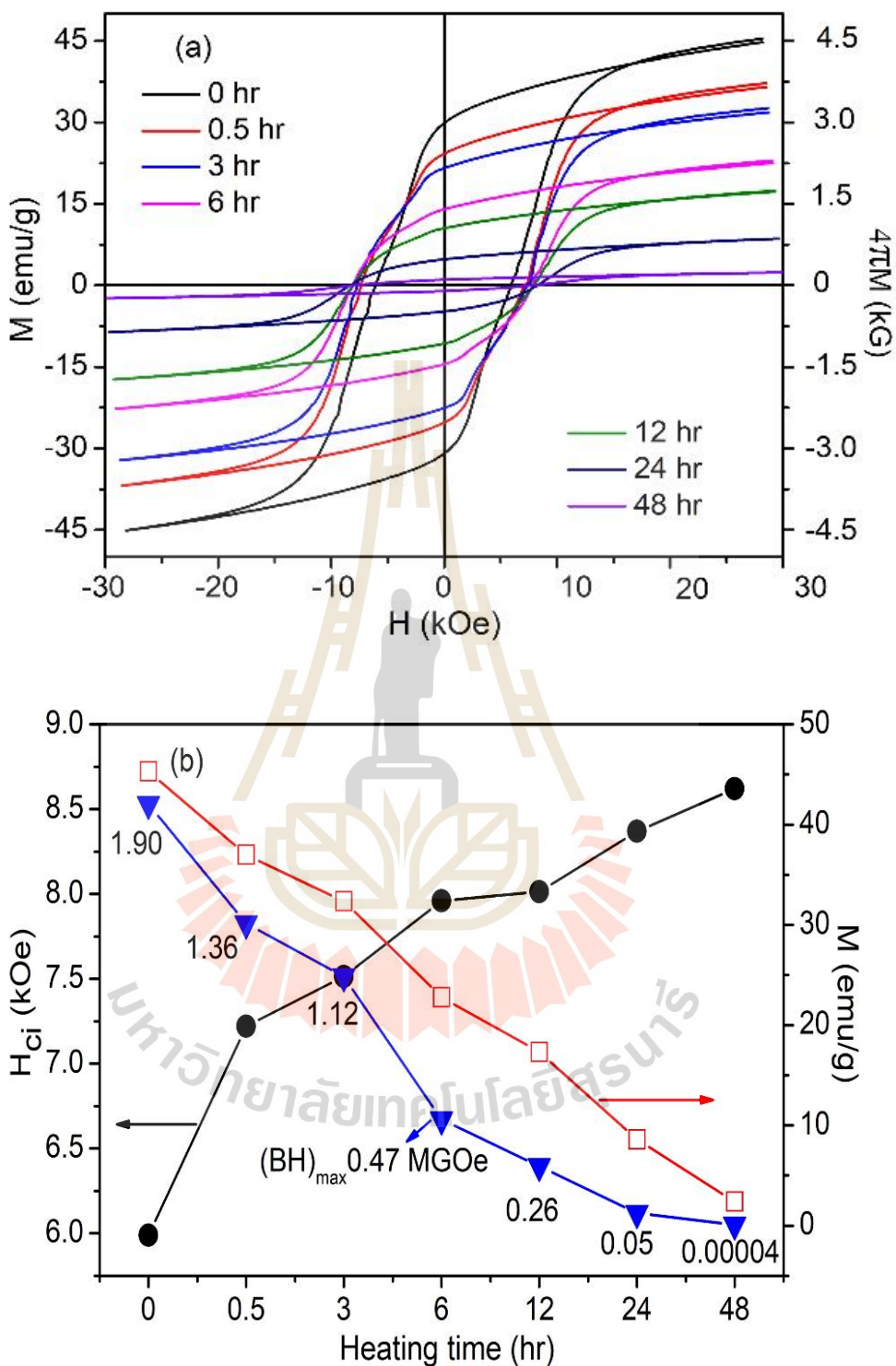


Figure 4.23 (a) Room temperature M-H curves with demagnetization field corrector of MnBi powder heated at 150 °C for different duration. (b) Extracted saturation magnetization (M_s), coercivity (H_{ci}) and the calculated energy products ($(BH)_{max}$).

4.4.3 Magnetic properties

The magnetic properties of MnBi powder heated at different duration were studied by VSM. The room temperature M-H curves with demagnetization field of MnBi powder at different conditions were plotted in Figure 4.23(a).

Their corresponding magnetic values including saturation magnetization (M_s), coercivity (H_{ci}) and energy products ($(BH)_{max}$) were presented in Figure 4.23(b). The magnetic properties of the as-fabricated sample are $M_s = 45.31$ emu/g, $H_{ci} = 5.98$ kOe and $(BH)_{max} = 1.90$ MGOe. A comparison of $(BH)_{max}$ between MnBi_0 and the small MnBi-275 °C for 12 hr (Table 4.1) is 12.84%, which is possibly due to relatively low MnBi content in these sample batches. This circumstance can be expected from the inhomogeneous MnBi formation which is varied by gravitational effect, initial mass, and other uncertain factors during LPS.

As seen in Figure 4.23(b), the value of M_s decreases noticeably from 45.31 to 2.38 emu/g or by 90.01% in the last condition. The H_{ci} rose from 5.98 kOe and saturated at the value of about 8.62 kOe after 48 hr heating time due to oxidation (M. Y. Sun et al., 2016). With a dramatic decrease of M_s , the $(BH)_{max}$ dropped sharply after heating where only $(BH)_{max} = 0.00004$ MGOe were observed in the sample heated at 150 °C for 48 hr. The greatly reduction of ferromagnetic response in the heated sample is agreeable with a reduction of LTP-MnBi content shown in the XRD patterns of Figure 4.21(b). The reduction of MnBi content is considering much faster than by natural aging. It was reported that 54% drop of M_s for MnBi thin film with 10 nm Ta capping after 6 days of exposure time which was completely disappeared after 4 months (Villanueva et al., 2019). Another reports no significant change for MnBi thin film protected with a Ta capping layer while the sample without capping layer experiences a 35% drop after 14 days' exposure to air (J. Sun et al., 2016). In addition, it is reported that the magnetic properties of the MnBi powder which was sealed in epoxy resin and kept under Ar atmosphere showed no considerable change up to 80 days while the one kept under ambient atmosphere attributed to a dramatic decrease after exposing longer than 7 days (Ly et al., 2014). From above characterizations, it was found that thermal strongly affects to the magnetic

performance through the reduction of the MnBi content resulted from the segregation and oxide formation. This works pointed out that thermal is one of the crucial parameters for degradation, in addition to the atmosphere and protection.



CHAPTER V

CONCLUSION AND FUTURE RESEARCH

5.1 Conclusions

This thesis work showed that low-temperature liquid phase sintering (LPS) in vacuum requires no extensive post-sintering processing, and thus is a facile technique for mass production of LTP-MnBi with good magnetic properties. Powder of LTP-MnBi with coercivity of about 5 kOe at room temperature has been achieved by a single-step low-temperature LPS. The highest $(BH)_{max}$ of 5.5 MGOe was obtained for the MnBi powder sintered at 325 °C.

The complex nature of the liquid phase sintering processes for synthesizing LTP-MnBi was explained. The diffusion mechanism plays an important role in the formation of LTP-MnBi during low-temperature LPS in vacuum. At sintering temperatures higher than the melting point, Bi powder was melted into liquid before migrating over the surface of the Mn particles, and along the cracks within the Mn particles. LTP-MnBi layers were formed when Bi diffuses into the bulk Mn particles from their exterior surfaces and from interior surfaces of cracks within the particles.

The diffusion coefficient was deduced from the measured diffusion length obtained by using EDS line scans of the cross-sectional MnBi particles. At temperatures between 275 and 375 °C, the diffusion coefficient was found to follow the Arrhenius equation with the pre-exponential factor of 5.33×10^{-10} cm²/s and activation energy of 0.45 eV. This equation provides the information to estimate the thickness of LTP-MnBi layers sintered at any temperature between 275 and 375 °C for a given sintering duration. Therefore, proper parameters of the starting materials and optimum conditions for the sintering process could be chosen to achieve the best performance sintered LTP-MnBi. The optimum sintering temperature shall not exceed 340 °C to obtain high performance LTP-MnBi with no HTP-MnBi.

At room temperature, sintered LTP-MnBi exhibits interesting changes that the magnetic performance improved with aging. The coercivity and energy product were found to increase with aging (or storing time). At room temperature, LTP-MnBi is rather stable. However, LTP-MnBi is easily decomposed at 150 °C in air atmosphere. The decomposition was caused mainly by oxidation, yielding Mn oxides and Bi. Therefore, the prevention to expose to air must be taken into account seriously to utilize this material at elevated temperatures. Capsulated or thin film coating maybe a solution to this problem.

5.2 Future works

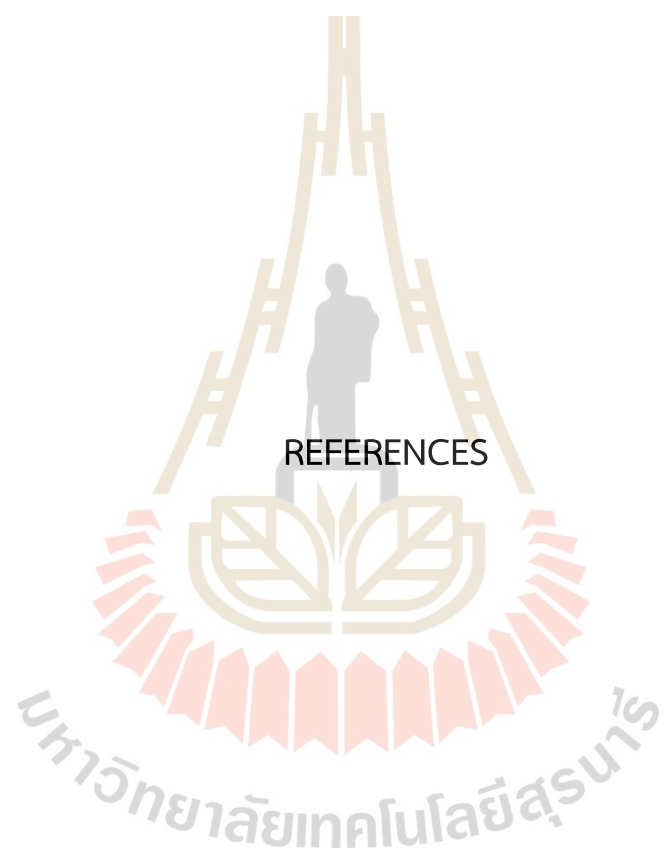
Low-temperature sintering in vacuum is quite a promising method for mass production of LTP-MnBi magnetic materials. However, there is a stringent condition that high content LTP-MnBi shall be obtained from the sintered products. Since diffusion is the main process limiting the formation of LTP-MnBi, especially at low temperatures limited by the maximum sintering temperature avoiding the formation of HTP-MnBi. Thus, there are two possible approaches for enhancing the LTP-MnBi content i.e., increasing sintering time and reducing the initial Mn particle size. The former may not be favorable since it is both time and energy consuming. The latter is very attractive to explore. Reducing the starting Mn powder particles to be about or less than 1 μm will greatly decrease require sintering time to transform a whole Mn particle to be LTP-MnBi. Ball-milling may not be applicable for reducing the Mn particle prior to sintering. Atomizing technique might be the technique for mass production of Mn powder with particle size of about or less than 1 μm . Not only the increase in LTP-MnBi content, but also the increase in the value of coercivity will benefit from the small particle size.

The formation of LTP-MnBi layers on exterior surface of the Mn particles and on the interior surfaces on the cracks inside the Mn particle resulting complex LTP-MnBi materials. It is interesting to investigate the magnetic domains in this material system. The LTP-MnBi layers are in fact the MnBi sheets with irregular feature due to the complex nature of the cracks. Magnetic force microscope (MFM) shall be employed for this kind of investigation.

Thermal stability and decomposition of LTP-MnBi shall be explored more in-depth. Study of thermal stability of the LTP-MnBi at different elevated temperatures shall be carried to identify the maximum working temperature. Capsulating and thin film coating shall also be investigated to seek for solutions for protecting the LTP-MnBi in hazardous ambient.

Last but not least, development of permanent magnets using shall also be investigated. This might also include the utilization of LTP-MnBi as a hard phase magnetic materials for composited permanent magnets.





REFERENCES

REFERENCES

- Adams, E., Hubbard, W. M., and Syeles, A. M. (1952). A New Permanent Magnet from Powdered Manganese Bismuthide. *Journal of Applied Physics*. 23(11), 1207-1211.
- Akagi, F. (2019). Magnetic Domain Structures and Techniques in Micromagnetics Simulation. In K. Fujisaki (Ed.), *Magnetic Material for Motor Drive Systems: Fusion Technology of Electromagnetic Fields* (pp. 165-179). Singapore: Springer Singapore.
- Antonov, V. N., and Antropov, V. P. (2020). Low-temperature MnBi alloys: Electronic and magnetic properties, constitution, morphology and fabrication (Review article). *Low Temperature Physics*. 46(1), 1-27.
- Bandaru, R., Sands, T., Weller, D., and Marinero, E. (1999). Magneto-optical properties of chromium-alloyed manganese bismuth thin films. *Journal of Applied Physics*. 86.
- Borsup, J., Eknapakul, T., Thazin Myint, H., Smith, M. F., Yordsri, V., Pinitsoontorn, S., Thanachayanont, C., Zaw Oo, T., and Songsiriritthigul, P. (2022). Formation and magnetic properties of low-temperature phase manganese bismuth prepared by low-temperature liquid phase sintering in vacuum. *Journal of Magnetism and Magnetic Materials*. 544, 168661.
- Cao, J., Huang, Y., Hou, Y. H., Shi, Z. Q., Yan, X. T., Zhong, Z., and Wang, G. P. (2018). Microstructure and magnetic properties of MnBi alloys with high coercivity and significant anisotropy prepared by surfactant assisted ball milling. *Journal of Magnetism and Magnetic Materials*. 473.
- Cao, J., Huang, Y. L., Hou, Y. H., Shi, Z. Q., Yan, X. T., Zhong, Z. C., and Wang, G. P. (2019). Microstructure and magnetic properties of MnBi alloys with high coercivity and significant anisotropy prepared by surfactant assisted ball milling. *Journal of Magnetism and Magnetic Materials*. 473, 505-51

- Cao, J., Huang, Y. L., Hou, Y. H., Zhang, G. Q., Shi, Z. Q., Zhong, Z. C., and Liu, Z. W. (2018). Effects of intergranular phase on the coercivity for MnBi magnets prepared by spark plasma sintering. *AIP Advances*. 8(5), 055132.
- Cao, S., Yue, M., Yang, Y. X., Zhang, D. T., Liu, W. Q., Zhang, J. X., Guo, Z. H., and Li, W. (2011). Magnetic properties and thermal stability of MnBi/NdFeB hybrid bonded magnets. *Journal of Applied Physics*. 109(7), 07A740.
- Chen, T. (1974). Contribution to the equilibrium phase diagram of the Mn–Bi system near MnBi. *Journal of Applied Physics*. 45(5), 2358-2360.
- Chen, Y.-C., Gregori, G., Leineweber, A., Qu, F., Chen, C.-C., Tietze, T., Kronmüller, H., Schütz, G., and Goering, E. (2015). Unique high-temperature performance of highly condensed MnBi permanent magnets. *Scripta Materialia*. 107, 131-135.
- Chen, Y.-C., Sawatzki, S., Ener, S., Sepehri-Amin, H., Leineweber, A., Gregori, G., Qu, F., Muralidhar, S., Ohkubo, T., Hono, K., Gutfleisch, O., Kronmüller, H., Schütz, G., and Goering, E. (2016). On the synthesis and microstructure analysis of high performance MnBi. *AIP Advances*. 6(12), 125301.
- Corbin, S., and Mclsaac, J. (2003). Differential scanning calorimetry of the stages of transient liquid phase sintering. *Materials Science and Engineering A-structural Materials Properties Microstructure and Processing - MATER SCI ENG A-STRUCT MATER*. 346, 132-140.
- Cui, J., Choi, J. P., Li, G., Polikarpov, E., Darsell, J., Overman, N., Olszta, M., Schreiber, D., Bowden, M., Droubay, T., Kramer, M. J., Zarkevich, N. A., Wang, L. L., Johnson, D. D., Marinescu, M., Takeuchi, I., Huang, Q. Z., Wu, H., Reeve, H., Vuong, N. V., and Liu, J. P. (2014). Thermal stability of MnBi magnetic materials. *Journal of Physics: Condensed Matter*. 26(6), 064212.
- Cui, J., Kramer, M., Zhou, L., Liu, F., Gabay, A., Hadjipanayis, G., Balasubramanian, B., and Sellmyer, D. (2018). Current progress and future challenges in rare-earth-free permanent magnets. *Acta Materialia*. 158, 118-137.
- Energy, U. S. D. o. (2010). *U.S. Department of Energy Critical Materials Strategy*. United States: Department of Energy.

- Gupta, R. K., Anil Kumar, V., and Khanra, G. P. (2018). Reactive and liquid-phase sintering techniques. In R. Mitra (Ed.), *Intermetallic Matrix Composites* (pp. 303-318): Woodhead Publishing.
- Huang, Y. L., Shi, Z. Q., Hou, Y. H., and Cao, J. (2019). Microstructure, improved magnetic properties, and recoil loops characteristics for MnBi alloys. *Journal of Magnetism and Magnetic Materials*. 485, 157-164.
- Jacobson, J., and Kim, A. (1987). Oxidation behavior of Nd-Fe-B magnets. *Journal of Applied Physics*. 61(8), 3763-3765.
- Jain, S. D. (2010). *Engineering Physics: Universities Press*.
- Janotová, I., Švec, P., Matko, I., Janičkovič, D., and Sr., P. Š. (2018). Evolution and degradation of magnetic MnBi phase. *AIP Conference Proceedings*. 1996(1), 020021.
- Jensen, B. A., Tang, W., Liu, X., Nolte, A. I., Ouyang, G., Dennis, K. W., and Cui, J. (2019). Optimizing composition in MnBi permanent magnet alloys. *Acta Materialia*. 181, 595-602.
- Kang, S.-J. (2005). *Sintering, Densification, Grain Growth and Microstructure*. USA: Elsevier Butterworth-Heinemann.
- Kharel, P., Shah, V. R., Li, X. Z., Zhang, W. Y., Skomski, R., Shield, J. E., and Sellmyer, D. J. (2013). Structural and magnetic properties of Pr-alloyed MnBi nanostructures. *Journal of Physics D: Applied Physics*. 46(9), 095003.
- Kim, S., Moon, H., Jung, H., Kim, S.-M., Lee, H.-S., Choi-Yim, H., and Lee, W. (2017). Magnetic properties of large-scaled MnBi bulk magnets. *Journal of Alloys and Compounds*. 708, 1245-1249.
- Kirkemide, A., Shen, J., Gong, M., Cui, J., and Ren, S. (2015). Metal-Redox Synthesis of MnBi Hard Magnetic Nanoparticles. *Chemistry of Materials*. 27(13), 4677-4681.
- Kishimoto, M., and Wakai, K. (1977). Effect of Grinding on the Coercivity of MnBi Particles. *Japanese Journal of Applied Physics*. 16(3), 459-463.
- Klysubun, W. (2006). *X-ray absorption spectroscopy at Siam Photon Laboratory*. Nakhon Ratchasima: Synchrotron Light Research Institute.

- Ko, K. Y., Choi, S. J., Yoon, S. K., and Kwon, Y. S. (2007). MnBi magnets fabricated through spark plasma-sintering process. *Journal of Magnetism and Magnetic Materials*. 310(2, Part 3), e887-e889.
- Kramer, M. J., McCallum, R. W., Anderson, I. A., and Constantinides, S. (2012). Prospects for Non-Rare Earth Permanent Magnets for Traction Motors and Generators. *JOM Journal of the Minerals Metals and Materials Society*. 64(7), 752-763.
- Li, B., Ma, Y., Shao, B., Li, C., Chen, D., Sun, J., Zheng, Q., and Yin, X. (2018). Preparation and magnetic properties of anisotropic MnBi powders. *Physica B: Condensed Matter*. 530, 322-326.
- Li, X., Pan, D., Zhen, X., Lu, W., and Batalu, D. (2019). Microstructure and Magnetic Properties of Mn₅₅Bi₄₅ Powders Obtained by Different Ball Milling Processes. *Metals*. 9, 441.
- Liu, S., Wang, J., and Dong, F. (2018). A new bottom-up synthesis of MnBi particles with high magnetic performance. *Chemical Physics Letters*. 691, 325-329.
- Ly, V., Wu, X., Smillie, L., Shoji, T., Kato, A., Manabe, A., and Suzuki, K. (2014). Low-temperature phase MnBi compound: A potential candidate for rare-earth free permanent magnets. *Journal of Alloys and Compounds*. 615, S285-S290.
- Mehrer, H. (2007.). *Diffusion in solids : fundamentals, methods, materials, diffusion-controlled processes*. Berlin, New York : Springer.
- Mican, S., Hirian, R., Isnard, O., Chicinaş, I., and Pop, V. (2015). Effect of Milling Conditions on the Microstructure and Interphase Exchange Coupling of Nd₂Fe₁₄B/ α -Fe Nanocomposites. *Physics Procedia*. 75, 1314-1323.
- Mohapatra, J., and Liu, J. P. (2018). *Handbook of Rare-Earth-Free Permanent Magnets: The Past and Future* (Vol. 27). Brück.: Elsevier.
- Nguyen, P.-K., Jin, S., and Berkowitz, A. E. (2013). Unexpected Magnetic Domain Behavior in LTP-MnBi. *IEEE Transactions on Magnetism*. 49(7), 3387-3390.
- Nguyen, V., Poudyal, N., Liu, X., Liu, J., Kramer, M., and Cui, J. (2014). High-Performance MnBi Alloy Prepared Using Profiled Heat Treatment. *Magnetics, IEEE Transactions on*. 50, 1-6.

- Nguyen, V. V., Poudyal, N., Liu, X. B., Liu, J. P., Sun, K., Kramer, M. J., and Cui, J. (2014). Novel processing of high-performance MnBi magnets. *Materials Research Express*. 1(3), 036108.
- Nieminen, H.-E., Miikkulainen, V., Settapani, D., Simonelli, L., Hönicke, P., Zech, C., Kayser, Y., Beckhoff, B., Honkanen, A.-P., Heikkilä, M. J., Mizohata, K., Meinander, K., Ylivaara, O. M. E., Huotari, S., and Ritala, M. (2019). Intercalation of Lithium Ions from Gaseous Precursors into β -MnO₂ Thin Films Deposited by Atomic Layer Deposition. *The Journal of Physical Chemistry C*. 123(25), 15802-15814.
- Park, J., Hong, Y.-K., Lee, J., Lee, W., Kim, S.-G., and Choi, C.-J. (2014). Electronic Structure and Maximum Energy Product of MnBi. *Metals*. 4(3), 455-464.
- Patel, K., Zhang, J., and Ren, S. (2018). Rare-earth-free high energy product manganese-based magnetic materials. *Nanoscale*. 10(25), 11701-11718.
- Persson, K. (2016). *Materials Data on MnBi (SG:194) by Materials Project*. Retrieved from <https://www.osti.gov/dataexplorer/biblio/dataset/1274398>.
- Poudyal, N., Liu, X., Wang, W., Nguyen, V. V., Ma, Y., Gandha, K., Elkins, K., Liu, J. P., Sun, K., Kramer, M. J., and Cui, J. (2016). Processing of MnBi bulk magnets with enhanced energy product. *AIP Advances*. 6(5), 056004.
- Prozorov, R., and Kogan, V. G. (2018). Effective Demagnetizing Factors of Diamagnetic Samples of Various Shapes. *Physical Review Applied*. 10(1), 014030.
- Rama Rao, N. V., Gabay, A. M., and Hadjipanayis, G. C. (2013). Anisotropic fully dense MnBi permanent magnet with high energy product and high coercivity at elevated temperatures. *Journal of Physics D: Applied Physics*. 46(6), 062001.
- Rama Rao, N. V., Gabay, A. M., Hu, X., and Hadjipanayis, G. C. (2014). Fabrication of anisotropic MnBi nanoparticles by mechanochemical process. *Journal of Alloys and Compounds*. 586, 349-352.
- Ravel, B., and Newville, M. (2005). ATHENA, ARTEMIS, HEPHAESTUS: data analysis for X-ray absorption spectroscopy using IFEFFIT. *Journal of Synchrotron Radiation*. 12(4), 537-541.
- Rehr, J. J., Kas, J. J., Vila, F. D., Prange, M. P., and Jorissen, K. (2010). Parameter-free calculations of X-ray spectra with FEFF9. *Physical Chemistry Chemical Physics*. 12(21), 5503-5513.

- Roberts, B. W. (1956). Neutron Diffraction Study of the Structures and Magnetic Properties of Manganese Bismuthide *Physical Review*. 104(3), 5.
- Sarkar, A., and Basu Mallick, A. (2020). Synthesizing the Hard Magnetic Low-Temperature Phase of MnBi Alloy: Challenges and Prospects. *JOM Journal of the Minerals Metals and Materials Society*. 72(8), 2812-2825.
- Schneider, C. A., Rasband, W. S., and Eliceiri, K. W. (2012). NIH Image to ImageJ: 25 years of image analysis. *Nature methods*. 9(7), 671-675.
- Si, P. Z., Yang, Y., Yao, L. L., Qian, H. D., Ge, H. L., Park, J., Chung, K. C., and Choi, C. J. (2019). Magnetic-field-enhanced reactive synthesis of MnBi from Mn nanoparticles. *Journal of Magnetism and Magnetic Materials*. 476, 243-247.
- Sun, J., Li, C., Huang, Q., Guo-Lei, L., Han, G. B., Yu, S., and Kang, S.-s. (2016). A facile way to synthesize rare-earth-free MnBi magnetic nanoparticles. *RSC Adv*. 6.
- Sun, M. Y., Xu, X. W., Liang, X. A., Sun, X. W., and Zheng, Y. J. (2016). Effect of oxidation on perpendicular magnetic behavior of MnBi thin films. *Journal of Alloys and Compounds*. 672, 59-63.
- Truong, N., and Nguyen, V. (2015). Preparation and Magnetic Properties of MnBi Alloy and its Hybridization with NdFeB. *Journal of Magnetism*. 20, 336-341.
- Truong, N., and Vuong, N. (2015). Preparation and Magnetic Properties of MnBi Alloy and its Hybridization with NdFeB. *Journal of Magnetism*. 20, 336-341.
- Tu, C., and Stutius, W. (1974). The phase transformation and physical properties of the MnBi and Mn_{1.08}Bi compounds. *IEEE Transactions on Magnetism*. 10(3), 581-586.
- Van Nguyen, V., and Nguyen, T. X. (2017). An Approach for Preparing High-Performance MnBi Alloys and Magnets. *Journal of Electronic Materials*. 46(6), 3333-3340.
- Villanueva, M., Navío, C., Céspedes, E., Mompeán, F., García-Hernández, M., Camarero, J., and Bollero, A. (2019). MnBi thin films for high temperature permanent magnet applications. *AIP Advances*. 9(3), 035325.
- Vuong, N. V. (2019). MnBi Magnetic Material: A Critical Review. *Communications in Physics*. 29(4).

- Xie, W., Polikarpov, E., Choi, J.-P., Bowden, M. E., Sun, K., and Cui, J. (2016). Effect of ball milling and heat treatment process on MnBi powders magnetic properties. *Journal of Alloys and Compounds*. 680, 1-5.
- Yang, J. B., Yelon, W. B., James, W. J., Cai, Q., Roy, S., and Ali, N. (2002). Structure and magnetic properties of the MnBi low temperature phase. *Journal of Applied Physics*. 91(10), 7866-7868.
- Yang, Y. B., Chen, X. G., Guo, S., Yan, A. R., Huang, Q. Z., Wu, M. M., Chen, D. F., Yang, Y. C., and Yang, J. B. (2013). Temperature dependences of structure and coercivity for melt-spun MnBi compound. *Journal of Magnetism and Magnetic Materials*. 330, 106-110.
- Yang, Y. B., Chen, X. G., Wu, R., Wei, J. Z., Ma, X. B., Han, J. Z., Du, H. L., Liu, S. Q., Wang, C. S., Yang, Y. C., Zhang, Y., and Yang, J. B. (2012). Preparation and magnetic properties of MnBi. *Journal of Applied Physics*. 111(7), 07E312.
- Yang, Y. B., Wei, J. Z., Peng, X. L., Xia, Y. H., Chen, X. G., Wu, R., Du, H. L., Han, J. Z., Wang, C. S., Yang, Y. C., and Yang, J. B. (2014). Magnetic properties of the anisotropic MnBi/Sm₂Fe₁₇N_x hybrid magnet. *Journal of Applied Physics*. 115(17), 17A721.
- Yoshida, H., Shima, T., Takahashi, T., and Fujimori, H. (1999). Preparation of Highly Pure MnBi Intermetallic Compounds by Arc-Melting. *Materials Transactions, JIM*. 40(5), 455-458.
- Yoshida, S., Okumura, T., Kita, H., Takahashi, J., and Ushioda, K. (2014). High Temperature Tensile Properties and Its Mechanism in Low-Carbon Nb-Bearing Steels. *Materials Transactions*. 55(6), 899-906.
- Zhang, D. T., Cao, S., Yue, M., Liu, W. Q., Zhang, J. X., and Qiang, Y. (2011). Structural and magnetic properties of bulk MnBi permanent magnets. *Journal of Applied Physics*. 109(7), 07A722.
- Zhang, D. T., Geng, W. T., Yue, M., Liu, W. Q., Lu, Q. M., Zhang, J. X., Guo, Z. H., Li, W., Sundararajan, J. A., and Qiang, Y. (2014). Magnetic properties and thermal stability of MnBi/SmFeN hybrid bonded magnets. *Journal of Applied Physics*. 115(17), 17A746.

Zhang, Y., Han, J., Liu, S., Tian, H., Zhao, H., Du, H., Yang, Y., Fang, Y., Li, W., and Yang, J. (2017). Structural modification and ultra-high coercivity of nanostructural anisotropic MnBi/Bi films. *Acta Materialia*. 128.



CURRICULUM VITAE

Name	Miss Jongrak Borsup
Date of birth	February 8, 1993
Place of birth	Bangkok, Thailand
E-mail	jongrak.borsup@gmail.com
Education	
2017-2021	Ph.D. in Physics , Suranaree University of Technology, Nakhon Ratchasima, Thailand
2014-2016	M.Sc. in Physics , Burapha University, Chonburi, Thailand
2011-2014	B.Sc. in Applied-Physics , Burapha University, Chonburi, Thailand
Grants and Fellowships	Science Achievement Scholarship of Thailand (SAST)

List of Research Publications

1. **Borsup, J.**, Eknapakul, T., Thazin Myint, H., Smith, M. F., Yordsri, V., Pinitsoontorn, S., Thanachayanont, C., Zaw Oo, T., and Songsiriritthigul, P. (2022). Formation and magnetic properties of low-temperature phase manganese bismuth prepared by low-temperature liquid phase sintering in vacuum. *Journal of Magnetism and Magnetic Materials*. 544, 168661.
2. Céolin, D., Yuzawa, H., Saisopa, T., Klaiphet, K., **Borsup, J.**, Songsiriritthigul, P., and Kosugi, N. (2021). Substituent effects in aqueous solutions of carboxylate salts studied by x-ray absorption spectroscopy at the oxygen K-edge. *The Journal of Chemical Physics*. 155(1), 014306.